ANALYSIS OF SOLAR TOWER INTEGRATED WITH sCO_2 BRAYTON CYCLE AND MEE-TVC DESALINATION

BY

AMINE ABDULLAH KOUTA

A Thesis Presented to the
DEANSHIP OF GRADUATE STUDIES

KING FAHD UNIVERSITY OF PETROLEUM & MINERALS

DHAHRAN, SAUDI ARABIA

In Partial Fulfillment of the
Requirements for the Degree of

MASTER OF SCIENCE

In

MECHANICAL ENGINEERING

MAY 2015

KING FAHD UNIVERSITY OF PETROLEUM & MINERALS

DHAHRAN- 31261, SAUDI ARABIA

DEANSHIP OF GRADUATE STUDIES

This thesis, written by AMINE ABDULLAH KOUTA under the direction of his thesis advisor and approved by his thesis committee, has been presented and accepted by the Dean of Graduate Studies, in partial fulfillment of the requirements for the degree of **MASTER OF SCIENCE IN MECHANICAL ENGINEERING.**

Dr. Fahad A. Al-Sulaiman
(Advisor)

Dr. Zuhair M. Gasem
Department Chairman

Dr. Yilbas S. Bekir
(Member)

Dr. Salam A. Zummo
Dean of Graduate Studies

Dr. Ahmet Z. Sahin
(Member)

13/10/15
Date

Dedication

To my beloved parents, for their endless love, support, and encouragement

To my older brother Ahmad, for his continuous support and motivation

To my teachers, for their help and guidance

To my friends, for their moral support and advice throughout

ACKNOWLEDGMENTS

All praise and thanks are due to almighty ALLAH, most gracious and most merciful, for his immense beneficence and blessings, without whose help, I would not have been able to make it this far.

I acknowledge, with deep gratitude and appreciation, the inspiration, encouragement, valuable time, and continuous guidance given to me by my thesis advisor, Dr. Fahad Al-Sulaiman. I am also grateful to my committee members, Dr. Yilbas Bekir for his motivation, good will, and for making science look very enjoyable and easy to grasp in earlier coursework, and Dr. Ahmet Sahin for his review and valuable comments on the work conducted.

I would also like to acknowledge the support of King Fahad University of Petroleum & Minerals (KFUPM). Dhahran, Saudi Arabia.

I am also very thankful to my colleague, Mr. Maimoon Atif for his great help throughout the initial stage, and the suggestions and useful discussions throughout.

During my tenure, my mother was an invaluable source of support and motivation. I would also like to express my deep gratitude to my brother Ahmad who supported me in numerous ways throughout.

It is quite impossible to end this section, without giving a great deal of gratitude and appreciation to my dearest colleagues and friends, Fahad Al-Zahrani and Obeidullah Al-Munteshari, for their continuous support, help, and backup throughout my work, and to

my friend Bassam El-Koussa for his moral support and motivation. For them, I owe the lovely memories at KFUPM.

TABLE OF CONTENTS

LIST OF TABLES

LIST OF FIGURES

NOMENCLATURE

A	Radiative area of the central receiver, m^2
A_c	Condenser heat transfer area, m^2
A_{cst}	Heat transfer area of cold storage tank, m^2
A_{ei}	Heat transfer area for i^{th} effect, m^2
A_{fi}	Heat transfer area for the feed preheaters, m^2
A_h	Total area of the heliostats, m^2
A_{hst}	Heat transfer area of hot storage tank, m^2
A_l	Area covered by heliostat, m^2
A_s	Area of Solar Field, m^2
A_{t_s}	Specific heat transfer area, m^2
BPE	Boiling point elevation
ci	Cold fluid in
co	Cold fluid out
C	Specific heat, $kJ/(kgK)$
C_i	Insurance Cost, % of CC_t
C_L	Costs of Logistics and Import, % of CC_t
$C_{storage}$	Storage Costs, \$/kg
CC	Capital Costs, \$/kW, \$/kg, $\$/(m^3/d)$
CC_{cycle}	Capital Cost of Cycle, \$/kW

$CC_{med-tvc}$	MEE-TVC Desalination Capital Cost, $\$/(m^3/d)$
CC_{sf}	Capital Cost of Solar Field, $/m^2
CC_t	Total Capital Cost, $
CF	Capacity Factor, %
CHP	Combined Heat and Power
CR	Compression Ratio
CSP	Concentrated Solar Power
d	Day
$\widehat{d}_n$	Vector normal to heliostat
$\widehat{d}_{rec}$	Vector pointing toward the receiver
$\widehat{d}_{sun}$	Vector pointing toward the sun
$dsep$	Additional security distance between the heliostats, m
DH	Heliostat Diagonal, m
DH_j	Daylight hours for the j^{th} day of the year
DH_k	Daylight hours for the average day of the k^{th} month of the year
DM	Characteristic Diameter, m
DNI	Direct Normal Irradiation, $kW/(m^2/d)$
E_t	Total Lifetime Energy Generation, kWh
EES	Engineering Equation Solver
EIA	U.S. Energy Information Administration
EPA	Environmental Protection Agency
ER	Expansion Ratio

$Ex_{comp,j}$	Exergy destroyed in component j, kWh/d
$Ex_{D,total}$	Total exergy destruction in the whole system, kWh/d
$Ex_{in,j}$	Flow exergy entering the j^{th} component, kWh/d
f	Fraction of heat entering the sCO_2 power cycle
f_{at}	Atmospheric Attenuation Factor
f_{itc}	Intercept factor
f_{sb}	Shadowing and blocking factor
F_{view}	Radiation shape factor
g_b	Specific free Gibbs energy of brine, kJ/kg
g_p	Specific free Gibbs energy of product water, kJ/kg
g_{sw}	Specific free Gibbs energy of incoming seawater, kJ/kg
$GAMS$	Generalized Algebraic Modeling System
GOR	Gain Output Ratio
h_{conv}	Convection heat transfer coefficient, $kW/(m^2K)$
h_d	Enthalpy of discharged steam, kJ/kg
$h_{d_{fn}}$	enthalpy of distillate at thermal equilibrium with the environment, kJ/kg
h_{fd}	Saturated liquid enthalpy of discharged steam after condensation, kJ/kg
h_{fg}	Latent heat of the distillate produced, kJ/kg
h_{g_n}	Saturated vapor enthalpy of the entrained vapor extracted from the last effect, kJ/kg
h_{ts}	Enthalpy state of molten salt storage in the i^{th} state of the thermal storage, $kJ/kg, i=1,4$

h_{isc}	Enthalpy states for the sCO$_2$ power cycle, kJ/kg, $i=1,10$ for recompression, $i=1,6$ for regenerative
h_{2sc_s}	Isentropic enthalpy state at compressor exit, kJ/kg
h_{5st}	Enthalpy state of steam entering the heat exchanger HX-2, $kJ/(kg\cdot K)$
h_{6st}	Enthalpy state of steam leaving the heat exchanger HX-2, $kJ/(kg\cdot K)$
h_s	Enthalpy of motive steam, kJ/kg
h_{sw}	Enthalpy of seawater in the work of separation schematic, kJ/kg
hi	Hot fluid in
H_t	Image dimension tangential plane
I_b	Incident normal radiation, kW/m^2
IEO	International Energy Outlook
$IP_{comp,j}$	Improvement Potential of the j^{th} component, kWh/d
L_i	Latent heat of vaporization, kJ/kg
L_s	Latent heat of motive steam, kJ/kg
$LCOE$	Levelized Cost of Energy, $\$/kWh$
$LCOE_{WS}$	Net Levelized Cost of Energy based on the work of separation, $\$/kWh$
LC_{net}	Net Levelized Cost, $\$/kWh$
$LCOW$	Levelized Cost of Water, $\$/m^3$
LH	Height of the heliostat, m
$(LMTD)_c$	Logarithmic Mean Temperature Difference in the condenser
LR	Receiver size, m
LW	Width of the heliostat, m

$\dot{m}_{bi}$	Brine mass flow rate exiting the i^{th} effect, kg/s, $i = 1, n$
$\dot{m}_{CO_2}$	Mass flow rate of sCO_2, kg/s
$\dot{m}_{d_i}$	Distillate formed in the i^{th} effect, kg/s
$\dot{m}_{d_f}$	Mass flow rate of distillate entering the down condenser, kg/s
$\dot{m}_{d_{tot}}$	Total distillate mass flow rate, kg/s
$\dot{m}_{f_{tot}}$	Total mass flow rate of the seawater, kg/s
$\dot{m}_{fi}$	Mass flow rate of feed entering i^{th} effect, kg/s
$\dot{m}_i$	Mass flow rate in salt storage, kg/s, $i = 1, 4$
$\dot{m}_{is}$	Mass flow rate in the i^{th} state of the thermal storage, kg/s
$\dot{m}_{1st}$	Mass flow rate of steam entering the pump, kg/s
$\dot{m}_{2st}$	Mass flow rate of steam leaving the pump, kg/s
$\dot{m}_{3st}$	Mass flow rate of steam entering the steam jet ejector, kg/s
$\dot{m}_{4st}$	Mass flow rate of saturated liquid leaving the steam splitter, kg/s
$\dot{m}_{5st}$	Mass flow rate of steam entering the heat exchanger HX-2, kg/s
$\dot{m}_{6st}$	Mass flow rate of steam leaving the heat exchanger HX-2, kg/s
$\dot{m}_r$	Vapor entrained from last effect of MEE-TVC, kg/s
$\dot{m}_s$	Motive steam entering the steam jet ejector, kg/s
$\dot{m}_{sw}$	Mass flow rate of the entering seawater, kg/s
M_{cst}	Mass of the storage medium in cold storage tank, kg
M_{hst}	Mass of the storage medium in hot storage tank, kg
$M_{salt,tot}$	Total mass of molten salt, kg

$MEE-TVC$	Multiple-Effect Evaporation with thermal vapor compression
MSF	Multi Stage Flash Desalination
MVC	Mechanical Vapor Compression
n	Number of effects in MEE-TVC
n_d	Day of the year
N	Total Period of Energy Generation, Y
NEA	Non-Equilibrium Allowance
$Nhel$	Number of heliostats
NO_x	Nitrogen Oxide
$OECD$	Organization for Economic Co-operation and Development
OM	Operation and Maintenance Costs, \$/kWh, \$/kg, \$/(m^3/d)
OM_t	Total Operations and Maintenance Costs, \$
$OM_{storage}$	Operation and Maintenance Cost of Storage kg/s
ORC	Organic Rankine Cycle
P_d	Discharged pressure, kPa
P_n	Entrained vapor pressure, kPa
P_s	Motive steam pressure, kPa
PCF	Pressure Correction Factor
PR	Performance Ratio
PWR	Power to Water Ratio, $kW/(m^3/d)$
Q	Thermal load, kW
Q_{1s}	Total energy entering the hot storage tank, kW
Q_{2s}	Total energy leaving the hot storage tank, kW

Q_{3s}	Total energy entering the cold storage tank, kW
Q_{4s}	Total energy leaving the cold storage tank, kW
Q_{conv}	Convection heat loss from the receiver, kW
Q_{cst}	Heat loss rate from the cold storage tank to the ambient, kW
$Q_{cst_{day}}$	Total heat lost from the cold storage tank throughout the day kWh
Q_{d}	Specific heat consumption, kW
Q_{des}	Heat input from thermal storage into MEE-TVC, kW
Q_{des}^{eff}	Effective desalination input heat, kW
Q_{hst}	Heat loss rate from the hot storage tank to the ambient, kW
$Q_{hst_{day}}$	Total heat lost from the hot storage tank throughout the day kWh
Q_{in}	Total energy interception rate by the central receiver, kW
$Q_{in_{CO}}$	Heat added to the supercritical carbon dioxide cycle, kW
$Q_{net,day}$	Average heat per day collected at level of central receiver, kWh
Q_{rad}	Radiation heat losses, kW
$Q_{receiver}$	Net energy gained at the level of the central receiver, kW
$Q_{u}(Q_{net})$	Net useful energy gain rate at the central receiver, kW
Q_{solar}	Incident solar irradiation on the solar field, kW
$Q_{solar_{day}}$	Total incident solar irradiation on the heliostat field for the whole day, kWh
$Q_{solar_{lost_{day}}}$	Total lost energy at the level of the heliostat for the whole day, kWh
R_{i}	Radius of first ring in i^{th} zone of the heliostat, m, $i=1,2,3$

R_{last}	Radius of last row in the heliostat zone, m
RD	Receiver Diameter, m
RDS	Restricted Dead State
s_{bi}	Specific entropy of brine leaving the i^{th} effect, $kJ/(kgK)$, $i=1,n-1$
s_d	Specific entropy of discharged steam, $kJ/(kgK)$
s_{d_f}	Specific entropy of the condensed discharged steam leaving the first effect, $kJ/(kgK)$
$s_{d_{fi}}$	Specific entropy of condensed distillate entering the i^{th} flashbox, $kJ/(kgK)$, $i=2,n$
$s_{d_{gi}}$	Specific entropy of the vapor distillate leaving the i^{th} effect, $kJ/(kgK)$, $i=1,n$
s_{f_i}	Specific entropy of the feed stream entering the i^{th} effect, $kJ/(kgK)$, $i=1,n-1$
s_{is}	Entropy of the i^{th} state of thermal storage, $kJ/(kgK)$, $i=1,4$
s_{isc}	Entropy state of i^{th} sCO_2 cycle, $kJ/(kgK)$, $i=1,10$ for recompression, $i=1,6$ for regenerative
s_{1st}	Entropy state of the steam entering the pump, $kJ/(kg\cdot K)$
s_{2st}	Entropy state of steam leaving the pump, $kJ/(kgK)$
s_{3st}	Entropy state of steam entering the steam jet ejector, $kJ/(kgK)$
s_{4st}	Entropy state of saturated liquid leaving the steam splitter, $kJ/(kgK)$
s_{5st}	Entropy state of steam entering the heat exchanger HX-2, $kJ/(kgK)$
s_{6st}	Entropy state of steam leaving the heat exchanger HX-2, $kJ/(kgK)$
s_s	Specific entropy of motive steam, $kJ/(kgK)$

s_{sw}	Entropy of feed seawater in work of separation derivation, $kJ/(kgK)$
s_{sw_1}	Specific entropy of seawater entering the down condenser, $kJ/(kgK)$
sCO_2	Supercritical Carbon Dioxide
S_{rec}	Slant distance from the heliostat to the receiver, m
$S_{gen_{CST}}$	Total entropy generated for the whole day in the cold storage tank, kWh / K
$S_{gen_{HST}}$	Total entropy generated for the whole day in the hot storage tank, kWh / K
$S_{gen}^{MEE-TVC}$	Entropy generation in MEE-TVC, $kWh/(K\cdot d)$
S_{gen}^{ST}	Total entropy generation in the solar tower for the whole day, kWh / K
SO_2	Sulfur Dioxide
SS_m	Storage of Molten Salts, tons
ST	Solar Tower
$\dot{S}_{gen_{comp}}$	Entropy generated in compressor of regeneration cycle, kW/K
$\dot{S}_{gen_{comp1}}$	Entropy generated in 1st compressor of recompression cycle, kW/K
$\dot{S}_{gen_{comp2}}$	Entropy generated in 2nd compressor of recompression cycle, kW/K
$\dot{S}_{gen_{dc}}$	Entropy generation in the down condenser, kW/K
$\dot{S}_{gen_{effi}}$	Entropy generated in the i^{th} effect, kW/K, $i=1,n-1$
$\dot{S}_{gen_{fb_i}}$	Entropy generated in i^{th} flashbox, kW/K, $i=1,n-1$
$\dot{S}_{gen_{HTR}}$	Entropy generated in high temperature recuperator, kW/K
$\dot{S}_{gen_{HX-i}}$	Entropy generation rate in the i^{th} heat exchanger, kW/K, $i=1,2$
$\dot{S}_{gen_{LTR}}$	Entropy generated in low temperature recuperator, kW/K

$\dot{S}_{gen_{LTR}}$	Entropy generated in low temperature recuperator, kW/K
$\dot{S}_{gen_{ph_i}}$	Entropy generated in the i^{th} preheater, kW/K, $i=1,n-1$
$\dot{S}_{gen_{reg}}$	Entropy generated in regenerator of regeneration cycle, kW/K
$\dot{S}_{gen_{SJE}}$	Entropy generated in the steam jet ejector, kW/K
$\dot{S}_{gen_{turb}}$	Entropy generated in turbine of sCO2 cycle, kW/K
$\dot{S}_{gen}^{brine-RDS\to TDS}$	Entropy generated in bringing the brine to chemical equilibrium with the environment, kW/K
$\dot{S}_{gen}^{desalination}$	Entropy generation rate in the desalination system, kW/K
$\dot{S}_{genHX-3}^{reg}$	Entropy generation rate in 3rd heat exchanger for the regenerative solar cogeneration, kW/K
t	Time, s
T_{amb}	Ambient Temperature, $^\circ C$
T_c	Seawater temperature entering the MEE-TVC system
T_{cst}	Temperature of the cold storage tank, K
T_{hst}	Temperature of hot storage tank, K
T_i	Boiling temperature of the sea water in i^{th} effect, $i=1,n$, K
T_{fi}	Feed sea water temperature entering the i^{th} effect, K
T_R	Receiver Temperature, $^\circ C$
T_{v_i}	Temperature of vapor formed in the i^{th} effect, K
TBS	Top Brine Salinity, ppm
TCF	Temperature Correction Factor
TDS	Total Dead State

TIT	Turbine Inlet Temperature, $°C$
u_{cst}	Specific internal energy of the storage medium in the cold storage tank, kJ/kg
u_{hst}	Specific internal energy of the storage medium in the hot storage tank, kJ/kg
U_c	Overall heat transfer coefficient of the down condenser, kW/K
U_{cst}	Overall heat transfer coefficient of cold storage tank, kW/K
U_e	Overall heat transfer coefficient of the effects, kW/K
U_{ei}	Overall heat transfer coefficient in the i^{th} effect, kW/K
U_f	Overall heat transfer coefficient of the preheaters kW/K
U_{hst}	Overall heat transfer coefficient of heat storage tank, kW/K
UF	Utilization Factor
wr	Width to Height of heliostat, m
W_c	Compressor power input, kW
W_{c1}	1st compressor power input in the recompression cycle, kW
W_{c2}	2nd compressor power input in the recompression cycle, kW
W_{net}	Net power of the cycle, kW
$W_{net_{power}}$	Work output of the system for the whole day, kWh
W_p	Plant Capacity, m^3/d
W_s	Image dimension in sagittal plane
W_t	Turbine power output, kW
W_T	Total Lifetime Water Production, m^3

$\dot{W}_{sep}$	Work of separation, kW
$\dot{W}_{sep_{least}}$	Least work of separation, kW
$\dot{W}_{sep_{least}}^{\min}$	Minimum least work of separation, kW
x	Mass flow rate fraction flowing into the first compressor
X_{b_i}	Brine salinity for i^{th} effect
X_f	Feed seawater salinity, ppm
y_i	Fraction of the flashed vapor in the i^{th} flashbox, $i=1,n-1$
Y	Year
$Y_{comp,j}$	Exergetic fuel depletion in the j^{th} component
$Y_{comp,j}^{*}$	Irreversibility ratio of the j^{th} component

GREEK SYMBOLS

α	Absorptivity of the receiver surface
α_R	Absorptivity of the central receiver
α_s	Solar Altitude Angle, rad
ε	Emissivity
ε_{HTR}	Effectiveness of the high temperature regenerator
ε_{LTR}	Effectiveness of the low temperature regenerator
ε_R	Effectiveness of regenerator
ε_s	Effectiveness of storage heat exchanger

$\Delta \alpha z_i$	Azimuthal increment in the i^{th} zone of heliostat
$\Delta R_{\min}$	Minimum Radial Distance, m
ΔT	Temperature difference between effects, K
ΔT_e	Temperature difference across the heat transfer surface, K
δ	Solar Declination Angle, rad
η_c	Isentropic efficiency of the compressor
η_{c1}	Isentropic efficiency of the 1st compressor
η_{c2}	Isentropic efficiency of the 2nd compressor
η_{conv}	1st law efficiency
$\eta_{cog_{eff}}$	Effective efficiency
$\eta_{cog_{rec}}$	Effective efficiency
$\eta_{cog_{sep}}$	2nd law efficiency
η_{daa}	Daily Average Annual Optimization
η_{iwaa}	Insolation weighted daily averaged annually optimized efficiency
η_{maa}	Monthly averaged annually optimized optical efficiency
η_{opt}	Optical efficiency of the heliostat
$\eta_{th,R}$	Thermal efficiency of the central receiver
$\eta_{th_{power}}$	Thermal efficiency for the cycle
η_T	Turbine isentropic efficiency
σ	Stefan-Boltzmann constant, $W/(m^2K^4)$
σ_{ast}	Astigmatic error

σ_{bq}	Beam quality error
σ_h	Horizontal Gaussian error
σ_s	Mirror slope error
σ_{sun}	Sun shape error
σ_{track}	Tracking error
σ_{tot}	Total standard deviation on the receiver plane
σ_v	Vertical Gaussian error
$\cos\omega$	Cosine factor
ω_s	Hour angle, rad
ρ	Actual mirror reflectivity
ϕ	Latitude angle, rad
γ_s	Solar Azimuth Angle, rad
$\psi_{\max}$	Angular Distance, rad
$\omega_{sunrise}$	Sunrise hour angle, rad
ω_{sunset}	Sunset hour angle, rad

ABSTRACT

Full Name	:	Amine Abdullah Kouta
Thesis Title	:	Solar Cogeneration Utilizing Solar Tower Integrated with sCO2 Brayton Cycle and MEE-TVC Desalination
Major Field	:	Mechanical Engineering
Date of Degree	:	14 May, 2015

Renewable energy sources have become nowadays an efficient alternative to fossil fuels. Solar energy is one of the widely used renewable energy technologies. Recent advancement in the solar tower technology has made it an attractive choice of energy harvesting. In this study performance analysis is conducted for a solar driven supercritical CO_2 (sCO_2) Brayton cycles combined with multiple effect evaporation with thermal vapor compression (MEE-TVC) for power and desalinated water production. The study includes finding two configurations based on two different supercritical cycles, namely, the regeneration and recompression sCO_2 cycles and performing parametric studies for each. Monthly averaged study for each of the months of the year and the average for the whole year are present as well. The entropy generation evaluation for the system is also studied as well as the capital and operating cost estimation.

In this study, a new efficiency equation for the combined power and water production is developed. The study is performed over different regions of Saudi Arabia. From the energy analysis, it is found that the highest productivity is that of the region of Yanbu, followed by Khabt Al-Ghusn in the second place, and the rest are as follows, Jabal Al-Rughamah, Jizan, Al-Khafji, and Dhahran in descending order. The number of heliostats utilized is 2646. It is also deduced that the effective efficiency is the highest at

the minimum fraction possible of heat entering the sCO_2 cycle. For the area of Dhahran, this value is 0.32 for the regeneration cogeneration cycle and 0.34 for the recompression cycle at a fraction of 0.19 and 0.21, respectively. From the entropy analysis, it can be deduced that the highest contributing component in the MEE-TVC subsystem is the steam jet ejector, which is varying between 50 % and 60 % for different number of effects. The specific entropy generation in the MEE-TVC decreases as the fraction of the input heat to the desalination system decreases; and the specific entropy generation of the sCO_2 cycle remains constant entropy generation. The solar tower is the largest contributor to entropy generation in both configurations, reaching almost 80 % from total entropy generation, followed by the MEE-TVC desalination system, and the sCO_2 power cycle. The entropy generation in the two tank thermal storage is almost negligible varying around 0.3 % from total generation. The cost results reveal that the regions characterized by the highest average solar irradiation throughout the year have the lowest LCOE and LCOW values. The region achieving the lowest cost is Yanbu, followed by Khabt Al-Ghusn in the second place, and the rest are as follows, Jabal Al-Rughamah, Jizan, Al-Khafji, and Dhahran. The LCOE of Yanbu at a fraction of 0.5 for regeneration and recompression solar cogeneration cycles are 0.0915 \$/kWh and 0.0826 \$/kWh, respectively.

ARABIC ABSTRACT

الاسم الكامل: أمين عبدالله قوطه

عنوان الرسالة: تحليل لبرج الطاقة الشمسية مع دورة برايتون ثاني أكسيد الكربون فوق الحرجة ونظام التحلية البخاري المتعدّد التأثير مع ضغط البخار الحراري

التخصص: الهندسة الميكانيكيّة

تاريخ الدرجة العلمية: 25 رجب 1436 هـ

أصبحت مصادر الطاقة المتجددة في الوقت الحاضر بديل فعال للوقود الأحفوري. الطاقة الشمسية هي واحدة من التقنيات المستخدمة على نطاق واسع للطاقة المتجددة. لقد جعل التقدم الأخير في التكنولوجيا برج الطاقة الشمسية خيارا جذابا لحصاد الطاقة. تهدف هذه الدراسة نحو دمج تكنولوجيا برج الطاقة الشمسية مع دورات ثاني أكسيد الكربون فوق الحرجة (sCO2) لإنتاج الطاقة والنظام البخاري المتعدّد التأثير مع ضغط البخار الحراري (MEE-TVC) لإنتاج مياه التحلية. تتضمن هذه الدراسة إيجاد تشكيلتين اثنتين على أساس دورتين مختلفتين فوق الحرجة، وهي لدورات التجديد وإعادة الضغط (sCO2) وإجراء دراسات حدودية لكل تشكيلة باستخدام برنامج EES. دراسة المتوسط الشهري لكل واحد من أشهر السنة والمتوسط للعام بأكمله موجودة أيضا. أيضاً تتم دراسة تقييم إنتاج الانتروبيا للنظام وكذلك تقدير تكاليف رأس المال و التشغيل.

تمّ إجراء هذه الدراسة على مناطق مختلفة من المملكة العربية السعودية. من تحليل الطاقة، وجد أن أعلى إنتاجية هي في منطقة ينبع، تليها خبط الغصن في المركز الثاني، والباقي في ترتيب تنازلي كما يلي، جبل الرغامة، جازان، الخفجي، و الظهران. عدد الهليوستات المستخدمة هو 2646. ويستنتج أيضا أن الكفاءة الفعالة هي في المستوى الأعلى عند الحد الأدنى الممكن لجزء الحرارة الذي يدخل دورة sCO2. لمنطقة الظهران، هذه القيمة هي 0.32 لدورة تجديد التوليد المشترك للطاقة و0.34 لدورة إعادة الضغط في الأجزاء من 0.19 و 0.21 على التوالي. من تحليل الإنتروبيا، يمكن استنتاج أن أهم مكونات المساهمة في نظام MEE-TVC هو قاذف البخاربحيث تتراوح النسبة بين 50٪ و 60٪ لعدد من التأثيرات المختلفة. إنتاج الإنتروبيا المحددة للMEE-TVC يتناقص مع تناقص قيمة الجزء، وإنتاج الإنتروبيا المحددة لدورة ال sCO2 يحافظ على قيمة ثابتة لإنتاج الإنتروبيا.تساهم هذه النتيجة في

تأكيد نتائج الطاقة المستمدة سابقا، تتمثّل بأعلى كفاءة فعالة في الحد الأدنى لإنتاج الإنتروبيا المحددة لل MEE-TVC و دورة الsCO2 . البرج الشمسي هو أكبر مساهم في إنتاج الإنتروبيا في كل من التشكيلتين بحيث تصل النسبة الى نحو 80٪ من إنتاج الإنتروبيا الكلي، يليه نظام تحلية MEE-TVC، ودورة الطاقة sCO2. إنتاج الإنتروبيا في الخزّانين المستخدمين للتخزين الحراري هي بنسبة متدنّية جدّاً، فهي بنحو 0.3٪ من مجموع التوليد. أما بالنسبة لنتائج التكلفة، فالمناطق التي تتميز بأعلى متوسط للإشعاع الشمسي على مدار العام لديها أدنى قيمة لل LCOE و LCOW. تحقيق منطقة ينبع أدنى تكلفة، تليها خبط الغصن في المركز الثاني، والباقي كما يلي، جبل الرغامة، جازان، الخفجي، والظهران. قيمة الLCOE لينبع في جزء قيمته 0.5 لتجديد وإعادة الضغط لدورات توليد مشتركة للطاقة الشمسية هي 0.0915 $ / كيلوواط ساعة و0.0826 $ / كيلوواط ساعة، على التوالي.

CHAPTER 1

INTRODUCTION

In the continuous attempt of human kind to save energy to satisfy the needs of the growing population and to reduce the use of fossil fuels, finding efficient renewable energy systems is becoming more crucial. Being parallel in importance to the latter, cogeneration has also had its share in maximizing efficiency and minimizing waste. In this study, the topic of solar cogeneration and its efficiency is to be studied. In this chapter in particular, the motivation to the work and a general discussion of the components of such systems is to be carried out.

1.1 Energy Consumption Worldwide

When speaking of generating useful energy, it is best that we generalize the idea to include a study of the overall energy demand worldwide, which would serve as the number one motivation for this work. According to the EIA (U.S. Energy Information Administration), a 56 percent increase in world energy consumption is expected from 2010 to 2040, or in a 30 year interval. More than 85 percent of this amount is attributed to the developing nations outside the Organization for Economic Cooperation and Development (non-OECD). The OECD member countries however, are more mature energy consumers, and are described by a non-growing population and a stable economic growth. The OECD member countries are, namely, the United States, Canada, Mexico, Austria, Belgium, Chile, Czech Republic, Denmark, Estonia, Finland, France, Germany, Greece, Hungary, Iceland, Ireland, Israel, Italy, Luxembourg, the Netherlands, Norway, Poland, Portugal, Slovakia, Slovenia, Spain, Sweden, Switzerland, Turkey, the United Kingdom, Japan, South Korea, Australia, and New Zealand.

The IEO 2013 Reference case assumes that the non-OECD countries demand is the main contributor to the future energy consumption growth. It is shown that the non-OECD countries are expected, in year 2020, to consume 47 percent more energy than OCED countries, and 88 percent more in 2040, which is almost double that of the year 2020. The Middle East energy demand increase by 76 percent over the 30 years interval mentioned before [1].

1.2 Energy Consumption in Saudi Arabia

As one can understand from the previous section on global energy demand, Saudi Arabia is not listed in the OECD member countries; this implies that it is not a mature energy consuming country due to its strong industrial growth. Furthermore, it is considered as the largest oil consuming country in the Middle East. Its consumption in the year of 2012 is approximated by 3 million barrels per day. Direct burn of crude oil for power production is the major contributor to this growth. It is also estimated that the domestic demand for liquids will reach over 8 billion barrels per day by the year of 2030, which is more than double the consumption per day of the year of 2012 [1].If we go back in time to study the increase in electricity demand over the past years, an average annual growth of 14.8 percent is calculated from the year of 1975 to the year of 2001 [2]. It is also worthy of mentioning, as a motivation to the work on solar energy in the Kingdom of Saudi Arabia, that it has the largest expansion plan in the Middle East. Stated by the EIA, the generating capacity is to reach 120 GW by the year of 2020. 55 GW is to be generated by renewable energy sources, of which 41 GW is to come from solar energy [1].

1.3 Fuel Combustion Impact on the Environment

Fuel combustion is the main reason for Carbon Dioxide emissions. Carbon Dioxide is a member of the greenhouse gases like methane and water vapor. Sun, being the major source of energy for our planet, emits radiation which reaches our planet. Part of the solar radiation is reflected back and the other part heats up earth's surface. By convection, Earth heats up the air around us, and then carbon dioxide in air absorbs some heat and traps it in the atmosphere, thus causing earth to get warmer [3]. Carbon dioxide is released due to a reaction called "respiration" where human beings and animals exhale releasing CO_2 into the atmosphere. "Photosynthesis" is the other reaction in which plants absorb CO_2 from the atmosphere thus releasing oxygen into the air. Both equations were balanced along the years resulting in balancing temperature on earth until the industrial revolution in 1850 which started to increase CO_2 in atmosphere due to burning fossil fuels in several activities (cars, factories, etc.) and taking away green lands for industrial use. These activities has increased the amount of CO_2 in air reaching dangerous levels and rates, therefore leading to "Global Warming" on planet earth. Researchers on the following issue predict severe environmental problems as a result of the increase in temperature levels on earth such as the melting of both poles, rise of the sea level, health problems for humans, desertification, etc. [4]

1.4 Renewable Energy

As the demand for energy rises due to the increase in population and dependence on technological innovations, the idea of renewable energy has been sought after by mankind. It is thought of as clean energy and more importantly, a backup plan, which will serve as an alternative to insufficient natural resources predicted in the future. Examples of renewable energy are wind, sunlight, and geothermal energy etc…

In addition to the rise in energy demand, renewable energy is a major solution to CO_2 emissions and global warming stated before. Hence, the term clean energy is nothing but a synonym to the term renewable energy. It is estimated by the U.S Energy Information Administration (EIA) that 11 percent of energy consumption worldwide is satisfied by renewable energy sources. This number will increase another 4 percent to reach a predicted value of 15 percent by the year of 2040. As for the world electricity generation, 21 percent of global electricity generation in 2011 was from renewable energy sources, and it is estimated that this number will reach 25 percent by the year of 2040 [1].

1.4.1 Solar Energy

There are two ways for harvesting solar energy, solar thermal and photovoltaic. The difference between the two is that photovoltaic energy is the process of directly converting sunlight to electricity using solar panels, which means that these panels are effective in the daylight, since it is not an efficient process to store electricity. On the other hand, solar thermal energy is the process of creating heat by concentrating light from the sun. The heat harvested is used to run a cycle, it could be gas or steam, hence, electricity is generated. The advantage of thermal energy over photovoltaic energy is that heat storage is an effective and easy process allowing heat to be stored in order to run the steam or gas cycle in the night time. Having this information known, we can conclude that solar thermal energy is a better choice for large scale energy production; therefore, it will be the focus in this study.

Although we had made the choice on the way of harvesting solar energy, the applications lying within are to be investigated as well. Mainly, for large scale energy production, two types of solar thermal energy might be used, parabolic solar trough collectors, or solar tower. Although parabolic troughs or the process of concentrating heat into tubes containing thermal oil is the most dominant technology currently, the solar tower technology has the potential to be much more efficient due to the high concentration ratios compared to parabolic troughs. For the solar tower, heliostats are used to concentrate light coming from the sun onto a boiler placed at the top of the tower. The concentration ratio for the solar tower varies in the range of 300 to 800 suns (depending on the number of heliostats) versus 80 suns for solar troughs. This means that higher temperatures can be achieved by using a solar tower, and hence, reducing energy costs since higher temperatures are the way to more efficient turbines.

1.5 Supercritical Carbon Dioxide Cycles

Supercritical carbon dioxide is the state where the fluid is at or above its critical properties (temperature and pressure). At standard temperature and pressure, CO_2 behaves as a gas in air. When these properties are increased above critical temperature and pressure, the fluid behaves as a gas but with a relatively high density, which can achieve high efficiency if entered in a gas turbine at temperatures near 500 degrees Celsius and a pressure of 20 MPa. The efficiency of such cycles can reach 40 percent and even more, which is considered to be very high. Another main advantage of such cycles is the relatively reduced compressor work. Other advantages for using CO_2 at supercritical conditions include high efficiency at low temperatures, relatively small sized components due to its high operating pressures, the abundance of the gas, and its low cost [4]. Hence, we could say that it is a good choice if a supercritical carbon dioxide cycle is integrated with the studied system. A study for different configurations of these cycles will be carried later in this study.

1.6 Thermal Heat Storage

Given the change in energy output from a solar collector due to the change in solar incidence angle and sky clearance, the idea of delivering steady non-fluctuation heat input to the cycle arises. Not only has the problem of output fluctuation been the only obstacle, but also the fading of sunlight during night time. Thermal heat storage serves as a solution to this problem. It uses molten salt as a working fluid to store heat from the solar collector. The delivery of heat to the cycle is thus moderate and non-changing at night time and non-clear daytime.

1.7 Cogeneration

Another attempt to save energy is making use of the waste energy for process heating, like waste energy from gas turbines in gas cycles, usually referred to as cogeneration. Instead of losing the waste energy to the atmosphere, it is used to generate useful products, such as electricity from a bottoming steam cycle which can operate on relatively lower temperatures, or for water desalination, where the rejected heat is used to produce distilled water from seawater. Cogeneration which is known as “Combined Heat and Power”, simply saying CHP, is a process for generating power and heat from the same fuel source. According to US Environmental Protection Agency (EPA), CHP results in several benefits of major interest in environmental aspects. Advantages do include a more overall efficient performance (75%) than the conventional method (51%) where heat is being wasted as a result of separate power and heat. Efficiency of high value translated to environmental benefits reduces the emissions of greenhouse gases (CO_2, NOx, SO2, etc.) because less fuel will be used which is also an advantage reducing costs. EPA shows that for generating energy of 5 MW output for 1 year, CHP emits 23 kilotons of CO_2 while separate heat and power system emits 45 kilotons of the same gas. The ability of providing not only electric power but also thermal energy makes CHP a reliable source against the risk of outages and failure of sensitive equipment. EPA lists the common types of CHP systems to be “Gas Turbine or Engine with a Heat Recovery Unit” and “Steam Boiler with Steam Turbine”. First system, used for large industries requiring large amount of electricity, burns fuel in the gas turbine to generate electricity while heat exhausted is converted to thermal energy by a “Heat Recovery Unit” to be then applicable for usage. The second system, a different system, uses solid fuels such as coal or biomass to generate heat and electricity, but this time electricity being a by-product of heat generation. Much use of CHP technology can be applied for glass manufacturing, hotels, hospitals, food processing, airports, etc. [5]. Thus, we could use the waste energy exiting the gas turbine to utilize it in process heating, in this case, thermal desalination which will be introduced in the following section.

1.8 Thermal Desalination

There are several kinds of thermal desalination. Single effect desalination, multiple effect desalination, and Multistage flash desalination [6]. Due to its low gain output ratio, single effect desalination is disqualified from being an option unless used for micro scale applications such as for domestic use. The reliability, huge capacity, and simplicity of the multistage flash desalination system, made it an attractive option, especially in the gulf region, which accounts for 94 percent of the water production in this region, while MED with thermal vapor compression (TVC) accounts for the 6 percent left [7].

Recent technologies, however, made MED-TVC competitive to MSF and a well proven and reliable technology. Some of the advantages of the MED-TVC are that pretreatment requirements are minimal and the high operating flexibility; the cost of the plant is independent of the salinity, a high overall heat transfer coefficient is provided by MED-TVC compared to MSF, and most importantly, the relatively low power consumption and high performance ratio. The use of a steam jet ejector increases the gain output ratio substantially compared to MEE desalination system. This encourages the choice of using the MED-TVC technology in the cogeneration system in this study.

1.9 Second Law Analysis

Optimization of such systems is achieved by analyzing these systems from a second law perspective, which is to introduce entropy generation analysis. It is useful, however, to quote the words of Max Planck on the interpretation of the second law of thermodynamics. He stated, "*Every process occurring in nature proceeds in the sense in which the sum of the entropies of all bodies taking part in the process is increased. In the limit, i.e. for reversible processes, the sum of the entropies remains unchanged*."

The most popular definition of entropy is the measure of disorder in a system; in a somehow same fashion, entropy generation can be thought of as a measure of disorder during a certain process. From here rises the answer why an ideal system does not exist. Assume we have two books with the same content; the first book contains no table of contents, nomenclature, or appendix; on the contrary, the second book is well organized and contains them all. The first book is said to have high entropy, while the other is described to have relatively lower entropy, but this does not imply that the second book is ideal. As a matter of fact, it is not even close to idealism; it only implies that the same reader of both books will take longer time to grasp the concept using the first book, hence, if compared to thermodynamic systems, it can be said that the second system is more efficient and has a better performance than the first system. Matter tend to pass from a lower state entropy to a higher state entropy, that’s how God created things, even when otherwise designed by mankind to have a lower entropy, it will be on the expense of the entropy increase of the system interacting to create the organized low entropy form of matter. Every single thing has its life span, even our planet earth. Here comes the role of human beings, which consists of maintaining a low entropy life form through the manipulation of matter to produce systems of optimized performance and guarantee maximum evolution.

For a quite long time now, human beings have been seeking different sources of energy and developing a variety of methods to maintain these energy sources. One of the methods of maintaining energy of whatever form it might be is to reduce the unnecessary energy loss. Reduction of energy loss can be accomplished through a wide variety of selections ranging from geometrical changes (i.e. the change of a car's body from a rough square-shaped profile to a smooth aerodynamic friendly body which allows the reduction of air resistance) to system optimization through entropy generation minimization. Entropy generation minimization is an optimization method of thermodynamic systems. Entropy is generated due to fluid flow, heat transfer, and mass transfer irreversibility [8]. The irreversibility is minimized by simultaneously studying all the aspects mentioned and their effect on the system, and finding the optimum design which results in a minimum entropy generation, which implies, minimum heat is lost into entropy production, hence, enhanced efficiency. The performance of thermal systems is determined by entropy generation (e.g. refrigerators, air conditioners, heat engines, and power plants). In a closed system, entropy is produced due to heat transfer and irreversibility, while in an open system; the flow of mass contributes to the entropy production as well.

1.10 Motivation and Significance of the Work

In light of what was discussed in the previous sections of this chapter, it is obviously deducted that the energy demand follows an increasing scale with respect to time. It is, however, inevitably true that the use of fossil fuels is still the most widely spread power generating technology since its discovery. This is due to its abundance which, on the long term, is not scientifically guaranteed since a non-renewable source is judged to extinction by its definition. Another characteristic for fossil fuels or fossil fuel based systems is its relative independence of weather and environmental changes and its steady operation with respect to renewable sources. On the other hand, renewable energy sources are, quite the contrary to fossil fuels, sentenced to a non-ending abundance. Another advantage is its friendly impact on the environment, since unlike fossil fuels, no carbon dioxide gas emission results from it, and hence, it has no negative effect on the global warming as discussed in an earlier section. Subject to that, it is of great importance to direct research effort towards the study of renewable energy systems, its applications, and performance.

Another topic of importance is the dual purpose plant consideration, or cogeneration. Serving indirectly in the favor of the previously discussed, cogeneration uses the remaining energy from power production to supply process heat. It serves in the favor of the previously discussed since if it were not for the waste heat being used, process heating would be fed from a direct source which would result in a greater demand for energy. Thus, an effort in this direction is as well favored.

To make use of renewable energy, the use of a concentrated solar power technology is adopted in the study. As stated in earlier sections of this chapter, the choice of the type is well dependent on the performance and cost of the concentrating solar power technology. The solar power tower's superior performance and reduced prices due to recent technological developments renders it more attractive than other options[9]. The solar power tower's high achievable temperature due to its high concentration ratio makes it a system of choice.

The choice of a thermodynamic cycle is as important in the study as the choice of the CSP system. To make use of the high temperatures achieved by the solar tower, supercritical CO_2 cycles are the choice in the system under study. Due to low compressor work and real gas behavior near the critical point, its thermal efficiency reaches values above 50 percent for the temperatures achieved by the solar tower. The high operating pressures of this working fluid allows for smaller components of the system and a lower cost.[4]

Furthermore, to make use of the waste energy, a desalination system should be integrated in the system. The choice of MED-TVC desalination unit is an attractive choice over the well spread MSF technology in the Gulf area due to its thermodynamic superiority and recent technological improvements. Also, unlike MSF desalination, MED technologies are better suited for a fluctuating energy input for its operation.[10]

Further elaboration on the choice of components, their feasibility, and a detailed review of past work is carried out in the following chapter.

1.11 Thesis Objectives

The objective of this thesis is to carry out a parametric analysis of the performance of a solar cogeneration system using solar tower technology integrated with supercritical CO_2 cycle and multiple effect evaporation desalination system.

The specific objectives are:

1. Finding two configurations for the cogeneration system based on two different supercritical CO_2 cycles.
2. Developing a mathematical code for each configuration to perform the thermodynamic and cost analyses.
3. Monthly averaged study for each of the twelve months of the year and an average evaluation for the whole year for selected cities in Saudi Arabia.
4. Entropy generation evaluation for the system components and a study of the total entropy generated for different operating conditions.
5. Capital and Operation & Maintenance cost estimation for the systems under study.

CHAPTER 2

LITERATURE REVIEW

The purpose of this chapter is to present a survey for previous work done in the area of solar power generation and cogeneration and the advancements that one should take into consideration in the attempt to make a progress towards new configurations. Though it was stated in the previous chapter, in general, the different types of each component that a solar cogeneration plant must have and a preliminary choice was made on that basis, the purpose now is to elaborate more on the subject of each component.

We stated in the previous chapter how it was preferred utilizing solar power tower over parabolic trough solar collectors due to the high temperatures the solar tower can achieve compared to the latter. It was also stated that in order to make efficient use of that energy, we need to operate the cycle in a steady state non-fluctuating input, thus, we made it clear that the use of a thermal storage is inevitable. Moreover, having known that the supercritical carbon dioxide gas cycle achieves high efficiencies for high turbine input temperature, we found it a choice of significance given the advantage of high temperature input from the solar tower. Furthermore, to make use of waste energy from the gas cycle, cogeneration was proposed, and waste heat was to run a desalination system. MED-TVC was chosen for its relatively high gain output ratio and for the recent technological advancements which made it competitive to the conventional widely dominant MSF (multistage flash) desalination in the gulf area.

The survey will be split into parts discussing concentrating solar thermal power with emphasis on solar tower, supercritical gas cycles and CO_2 cycles in particular, thermal desalination plants and MED-TVC, and solar cogeneration plants. At the end, the general choice of components will be confirmed and an identification of certain configurations to be studied will be made possible.

2.1 Concentrating Solar Thermal Power

Atif and Al-Sulaiman [11] tackled the problem of solar thermal tower integrated with different supercritical CO_2 cycles, a thermodynamic study is presented and a mathematical model dealing with generating a heliostat field in a radial staggered configuration is developed. The optical performance of this field is evaluated. The central receiver receives the collected heat from the heliostat field where it is used to run the supercritical CO_2 cycles. The study is based on solar radiation in the area of Dhahran in Saudi Arabia. The optical efficiency as shown in this study is a function of the reflectivity of the heliostats, cosine factor, shading and blocking factor, intercept factor, and the atmospheric attenuation factor. The study also accounts for the radiation and convection losses from the receiver. The supercritical CO_2 cycles used in this study are, namely, the regenerative and recompression Brayton cycles. It is also worthy to note that the regenerative showed a higher efficiency.

Collado et al. [12] studied the flux density due to a focused heliostat over the solar tower receiver. An assumption of a continuous and spherical surface is made. An exact convolution is obtained in this study and was confirmed by experimental measurements taken from four heliostats. The analytical flux density function is considered to be relatively simple and flexible. It is concluded as well that the function has a closed form, thus, giving it an advantage over other models for optimization purposes. Later on, Collado et al. [13] used the flux density function along with another function based on simplifying assumptions to derive a new simplified procedure to evaluate the annual energy that a defined heliostat field produces. the assumptions used to derive the procedure are a radial staggered configuration, constant azimuthal spacing through the field, two shoulder heliostats only are used in the first row to calculate blocking, and shading was excluded from the study. A constant blocking factor, a constant azimuthal separation, and the tower height define the density function. The integral over the overall domain of the field of the product of the flux density function and the function based on simplifying assumptions is the annual energy produced. Collado [14] presented a simplified model of the annual overall energy collected by a surrounding heliostat field. This model allows for quick evaluation of the annual overall energy. The simplified model, as stated by the author, is valid for preliminary optimization. It is also concluded that preliminary results from this simplified model is to be later on verified in a full optimization process. Shading and blocking should be studied further due to its simplicity in this model. In a later work, the same author [15] addressed the difficulty of generating a discrete layout of a large number of heliostats. He managed to use two parameters, simplified blocking factor and an additional security distance, to define thousands of heliostat coordinates. Recently, Collado and Guallar [16], [17] presented the ability of a code in calculating the shading and blocking factor for each heliostat in the field. Maximum annual energy is searched in this code called Campo assuming the worst shadowing and blocking factor.

Benammar et al. [18] developed a model to study the performance of solar tower power plants based on energy analysis excluding energy storage from the study. The system is divided into four main subsystems, the heliostat field, receiver, steam generation, and power cycle. Numerical optimization is implemented to solve a general nonlinear mathematical model of the system under study. The steam mass flow rate and receiver efficiency dependence on the receiver surface temperature and surface area is studied.

Xu et al. [19] studied the solar power tower system using energy and exergy analysis. The study is carried out using molten salt as a heat transfer fluid. In order to locate the thermodynamic imperfections, energy and exergy losses for each component were evaluated. The effect of normal irradiation, concentration ratio, and power cycle type on energy and exergy is also analyzed. The maximum loss in exergy was shown to occur in the receiver system, and the heliostat field exergy loss comes second in classification. It was also found that the increase in direct normal irradiation increases the energy efficiency. Reddy et al. [20] analyzed a central tower receiver solar thermal power plant with air cooled volumetric receiver analytically by exergy analysis. Energy losses, exergy losses, and efficiencies are calculated. The calculation is specifically carried out for the location of Jodhpur, India. The unit cost of electric energy is also investigated for this location. Electrical energy generation for each month of the year is also found in the results.

Franchini et al. [21] studied the performance of a solar Rankine cycle and an integrated solar combined cycle combined with two solar field configurations, namely, the power tower, and parabolic trough solar collector. Real operating conditions on a one hour basis were used to calculate the plant performance. For the integrated solar combined cycle plant, a commercial gas turbine with heat recovery steam generator was assumed, whereas, for the solar Rankine cycle, a single reheat regenerative Rankine cycle was chosen. The heat transfer fluid considered in the study is molten salt to transfer heat to the solar Rankine cycle, and for the integrated solar combined cycle plant, synthetic oil was chosen. The effect of the concentrating solar power technology on the solar energy conversion efficiency was the main focus of comparison in this study. Thermal power of the parabolic trough collectors versus solar tower is assessed. The highest annual solar to electric efficiency of 21.8 percent was attained by the integrated solar combined cycle with the solar tower. It is stated as well that the solar tower has a higher collection efficiency and conversion efficiency when compared to parabolic trough collectors.

In addition to the efficiency and conversion ratio advantage solar towers have on parabolic trough collectors as stated by Franchini et al. [21], the working fluid , currently molten salt, can reach a temperature of 600 degrees Celsius. It is well known that the higher the temperature the higher the cycle efficiency. Moreover, the thermal storage is more attractive to utilize thermal storage. Thus, the preliminary choice made in the Introduction section is verified in this chapter of the study.

2.2 Brayton Cycles and Supercritical CO_2 cycles

Dunham and Iverson [22] provided a review of high efficiency thermodynamic cycles applied to concentrating solar power systems. Focus was given to single and combined high efficiency cycles. The considered cycles in this work were, the regenerative Brayton cycle, recompression Brayton cycle, combined Brayton-Rankine cycle, and the steam Rankine cycle. The regenerative He-Brayton cycle shows no effect for pressure change over thermal efficiency, instead, it had a great dependence on temperature and it reached an efficiency of 55.7 percent. In the study, carbon dioxide recompression Brayton cycle showed an outstanding high effieciency exceeding 60 percent at a pressure of 30 MPa and temperature of 1000 degrees Celsius. Liu et al. [23] proposed a new type of solar energy based power generation system. The power cycle in the study assumes supercritical carbon dioxide as the working fluid and the supercritical cycle is integrated with high temperature heat storage. Compared to steam systems, the system showed significantly high solar energy conversion efficiency, and the heat storage is found to improve the overall efficiency of the system. It was shown as well that the higher temperatures and pressures are, the more favorable it will be for power generation and energy storage.

Neises and Turchi [24] studied the recompression and partial cooling cycles with a more detailed heat exchanger model. The integration of these cycles with concentrating solar power technology is also carried out. Across the primary heat exchanger, it was shown that the partial cooling cycle offers a larger temperature difference which reduces the heat exchanger cost and improves the concentrating solar power receiver efficiency.

Chacartegui et al. [25] proposed the use of supercritical and transcritical carbon dioxide cycles for the application related to concentrated solar thermal power plants. The cycles considered in this study are, a stand-alone closed recuperative Brayton cycle, a two stage compression Brayton cycle, and a combined cycle assuming carbon dioxide cycle as a topping cycle and organic Rankine cycle as a bottoming cycle. The second cycle assuming two-stage compression resulted in a better performance among the two gas cycles considered. The analysis of the combined cycle shows that there is no significant advantage in utilizing recuperative ORC systems due to low heat recovery vapor generator efficiency.

A very important study was carried out by Kulhanek and Dostal [4]. They analyzed and compared a number of supercritical carbon dioxide cycles. These cycles included the following, the simple Brayton cycle, pre-compression cycle, recompression cycle, split expansion cycle, partial cooling, and partial cooling with improved regeneration. It was found that, at a constant compressor and turbine inlet temperatures of 32 and 550 degrees Celsius respectively, the pre-compression cycle reached an efficiency of 44 percent at an outlet compressor pressure of 10 MPa. The recompression cycle was found out to reach the highest efficiency of 45 percent for a compressor inlet pressure of 7.7 MPa and an output pressure of 20 MPa. Results are found in simple graphs illustrating the thermal efficiencies of each cycle for different turbine inlet pressures and different pressure ratios. It was concluded from this study that the behavior of the split expansion cycle is close to that of the recompression cycle but not as efficient. Though the partial cooling cycle with improved regeneration reaches higher thermal efficiency, but it is concluded that the overall cycle is complex pinch point problems within the recuperator might occur.

Trela et al. [26] analyzed the efficiency of two transcritical CO_2 power cycles with regenerative heaters. The operating temperature and pressure is set in the ranges of 600 to 700 degrees Celsius and 40 to 50 MPa respectively. Maximizing the cycle efficiency through optimization of pressure and mass flow in the regenerative heaters is the purpose of the study. An efficiency of 51-54 percent is achieved. It was found comparable to the results found by Dostal [27] in the comparative study on different supercritical cycles for utilizing in nuclear reactors.

A numerical study was conducted by Zhang et al. [28] on a Rankine cycle powered by solar energy for heat and power production; the working fluid is supercritical carbon dioxide. The annually averaged power generation and heat recovery efficiency were found to be 22.2 and 68 percent respectively.

2.3 Desalination and MEE-TVC

Fosselgard and Wangnick [29] tackled the problem of capital and operating costs for seawater desalination plants. In their study, they presented formulas for calculating the capital costs as well as parameters for evaluating the operation costs. Detailed calculations for each case are carried out. The multiple effect evaporation was found to be, in general, the cheapest. ME-TVC was found to be superior to the MSF system. However, the Mechanical vapor compression was found to be the most expensive. It is also shown that changing the fuel and electricity price has a huge impact which can change the results found, for example doubling the price of fuel and halving that of electricity renders reverse osmosis more attractive than the multiple effect evaporation, which in this case becomes the most expensive.

A recent study done by Mutaz and Wazeer [30] focused on developing a mathematical model of MEE-TVC system. Though the same study was carried out by Bin Amer [31] which will be discussed in the following paragraph, this study includes the effect of the NEA (non-equilibrium allowance) on the temperatures in the system. Also, while this study uses a Matlab code to evaluate the system performance, Bin Amer [31] used EES (Engineering Equations Solver) to carry out the calculations. None the less, the latter, as will be discussed later, used Matlab software for optimization.

Bin Amer [31] developed a mathematical model of the ME-TVC desalination system. Optimization was also carried out to determine the optimum operating and design conditions. Three commercial multiple effect thermal vapor compression units were used to validate the results derived from the model. In the range of 4 to 12 effects, the maximum gain ratio was found to be 8.5 and 18.5 respectively. The top brine temperature is in the range of 55.8 and 67.5 degrees Celsius; optimal results for compression ratio are in the range of 1.81 to 3.68, and that of the entrainment ratio are in the range of 0.73 to 1.65. Two optimization approaches were considered, smart exhaustive search method, and sequential quadratic programming. The results for optimum operating parameters are tabulated for different number of effects. A later study using response surface methodology and partial least square technique to analyze and optimize the multiple effect desalination with thermal vapor compression was performed by Esfahani et al. [32]. The paper presents an investigation of parameters such as the temperature difference, motive steam mass flow rate, and preheated feed water temperature on the system's performance. The total annual cost, gain output ratio, and fresh water flow rate were calculated using mathematical and economical models based on exergy analysis. Minimizing the total annual cost and maximizing the gain ratio was performed for different number of effects using multi-objective optimization. The study covered systems with 3, 4, 5, and 6 effects. Among the systems studied, the system with 6 effects is the most cost effective since it has the lowest unit product cost and largest GOR compared to the rest of the systems according to the results. The analysis showed that the

6 effects system reduces the unit product cost by 14, 12.5, and 2 percent and increases the gain output ratio by 50, 34, and 18 percent compared to systems with 3, 4, and 5 effects respectively.

In a similar approach to the previous studies, Kamali et al. [33] worked on the parametric optimization for multiple effect evaporation with thermal vapor compression. His study focused on increasing the gain output ratio of the system. Effect of different parameters on key results such as performance ratio, total capacity, and temperature difference between effects is carried out. A similar study by Samake et al. [34] was also performed for multiple effect evaporation with thermal vapor compression. The dependence of key values such as motive flow rate, seawater flow rate, total produced distillate, specific heat consumption, and exergy destruction on design variables such as motive fluid pressure, compression ratio, condenser temperature pinch, ratio of seawater rejected to that supplied is investigated. It was concluded that the increase in the ratio of seawater flow rate feeding the system to the total supplied does not affect the motive fluid mass flow rate and amount of heat that needs to be supplied but it increases exergy destruction. It was also concluded that an increase in CR (compression ratio) decreases energy consumption, total supplied seawater flow rate, and total distillate. The increase in motive fluid pressure decreases heat consumption, motive steam flow rate, distillate flow rate, and total supplied seawater flow rate.

Shakouri et al. [35] studied two cases of multiple effect desalination systems integrated with gas turbine. The feasibility of integration of these systems with the gas turbine is also investigated. Both cases were coded in EES software and optimization was carried out in GAMS (Generalized Algebraic Modeling System).

Alasfour et al. [36] studied three cases of multiple effect evaporation, the conventional system, the system with regenerative feed heaters, and multiple effect evaporation with thermal vapor compression coupled with the conventional system. The first and second law thermodynamics are covered in the analysis. The system's performance dependence on different parameters such as the motive steam pressure, temperature difference between effects, seawater temperature, flow rate of motive steam, and top brine temperature are investigated. It was also concluded that the exergy destruction were mainly from the irreversibility in the steam ejector and the evaporators. The second case was concluded to have the highest gain ratio and lowest specific heat consumption; though it was expected in the paper that the third case would have the best performance, this result was attributed to two reasons, the first one to be the greater number of feed preheaters to each effect, and the small difference between the temperature entering the effect and the boiling temperature. The third case though, has the lowest specific heat transfer area and a low compression ratio allowing the utilization of a lower amount of motive steam. It is useful to note that the second case is similar to the one analyzed by Bin Amer [31] and Mutaz and Wazeer [30] discussed earlier in this survey.

In an earlier study, Dessouky et al. [37] studied the performance of mechanical vapor compression and thermal vapor compression multiple effect evaporation desalination system. The focus of the analysis was on parameters affecting the cost of the system such as the specific heat transfer area, gain ratio, conversion ratio, cooling water flow rate, and specific power consumption.

Kouhikamali et al. [38] studied the effect of changing the position of the thermo-compressor within the MEE-TVC desalination system. It was shown that the entrainment ratio is highly affected by the variation in the suction pressure. A decrease in energy consumption was shown when thermo-compressor position is changed from the conventional last effect to the middle effects.

Choi et al. [39] tackled the improvement of the MEE-TVC system through exergy analysis. It was concluded in his study that the share of exergy destruction for the vapor compressor and the effects is more than 70 percent from total. It was also concluded that a 120 percent increase in the entrainment ratio resulted in a 12 percent decrease in the total heat transfer area.

Thermoeconomic analysis of different desalination plants was carried out by Mabrouk et al. [40]. Cost is estimated on an exergy basis. Exergy destruction for components within the system is also calculated. This facilitates the identification of components with the highest exergy destruction costs. Lower unit product cost appeared to be resulting from MVC and reverse osmosis.

A comparison between MSF and MEE-TVC desalination systems was carried out by Darwish and Alsairafi [10]. In this paper, it is intended to show why MEE-TVC systems are becoming favorable and comparative to the widely spread MSF desalination systems. MEE-TVC has the advantage of operating at relatively low top brine temperature which reduces corrosion and scale formation. Other advantages of MEE-TVC over MSF include its response to fluctuating steam supply, less energy for pumping, and the flexibility of operation off the design. As stated before, it is concluded that treatment of feed water to avoid scale formation and corrosion in MEE-TVC costs less than that of MSF since MSF operate at high top brine temperature (90-110 degrees Celsius) compared to MEE-TVC which operates at 63 degrees Celsius top brine temperature.

In an attempt to study the feasibility of integrating a four unit multiple effect evaporation TVC desalination system with the Azzour South cogeneration plant in Kuwait, Alasfour and Alajmi [41] performed a parametric analysis involving the compression ratio, temperature difference between stages, and the number og stages assumed on the performance of the thermal vapor compression desalination system.

Probabilistic modeling of CSP technologies has been carried out by Ho et al. [42]. The quantification of uncertainties and their effect on the performance and cost of the system is one of the advantages of the probabilistic modeling.

2.4 Cogeneration Systems

Rheinlander and Lippke [43] tackled the problem of solar tower power plant with PHOEBUS receiver for cogeneration of electricity and water. For the power production, a Rankine cycle was utlilized. Different configurations were studied and it was found that the cost of water from the systems studied is comparative to other non-solar energy driven systems. An additional environmental benefit summarized by a 50 percent reduction in CO_2 emissions was also observed. A cost comparison is also present.

Prengle et al. [44] studied a solar energy cogeneration power plant based on a central receiver-AHS with a chemical storage allowing the system to run for both, daytime and at night. 46 percent efficiency is shown to be achieved. The case of a 100 MWe cogeneration power plant and its analysis is discussed in detail in the paper. Preliminary capital costs are evaluated and found competitive to non-renewable energy systems.

Hoefler et al. [45] studied the design of a cogeneration solar power plant to produce power and fresh water in a desert area in Kuwait. Parabolic collectors are utilized for harvesting solar energy. Synthetic fluid is used within the collectors where it reaches 400 degrees Celsius. A radial flow turbine is operated for electric energy generation, and rejected heat is used to run a multistage flash desalination system.

McDonald [46] proposed a power plant concept utilizing a combined closed cycle for energy conversion fed by a solar receiver system described by parabolic dish reflectors with centralized prime mover and mounted heat exchangers.

Alrobaei [47] identified the effectiveness and thermodynamic performance of different proposed concentrating solar cogeneration power plant configurations. The study is aimed towards evaluating the potential of integrating these systems with reverse osmosis or multiple effect evaporation desalination. A computational model was developed for this purpose. The dependence of the thermodynamic effectiveness of these configurations on key parameters is addressed as well.

Soltani et al. [48] performed an exergo-economic multi-objective optimization for a solar hybrid cogeneration cycle utilizing the solar power tower technology. The target of the multi-objective optimization is the exergy efficiency and the product cost. The study resulted in a 48 percent reduction in fossil fuel consumption for optimized input variables. The economic outcome, as expected by the author, was found disadvantageous, for the cost of the system rises by 87 percent compared to the conventional system utilizing only fossil fuel as an energy supplier.

Giuliano et al. [49] analyzed different solar-hybrid power plant configurations. The analysis was carried out on a yearly basis with different storage capacities and solar field sizes. A comparison is also present for all the cases with each other and with a conventional fossil fuel fed combined cycle.

It is also worthy to mention that the Spanish institution, PSA (Plataforma Solar de Almeria) is an active institution for studying the feasibility and design of cogeneration systems for power and water production. PSA studied and demonstrated the Aquasol 1 project developed in Australia. A study by Hardiman et al. [50] presents the Aquasol project design capabilities and its feasibility and advantage in delivering cost effective, efficient, and environmentally friendly function. The use of compound parabolic concentrators is adopted along with boilers utilizing fossil fuels integrated with a combined cycle gas turbine power plant. Part of the superheated steam formed in the system is directed to a multiple effect desalination unit for water production. The brine removed from the system is to be utilized as well in salt fields for salt production. In another project for PSA, Rodriguez and Galvez [51], studied the project POWERSOL. The purpose of the project was to develop a cost effective and environmentally friendly power generation technology integrated with a solar thermal energy source of energy. Experimental testing of the thermodynamic cycle is used for optimization with different working fluids and solar collector prototypes. Instead of utilizing MED like Aquasol [50], reverse osmosis technology is utilized for POWERSOL [51] and the different soar thermal prototypes used in the study are flat plate collector, CPC, and parabolic trough collector. Another cogeneration project utilizing reverse osmosis technology for water production is the MEDOSOL project, which is also developed at PSA. The MEDOSOL project is studied by Galvez et al. [52]; The study utilizes an advanced compound parabolic solar collector.

Modeling and optimization of a cogeneration conceptual system is studied by Ghobeity et al. [53] utilizing a regenerative Rankine cycle with an extracting turbine for power and process steam generation. The desalination systems involved within are both reverse osmosis and multi effect distillation systems. However, Non-conventional solar harvesting and storage is considered in the study. Unlike the conventional solar towers studied by Ortega et al. [54], Romero et al. [55], and Alpert and Kolb [56], or the prototypes with secondary reflectors and concentrators tackled by Yogev and Epstein [57], Blackmon et al. [58], and Segal and Epstein [59], the present approach utilizes the concentrating solar power on demand (CSPond technology) studied by Slocum et al. [60] which, in a brief description, is a concentrating solar energy system which uses hillside mounted heliostats and reflects sunlight onto a volumetric receiver containing molten salt referred to as a salt pond. The dual purpose receiver of absorbing solar energy and storing it as well is an attractive advantage the system has since the use of external hot and cold storage tanks can be eliminated.

The solar energy and reversible solid oxide fuel cell application and analysis in a cogeneration is carried out by Akikur et al. [61], [62]. Power and steam electrolysis and electricity as well is produced from solar energy and hydrogen production from solid oxide fuel cell; the generated hydrogen fuel is used for heat generation. In the performance analysis, the cogeneration system's mathematical model is developed. The system is studied for three different modes depending on the solar radiation intensity. The system's performance dependence on the solar radiation and temperature is investigated as well. The combined heat and power efficiency for the different modes studied has been calculated and an economic analysis of the system based on its yearly electricity generation has also been investigated.

The performance of a cogeneration system producing electricity and fresh water has also been studied by Li et al. [63]. The system studied, however, uses the parabolic trough solar collector technology for solar energy harvesting and a supercritical organic Rankine cycle to produce electricity. The desalination unit proposed in the study is the reverse osmosis desalination unit. Two different modes of operation are studied depending on the variation in incident radiation; the modes are, electricity generation only, and water-electricity cogeneration.

El-Nashar [64] studied the performance of several cogeneration systems integrated with MSF technology. An optimum cogeneration selection methodology is described, and the allocation of costs between electricity and water is achieved by the exergy analysis method. It is concluded from the study that the optimum cogeneration scheme depends highly on the power to water ratio. In a later study, El-Nashar [65] studied the optimal design of cogeneration systems for power and desalination taking into consideration the equipment reliability. It is seen that the equipment reliability consideration leads to higher products costs.

Hajeeh et al. [66] provided a mathematical optimization model that minimizes the operational cost of cogeneration systems for a specified time and for a set of constraints. Perz and Bergmann [67] studied the feasibility of integrating water and power supply with renewable energy in the MENA region.

Lianying et al. [68] targeted the minimum total annual cost through the use of a detailed mathematical model for cogeneration systems for power and water production. It can be seen from the study that the water demand affects the optimal pattern of the cogeneration system.

Iaquaniello et al. [69] proposed alternative scheme for power and water production by the proper integration of CSP with MED and RO desalination processes. RO is run by an amount of electricity from the turbines while MED is run by the exhaust steam from the back pressure steam turbine. The integration serves in increasing the RO feed temperature with increasing permeate flow and an increase in the flexibility of its operation. It also allows for the continuous operation increasing the reliability of the plant.

Altmann [70] carried out the definition of the most suitable technique for producing water with the lowest prime energy consumption from a first law perspective and introduced a new concept for power and RO cogeneration.

El-Nashar [71] proposed two different methods for cost allocation in a cogeneration plant, the exergy cost accounting method, and the indirect cost allocation method. It is found that the exergy method results are more reliable.

Safi and Korchani [72] carried out the measurement and comparison of two desalination low-temperature technologies, MSF and MED in dual purpose operation for production of water and power based on gas turbines. It is found that an increase in water production quantities is encountered with the increase in the power plant. Shakib et al. [73] modeled a dual purpose plant consisting of a gas turbine with and without a preheater, an HRSG, and MEE-TVC. It can be seen from the study that by applying the multi-objective genetic algorithm, a decrease in the total products cost is achieved and the exergy efficiency increases for the system utilizing an air preheater.

2.5 Summary

An extensive literature review has been carried out in the previous sections. It can be seen that throughout the solar cogeneration review, a variety of systems has been studied including a variety of CSP technologies integrated with different cogeneration systems for electricity and water desalination (including both membrane, and thermal desalination systems). However, the idea of integrating solar tower with supercritical CO_2 cycles along with MEE desalination for cogeneration of electricity and water has not been yet studied in details. Therefore, the research in this discipline is original in the extent that it has not yet been studied in details for its feasibility and performance, and it is the focus of this study.

CHAPTER 3

MATHEMATICAL FORMULATION

The previous chapters in the study included an introduction and a literature review of each component of the configuration to be studied and the configuration as a whole. This chapter will include the mathematical formulation for each of the components of the system. The mathematical formulations are to be employed in a computer code to help facilitate the study of the system. The validation of the computer codes aiding the analysis, if found in the Literature, are also present in this Chapter.

Moreover, this chapter will be divided into several parts. The first part will shed light on the mathematical model related to the solar tower, its optical performance based on the study of Atif and Al-Sulaiman [11], and its receiver efficiency. Previously stated in the literature review, the optical performance in their study is calculated using five parameters, the cosine efficiency, atmospheric attenuation factor, shadowing and blocking factor, intercept factor, and the actual mirror reflectivity. The second part will be assigned to the mathematical modeling of the two sCO_2 cycles that will be integrated to the solar tower, namely, regenerative and recompression sCO_2 cycles. Later on, the mathematical modeling for the heat storage will be discussed, and the modeling of the MEE-TVC desalination system based on the study done by Bin Amer [31] on their performance and optimization will also be presented. Finally, the configurations to be studied are presented and the entropy equations for the two configurations are discussed as well.

3.1 Solar Tower

The following section is a discussion of the optical efficiency and the receiver efficiency mathematical formulation. The modeling of the heliostat field including the characteristic diameter, the radial spacing, the azimuthal spacing, number of heliostats, and the optical efficiency of the heliostat field will be discussed briefly. The mathematical formulation was discussed by Atif and Al-Sulaiman [11].

3.1.1 Modeling of the Heliostat Field

A radial staggered configuration is utilized to generate a preliminary heliostat field. Methods for calculating the components stated above are found in this subsection.

The Characteristic Diameter

The characteristic diameter is defined as the distance between the centers of the adjacent heliostats. It is calculated as,

$$DH = \sqrt{1+wr^2}LH \tag{1}$$

$$DM = DH + dsep \tag{2}$$

where DH is the heliostat diagonal, wr is defined as the ratio of the width to the height of the heliostat, LH is the height of the heliostat, $dsep$ is the additional security distance between the heliostats, DM and is the characteristic diameter.

The Radial Spacing

The radial spacing is defined as the distance between two heliostat rows. The minimum radial distance is the height of an equilateral triangle combining the centers of three adjacent heliostats shown in the configuration (Figure 3.1).

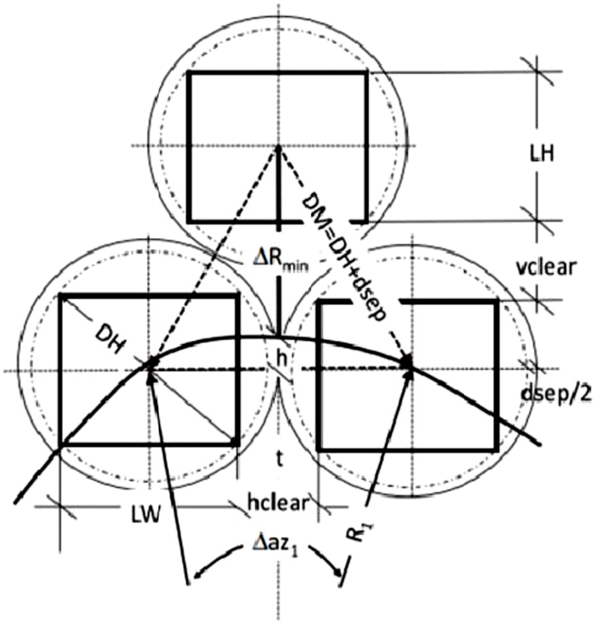

Figure 3.1 Radial spacing, azimuthal spacing and clearances [17].

The minimum radial distance is evaluated by,

$$\Delta \mathrm{R}_{\min} = DM \ \cos 30^{\circ} \tag{3}$$

The Azimuthal Spacing

Previously given by Collado and Guallar [17], the azimuthal increment is defined as the angular spacing between adjacent heliostats of the first ring,

$$\Delta \alpha \mathrm{z}_1 = 2\sin^{-1}\left(\frac{DM}{2R_1}\right) \cong \frac{DM}{R_1} \tag{4}$$

A zone is defined as a group of rings having a constant azimuthal spacing. R_1 is the radius of the first ring in the first zone. The radial staggered configuration implemented in the Literature implies that the azimuthal spacing between heliostats increases as we progress in the rows. This will lead to the redefining of the azimuthal spacing formulation when the azimuthal spacing is large enough to fit an additional heliostat, thus defining a new zone. For the first and second zones respectively, it is stated as follows,

$$\Delta\alpha z_2 = \Delta\alpha z_1 / 2 \cong \frac{DM}{R_2} \tag{5}$$

$$\Delta\alpha z_3 = \Delta\alpha z_1 / 4 \cong \frac{DM}{R_3} \tag{6}$$

Number of Heliostats

For the even and odd rows, separate mathematical formulations are used to find the number of heliostats.

For odd rows

$$Nhel = 2 \times round\left(\frac{\psi_{\max} - \Delta\alpha z \;/\; 2}{\Delta\alpha z}\right) + 1 \tag{7}$$

And for even rows,

$$Nhel = 2 \times round\left(\frac{\psi_{\max}}{\Delta\alpha z}\right) + 1 \tag{8}$$

where $Nhel$ is the number of heliostats, and $\psi_{\max}$ is the angular distance (in radians) from the north axis to the last heliostat.

Area of the Heliostat Field

The area of the heliostat field is defined as the circle of the radius from the tower center to the last row of the last zone of the field. It is calculated by the following equation,

$$A_l = \pi (R_{last} + 0.5DM)^2 \tag{9}$$

R_{last} is the radius of the last row in the last zone and A_l is the area covered by the heliostat field.

3.1.2 Solar Positioning Model

The solar positioning model is necessary to find the instantaneous optical efficiency of the heliostat field. The position with respect to the sun is calculated by the following,

$$\delta = \frac{23.45\pi}{180} \sin(2\pi \frac{284 + n_d}{365}) \tag{10}$$

$$\omega_{sunrise} = \cos^{-1}(\tan\phi \tan\delta) - \pi = -\omega_{sunset} \tag{11}$$

$$\alpha_s = \sin^{-1}(\cos\phi \cos\delta \cos\omega_s + \sin\phi \sin\delta) \tag{12}$$

$$\gamma_s = \mathrm{sgn}(\omega_s) \left| \cos^{-1} \frac{\sin\alpha \sin\phi - \sin\delta}{\cos\alpha \cos\phi} \right| \tag{13}$$

n_d is defined as the day of the year, ω_s is the hour angle, and ϕ is the latitude angle. The solar altitude and solar azimuth angle are α_s and γ_s respectively, and the solar declination angle is defined as δ [74].

3.1.3 Optical Efficiency of the Heliostat Field

The optical efficiency of the heliostat field is dependent, as stated in the introduction to this chapter, upon five parameters, namely, the cosine efficiency or the cosine of the angle between the incident sunray and the line normal to the surface of the heliostat ($\cos\omega$), atmospheric attenuation factor (f_{at}), shadowing and blocking factor (f_{sb}), intercept factor or the fraction of the reflected rays intercepted at the receiver (f_{itc}), and the actual mirror reflectivity (ρ) [17]. The equation for calculating the optical efficiency of the heliostat is,

$$\eta_{opt}(x,y,t) = \rho\cos\omega(x,y,t) f_{at}(x,y) f_{sb}(x,y,t) f_{itc}(x,y,t) \tag{14}$$

The following is a detailed explanation of each of the components involved in evaluating the optical performance.

Cosine Factor

The law of specular reflection is utilized to calculate the cosine factor. It is given by the dot product of the vector pointing towards the sun $\widehat{d}_{sun}$ and that normal to the heliostat $\widehat{d}_n$. The equation is,

$$\cos\omega = \widehat{d}_{sun} \cdot \widehat{d}_n \tag{15}$$

It could also be evaluated using the dot product of the vector pointing towards the receiver and the sun vector,

$$\cos\omega = \widehat{d}_{rec} \cdot \widehat{d}_n \tag{16}$$

The normal vector is found by the following equation,

$$\widehat{d}_n = \frac{\widehat{d}_{rec} + \widehat{d}_s}{|\widehat{d}_{rec} + \widehat{d}_s|} \tag{17}$$

where $\widehat{d}_s$ and $\widehat{d}_{rec}$ are the sun vector and the vector pointing towards the receiver respectively.

Atmospheric Attenuation Factor

The beam losses of the reflected ray from the heliostat to the receiver at the top of the tower is referred to as the atmospheric attenuation efficiency [75]. The equations for evaluating this factor is given by,

$$f_{at} = 0.99321 - 0.0001176 S_{rec} + 1.97 \times 10^{-8} S_{rec}^{2} \qquad if \quad S_{rec} < 1000m \tag{18}$$

$$f_{at} = \exp(-0.0001106 S_{rec}) \qquad if \quad S_{rec} \geq 1000m \tag{19}$$

The slant distance from the heliostat to the receiver is referred to as S_{rec} found in the equations.

Shading and Blocking Factor

The fraction of the area of the heliostat that is free of shading and blocking is referred to as the shading and blocking factor. It is calculated by Atif and Al-Sulaiman [11] based on the procedure found in earlier studies [17], [76]. A radial staggered configuration is adopted in this procedure and projections are taken from the edge points of the affecting heliostats onto the problem heliostat. the blocking heliostats are split into two categories, shoulder blocking and nose blocking, which are respectively, the two affecting heliostats in the next outer row and one affecting heliostat in the outer second row. Blocking heliostats were tested for shadowing as well. Shadowing heliostats, on the other hand, are not defined clearly in the procedure adopted, hence, for projection onto the affecting heliostats, nine surrounding heliostats were used. The shading and blocking configuration is illustrated in Figure 3.2.

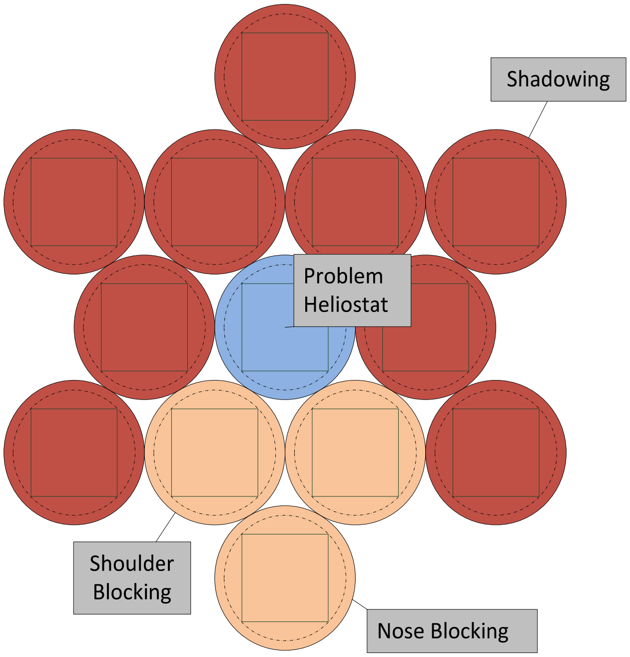

Figure 3.2 Projections onto the problem heliostat for the calculation of shading and blocking factor.

A computer code was written by Atif and Al-Sulaiman [11] and validated with the campo code [17]. The results computed from the former code, however, results in better accuracy since the total numbers of projections adopted in the campo code are 9 projections covering the worst cases, whereas, 15 projections were used in Atif and Al-

Sulaiman's code. Thus, slightly less results and better accuracy compared to the campo code were found. The validation of the code developed by Atif and Al-Sulaiman is illustrated in Table 3.1.

Table 3.1 Validation of the calculation of the shadowing and blocking factor

Sr. #	Case	Atif and Al-Sulaiman	Campo code
1	Day 345, solar hour 9, *dsep*=0	0.6246	0.676
2	Day 345, solar hour 9, *dsep*=3	0.7113	0.747
3	Day 81, solar hour 12, *dsep*=0	0.7936	0.794

Intercept Factor

The fraction of reflected rays intercepted by the receiver is referred to as the intercept factor. The intercept factor is also calculated by Atif and Al-Sulaiman [11] based on the HFLCAL model found in Literature [77]. The intercept factor is evaluated by the following equation,

$$f_{itc} = \frac{1}{2\pi\sigma_{tot}^2} \int_{x'}\int_{y'} \exp\left(-\frac{x'^2 + y'^2}{2\sigma_{tot}^2}\right) dy'.dx' \tag{20}$$

σ_{tot} is defined as the total standard deviation on the receiver plane, and calculated by the following,

$$\sigma_{tot} = \sqrt{S_{rec}^2(\sigma_{sun}^2 + \sigma_{bq}^2 + \sigma_{ast}^2 + \sigma_t^2)} \tag{21}$$

σ_{sun} is the sun shape error, σ_{bq} the beam quality error, σ_{ast} the astigmatic error, and σ_{track} the tracking error.

The beam quality error is calculated by,

$$\sigma_{bq}^2 = (2\sigma_s^2) \tag{22}$$

σ_s is defined as the mirror slope error caused by the imperfections of the mirror surface [75], [77], and is calculated by the following [16],

$$\sigma_s^2 = \frac{\sigma_h^2 + \sigma_v^2}{2} \tag{23}$$

The astigmatic effect is calculated by,

$$\sigma_{ast} = \frac{\sqrt{0.5(H_t^2 + W_s^2)}}{4S_{rec}} \tag{24}$$

$$H_t = d\left|\frac{S_{rec}}{f} - \cos\omega\right| \tag{25}$$

$$W_s = d\left|\frac{S_{rec}}{f}\cos\omega - 1\right| \tag{26}$$

$$d = \sqrt{LW \times LH} \tag{27}$$

W_s and H_t are defined as the image dimensions in the sagital and the tangential planes at distance S_{rec} from the mirror. f is defined as the focal distance of the heliostat and it is taken equal to S_{rec} in the study by Atif and Al-Sulaiman [11], and the sun shape error is also assumed equal to the value adopted by Collado [78]. The intercept factor is also validated against the data provided by Collado [78].

3.1.4 Optimization

The optimization of the heliostat on an annual basis has been studied by Atif and Al-Sulaiman [11]. Optimization is based on the differential evolution optimization algorithm [79]. The optimization has been selected by Atif and Al-Sulaiman due to its simplicity and fast convergence, and a Matlab program is developed to perform the desired task. The radial and azimuthal spacing are the optimizing parameters in their study.

Daily Averaged Annual Optimization

The daily averaged annually optimized optical efficiency of the heliostat field has been evaluated by Atif and Al-Sulaiman [11] based on earlier computational model. The equation implemented is as follows,

$$\eta_{daa} = \frac{\sum_{j=1}^{365}\left(\sum_{t=sunrise}^{t=sunset} \eta_{opt}\Delta t\right)}{\sum_{j=1}^{365} DH_j} \tag{28}$$

The daily average annually optimized heliostat field efficiency is denoted by η_{daa}.

Insolation Weighted Daily Averaged Annual Optimization

The equation for evaluating the insolation weighted daily average annually optimized efficiency is given by [80],

$$\eta_{iwaa} = \frac{\sum_{j=1}^{365} \left(\sum_{t=sunrise}^{t=sunset} I_b \eta_{opt} \Delta t \right)}{\sum_{j=1}^{365} \left(\sum_{t=sunrise}^{t=sunset} I_b \Delta t \right)} \tag{29}$$

The insolation weighted daily averaged annually optimized efficiency is denoted by η_{iwaa}

Monthly Averaged Annual Optimization

The monthly averaged annually optimized optical efficiency is calculated by the following equation,

$$\eta_{maa} = \frac{\sum_{k=1}^{12} \left(\sum_{t=sunrise}^{t=sunset} \eta_{opt} \Delta t \right)}{\sum_{k=1}^{12} DH_k} \tag{30}$$

The monthly averaged annually optimized optical efficiency is denoted by η_{maa}. The average day of each month of the year is considered in the calculation. Table 3.2 provides the average day of each month of the year.

Table 3.2 Recommended average days of month [74]

	Month	Average day of Month (Date)	Day of the year (n_d)
1	January	17	17
2	February	16	47
3	March	16	75
4	April	15	105
5	May	15	135
6	June	11	162
7	July	17	198
8	August	16	228
9	September	15	258
10	October	15	288
11	November	14	318
12	December	10	344

3.1.5 Central Receiver

For the central receiver modeling, the optical losses, heat radiation losses, and convection losses were evaluated. The following paragraphs represent a brief explanation of each.

Radiation Heat Losses

For calculating the radiation heat losses, the following equation is used [81]:

$$Q_{rad} = F_{view} A \varepsilon \sigma T_R^4 \tag{31}$$

The radiation shape factor is denoted by F_{view}, A is defined as the radiative area of the central receiver, emissivity is denoted by ε, σ is the Stefan-Boltzmann constant, and the receiver temperature is denoted by T_R.

Convective Heat Losses

The convective heat loss from the receiver is calculated by the following equation:

$$Q_{conv} = A h_{conv} (T_R - T_{amb}) \tag{32}$$

where h_{conv} is the convection heat transfer coefficient and is calculated by,

$$h_{conv} = 0.557 \times 10^{-6} (\frac{T_R - T_{amb}}{H_t})^{0.25} [\mathrm{kW/\,m^2 - K}] \tag{33}$$

where the total height of the solar tower and the ambient temperature are denoted by H_t and T_{amb} respectively.

Receiver Thermal Efficiency

The thermal efficiency of the central receiver is calculated by the following equations:

$$\eta_{th,R} = \frac{Q_{net}}{Q_{in}} \tag{34}$$

$$Q_u = Q_{net} = \alpha_R Q_{in} - (Q_{rad} + Q_{conv}) \tag{35}$$

$$Q_{in} = \eta_{opt} Q_{solar} \tag{36}$$

$$Q_{solar} = I A_h \tag{37}$$

The central receiver absorptivity is defined as α_R, the direct normal incident radiation is defined as I, and the total area of the heliostat is denoted by A_h. Q_u represents the useful energy gained at the receiver level, Q_{solar} and Q_{in} are the total incident radiation on the heliostats and the net energy intercepted at the receiver, respectively.

3.2 Supercritical CO_2 Brayton Cycle Modeling

The two supercritical CO_2 cycles used in this study are the regenerative and the recompression cycles. The mathematical modeling of these cycles is discussed in the following sections.

3.2.1 Regenerative sCO_2 Brayton Cycle

The regenerative Brayton cycle is illustrated in Figure 3.3. It is comprised of a compressor, a turbine, a heat source, a cooler, and a regenerator. The mathematical modeling of the cycle is as follows:

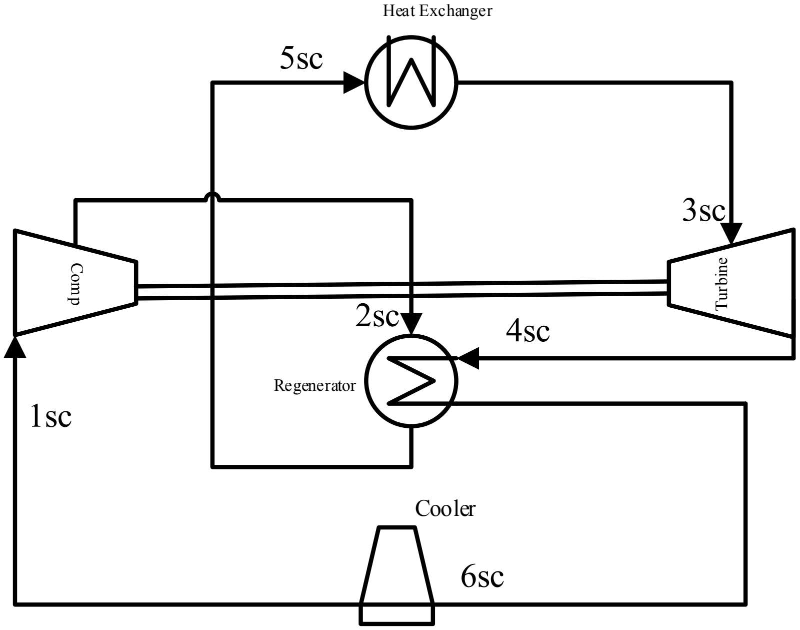

Figure 3.3 Regenerative supercritical carbon dioxide Brayton cycle.

The compressor work is evaluated by,

$$W_c = \dot{m}_{CO_2}(h_{2sc} - h_{1sc}) \tag{38}$$

The compressor isentropic efficiency is calculated by,

$$\eta_c = \frac{h_{2sc_s} - h_{1sc}}{h_{2sc} - h_{1sc}} \tag{39}$$

Effectiveness of the regenerator is found by,

$$\varepsilon_R = \frac{h_{5sc} - h_{2sc}}{h_{4sc} - h_{2sc}} \tag{40}$$

The work of the turbine is calculated by,

$$W_T = \dot{m}_{CO_2}(h_{3sc} - h_{4sc}) \tag{41}$$

And its isentropic efficiency,

$$\eta_T = \frac{h_{3sc} - h_{4sc}}{h_{3sc} - h_{4sc_s}} \tag{42}$$

Energy balance on the regenerator results in the following equation:

$$h_{5sc} - h_{2sc} = h_{4sc} - h_{6sc} \tag{43}$$

The lost energy at the cooler stage is calculated by,

$$Q_{out} = \dot{m}_{CO_2}(h_{6sc} - h_{1sc}) \tag{44}$$

Finally, the net work of the cycle is given by,

$$W_{net} = W_T - W_C \tag{45}$$

The entropy generated in each of the components of the regenerative cycle is calculated as follows,

Starting with the first compressor

$$\dot{m}_{CO_2} s_{1sc} - \dot{m}_{CO_2} s_{2sc} + \dot{S}_{gen_{comp1}} = 0 \tag{46}$$

The regenerator,

$$\dot{m}_{CO_2} s_{2sc} - \dot{m}_{CO_2} s_{5sc} + \dot{m}_{CO_2} s_{4sc} - \dot{m}_{CO_2} s_{6sc} + \dot{S}_{gen_{reg}} = 0 \tag{47}$$

The turbine,

$$\dot{m}_{CO_2} s_{3sc} - \dot{m}_{CO_2} s_{4sc} + \dot{S}_{gen_{turb}} = 0 \tag{48}$$

3.2.2 Recompression sCO$_2$ Brayton Cycle

The recompression Brayton cycle is comprised of two compressors, two regenerators (high and low temperature regenerators), a cooler, a turbine, and a heat source. After the low temperature regenerator stage, the flow is split in two, part flowing into the main compressor, and the remaining into the cooler. The system in this case rejects less heat through the cooler causing an increase in the thermal efficiency. It is better illustrated in Figure 3.4.

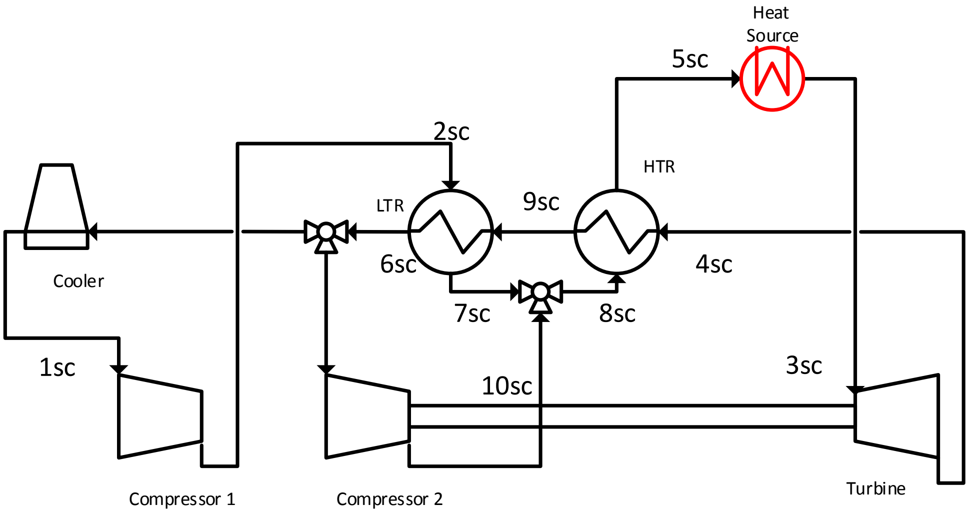

Figure 3.4 Recompression supercritical carbon dioxide Brayton cycle.

The mathematical modeling of the recompression model is discussed next. The work of the first compressor is calculated by,

$$W_{c1} = x\dot{m}_{CO_2}(h_{2sc} - h_{1sc}) \tag{49}$$

where x defined as the mass flow rate fraction flowing into the first compressor, the isentropic efficiency of the first compressor can also be calculated by,

$$\eta_{c1} = \frac{h_{2sc_s} - h_{1sc}}{h_{2sc} - h_{1sc}} \tag{50}$$

The second compressor work is found by,

$$W_{c2} = (1-x)\dot{m}_{CO_2}(h_{10sc} - h_{6sc}) \tag{51}$$

And its isentropic efficiency,

$$\eta_{c2} = \frac{h_{10sc_s} - h_{6sc}}{h_{10sc} - h_{6sc}} \tag{52}$$

The effectiveness of the high temperature and low temperature regenerators can also be calculated by the following equations respectively,

$$\varepsilon_{HTR} = \frac{h_{5sc} - h_{8sc}}{h_{4sc} - h_{8sc}} \tag{53}$$

$$\varepsilon_{LTR} = \frac{h_{7sc} - h_{2sc}}{h_{9sc} - h_{2sc}} \tag{54}$$

where the high temperature regenerator effectiveness is denoted by ε_{HTR} , and that of the low temperature regenerator is denoted by ε_{LTR} .

And the turbine work by,

$$W_T = \dot{m}_{CO_2}(h_{3sc} - h_{4sc}) \tag{55}$$

And its isentropic efficiency is evaluated by,

$$\eta_T = \frac{h_{3sc} - h_{4sc}}{h_{3sc} - h_{4sc_s}} \tag{56}$$

Energy balance on the high and low temperature regenerators result in the following equations respectively:

$$h_{4sc} - h_{9sc} = h_{5sc} - h_{8sc} \tag{57}$$

$$x\,(h_{7sc} - h_{2sc}) = h_{9sc} - h_{6sc} \tag{58}$$

The output work from the cycle is calculated by subtracting the work of the two compressors from the work of the turbine,

$$W_{net} = W_T - W_{C1} - W_{C2} \tag{59}$$

The entropy generated in each of the components of the recompression cycle is calculated as follows:

The first compressor,

$$x\dot{m}_{CO_2}\left(s_{1sc} - s_{2sc}\right) + \dot{S}_{gen_{comp1}} = 0 \tag{60}$$

Second compressor,

$$\left(1 - x\right)\dot{m}_{CO_2}\left(s_{6sc} - s_{10sc}\right) + \dot{S}_{gen_{comp2}} = 0 \tag{61}$$

Low temperature recuperator,

$$x\dot{m}_{CO_2}\left(s_{2sc} - s_{7sc}\right) + \dot{m}_{CO_2}\left(s_{9sc} - s_{6sc}\right) + \dot{S}_{gen_{LTR}} = 0 \tag{62}$$

High temperature recuperator,

$$\dot{m}_{CO_2}\left(s_{8sc} - s_{5sc}\right) + \dot{m}_{CO_2}\left(s_{4sc} - s_{9sc}\right) + \dot{S}_{gen_{HTR}} = 0 \tag{63}$$

The turbine,

$$\dot{m}_{CO_2}\left(s_{3sc} - s_{4sc}\right) + \dot{S}_{gen_{turb}} = 0 \tag{64}$$

3.2.3 Thermal Efficiency of the sCO$_2$ Brayton Cycles

For both systems, the thermal efficiency for the cycle is defined as,

$$\eta_{th_{power}} = \frac{W_{net}}{Q_{in_{CO_2}}} \tag{65}$$

where W_{net} is the net work obtained from the cycle, and $Q_{in_{CO_2}}$ is the heat added to the supercritical carbon dioxide cycle.

3.2.4 Validation of sCO$_2$ Brayton Cycles Modeling

The mathematical modeling of sCO$_2$ cycles is done by EES [82] (Engineering Equation Solver). In order to validate the model, the results from the recompression cycle has been compared with previously published results in the literature, which is presented in figure 2 of the reference [83]. A T-s (pressure-entropy) diagram is plotted for both results in the graph of Figure 3.5. It is concluded from the graph that the results from EES are in good agreement with the results found in Literature.

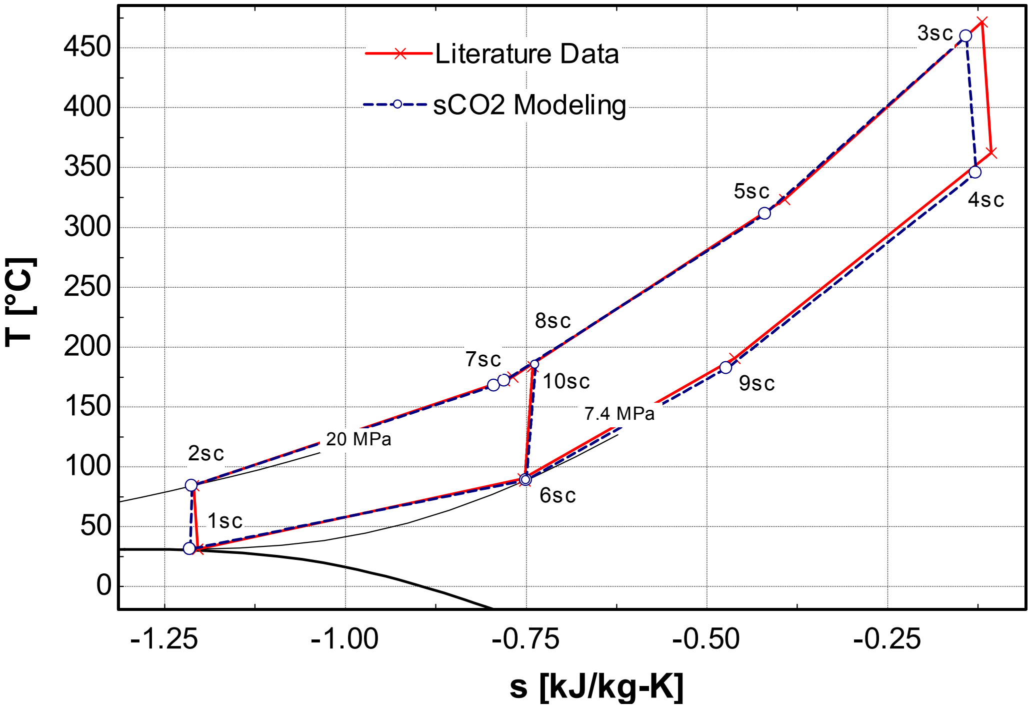

Figure 3.5 T-s diagram for validation of EES code with reference [83].

3.3 Multiple Effect Evaporation – Thermal Vapor Compression

The multiple effect evaporation with thermal vapor compression (MEE-TVC) is adopted in the cogeneration system under study. Similar to the MEE desalination system, MEE-TVC consists of horizontal falling film evaporators or effects, an end condenser, flashing boxes, and feed preheaters. The only difference is that unlike MEE, MEE-TVC has one extra component, the steam jet ejector which acts as a thermal compressor.

3.3.1 Function of the MEE-TVC

The multiple effect evaporation with thermal vapor compression desalination system uses motive steam $\dot{m}_s$ at relatively high pressure to entrain part of the vapor $\dot{m}_r$ formed in the last effect. The entrained vapor is then added to the motive steam and enters the first effect where its latent heat of condensation is utilized in heating the feed seawater entering the effect from a temperature of T_{f1} to a temperature of T_1 defined as the boiling temperature, as well as, evaporating part of the feed by boiling. The evaporated feed is denoted by $\dot{m}_{d_1}$ for the first effect. The condensate forming the motive and entrained vapor is split again where the motive steam flows back to the source and the entrained vapor flows into the first flashing box. Due to the pressure drop in the flashing box, a small fraction of steam is flashed off, and along with the vapor distillate from the first effect, it passes through the first preheater and to the second effect where the same process occurs again until we reach the last effect. The brine heated in the first effect is directed into the second effect where a vapor fraction is flashed off from it and added to the distillate vapor formed in that effect due to the pressure drop and that of the second effect is directed into the third, and so on until reaching the last effect. The distillate from the last effect is split into two parts, entrained vapor to redo the process discussed earlier, and the remainder denoted by $\dot{m}_{d_f}$ flows into the end condenser where it condenses to be added to the distillate produced from the rest of the effects and its latent heat is utilized to heat the cooling seawater temperature from T_c to T_{f_n}, corresponding to the seawater temperature before and after passing through the condenser respectively. The flow rate amount of cooling seawater temperature is denoted by $\dot{m}_{sw}$, which in turn, after passing through the down condenser, is split into two parts, one being fed to the system denoted by $\dot{m}_{f_{tot}}$ and the other being considered as excess and rejected back. The MEE-TVC is illustrated in Figure 3.6.

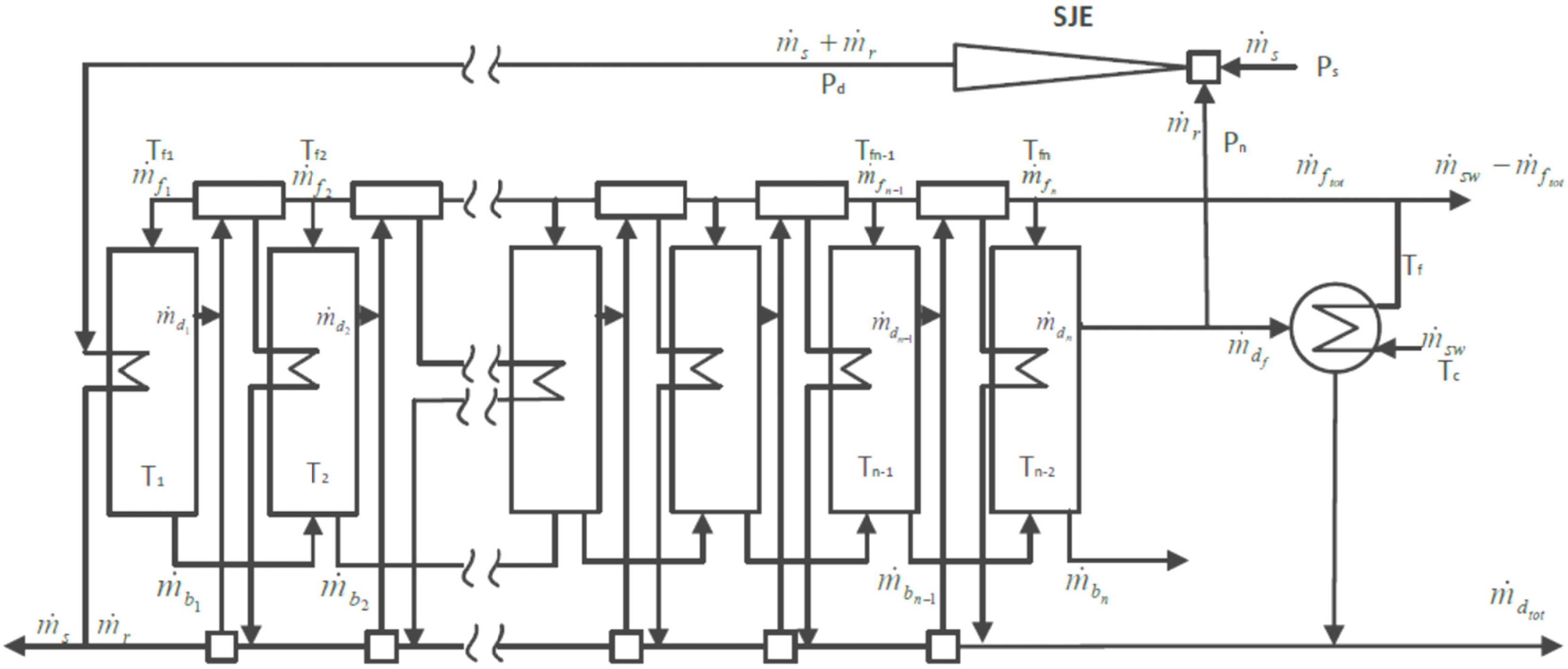

Figure 3.6 Multiple effect evaporation- thermal vapor compression

3.3.2 MEE-TVC Mathematical Modeling

A mathematical model for the study of the MEE-TVC desalination system has been developed based on an earlier model by Bin Amer [31]. The model is developed through the application of mass and energy conservation laws on the different components of the system such as the effects, feed preheaters, end condenser, and steam jet ejector. Simplifying assumptions has been made in the model of Bin Amer [31], the assumptions are summarized by the following,

- Negligible heat is lost into the surrounding.
- Equal temperature difference across feed preheaters.
- Salt free distillate resulting from the effects.
- Negligible variation in specific heat with temperature and salinity.
- Equal temperature difference across the effects.

Having the simplifying assumptions stated, and utilizing the equal temperature difference across the effects assumption, if the brine temperature in effect i is T_i , then the brine temperature in effect T_{i+1} can be calculated by the following equation:

$$T_{i+1} = T_i - \Delta T \qquad i = 1, 2, ...n \tag{66}$$

The vapor generated in effect i has a lower temperature than the brine temperature. The vapor temperature is denoted by T_{v_i} and it is calculated by subtracting the boiling point elevation and the non-equilibrium allowance from the boiling temperature.

$$T_{vi} = T_i - (BPE + NEA) \qquad i = 1, 2, ...n \tag{67}$$

where the boiling point elevation and non-equilibrium allowance are denoted by BPE and NEA respectively.

The difference in temperature between the effects is calculated by the following equation:

$$\Delta T = (T_1 - T_n) / (n - 1) \tag{68}$$

T_1 and T_n are the brine temperatures in the first and last effect respectively, and n is the number of effects.

The feed seawater flow rate denoted by F is distributed equally over the effects; it is calculated by the following equation:

$$\dot{m}_{f_i} = \dot{m}_{f_{tot}} / n \tag{69}$$

As discussed earlier, the brine leaving the first effect enters the second, and that of the second effect enters the third until reaching the last effect where the brine rejection takes place. A cumulative trend then should be adopted and the formulas for calculating the brine flow rate in the 1st, ith, and last effect are as follows:

$$\dot{m}_{b_1} = \dot{m}_{f_1} - \dot{m}_{d_1} \tag{70}$$

$$\dot{m}_{b_{i+1}} = \sum_{k=1}^{k=i+1} (\dot{m}_{f_k} - \dot{m}_{d_k}) \tag{71}$$

$$\dot{m}_{b_n} = \sum_{k=1}^{k=n} (\dot{m}_{f_k} - \dot{m}_{d_k}) \tag{72}$$

In the first effect, the motive steam and entrained vapor latent heat of vaporization is utilized to heat the feed seawater to a temperature of T_1 and evaporate a portion denoted by $\dot{m}_{d_1}$, which is the distillate formed in the first effect. The equation is thus defined by,

$$\dot{m}_{d_1} = \frac{\left[\left(\dot{m}_s + \dot{m}_r\right)\left(h_d - h_{fd}\right)\right]}{L_1} - \dot{m}_{f_1} C \left(\frac{T_1 - T_{f1}}{L_1}\right) \tag{73}$$

where L_1 denotes the latent heat of vaporization at temperature T_{v1}, h_d and h_{fd} are the enthalpy of discharged steam and the saturated liquid enthalpy of discharged steam after condensation respectively, and C is the specific heat.

When the condensed vapor $\dot{m}_r$ enters the first flashing box, a portion of steam equal to $\dot{m}_r y$ will be flashed off. The flashed off vapor is calculated by,

$$y_i = \frac{C \Delta T}{L_i} \qquad i = 1, 2, \ldots n - 1 \tag{74}$$

The vapor flashed in the first flashing box is added to the distillate formed in the first effect, both flow into the first preheater to heat the feed seawater from temperature of T_{f2} to a temperature of T_{f1}. This process results in the condensation of a fraction of the vapor, and the rest of the vapor will be utilized in the second effect, thus, the equation for calculating the distillate formed in the second effect is given by the following:

$$\dot{m}_{d_2} = \left(\dot{m}_{d_1} + \dot{m}_r y_1 - \dot{m}_{f_1} y_1\right)\frac{L_1}{L_2} - \dot{m}_{f_2} C \frac{\left(T_2 - T_{f2}\right)}{L_2} + \dot{m}_{b_1} \frac{C \Delta \mathrm{T}}{L_2} \tag{75}$$

Similarly, the distillate formed in the 3rd, ith, and last effects are calculated by the following equations:

$$\dot{m}_{d_3} = \left(\dot{m}_{d_2} + \left(\dot{m}_r + \dot{m}_{d_1}\right) y_2 - 2\dot{m}_{f_2} y_2\right)\frac{L_2}{L_3} - \dot{m}_{f_3} C \frac{\left(T_3 - T_{f3}\right)}{L_3} + \dot{m}_{b_2}\frac{C\Delta \mathrm{T}}{L_3} \tag{76}$$

$$\dot{m}_{d_i} = \left(\dot{m}_{d_{i-1}} + \left(\sum_{k=1}^{i-2}\dot{m}_{d_k} + \dot{m}_r\right) y_{i-1} - \left(i-1\right)\dot{m}_{f_{i-1}} y_{i-1}\right)\frac{L_{i-1}}{L_i} - \dot{m}_{f_i} C \frac{\left(T_i - T_{f_i}\right)}{L_i} + \dot{m}_{b_{i-1}}\frac{C\Delta \mathrm{T}}{L_i} \tag{77}$$

$$\dot{m}_{d_n} = \left(\dot{m}_{d_{n-1}} + \left(\sum_{k=1}^{n-2}\dot{m}_{d_k} + \dot{m}_r\right) y_{n-1} - \left(n-1\right)\dot{m}_{f_{n-1}} y_{n-1}\right)\frac{L_{n-1}}{L_n} - \dot{m}_{f_n} C \frac{\left(T_n - T_f\right)}{L_n} + \dot{m}_{b_{n-1}}\frac{C\Delta \mathrm{T}}{L_n} \tag{78}$$

The distillate formed in the last effect is, as stated earlier, split into two parts, one entrained in the steam jet ejector and the other directed into the down condenser, the equation then is given by,

$$\dot{m}_{d_n} = \dot{m}_r + \dot{m}_{d_f} \tag{79}$$

The total distillate output is the sum of the distillate formed by all the effects, it is given by,

$$\dot{m}_{d_{tot}} = \sum_{i=1}^{n}\dot{m}_{d_i} \tag{80}$$

It has been stated in the assumptions earlier that the distillate is free of salt, so in order to find the salinity of brine exiting each effect, the salt-mass conservation law is applied. The brine salinity for the 1st, ith, and last effect is calculated by the following equations:

$$X_{b_1} = \frac{\dot{m}_{f_1}}{(\dot{m}_{f_1} - \dot{m}_{d_1})} X_f \tag{81}$$

$$X_{b_{i+1}} = \frac{\dot{m}_{f_{i+1}}}{\sum_{k=1}^{i+1}(\dot{m}_{f_k} - \dot{\mathrm{m}}_{d_k})} X_f + \frac{\sum_{k=1}^{i}(\dot{m}_{f_k} - \dot{m}_{d_k})}{\sum_{k=1}^{i+1}(\dot{m}_{f_k} - \dot{m}_{d_k})} X_{b_i} \tag{82}$$

$$X_{b_n} = \frac{\dot{m}_{f_n}}{\sum_{k=1}^{n}(\dot{m}_{f_k} - \dot{\mathrm{m}}_{d_k})} X_f + \frac{\sum_{k=1}^{n-1}(\dot{m}_{f_k} - \dot{m}_{d_k})}{\sum_{k=1}^{n}(\dot{m}_{f_k} - \dot{m}_{d_k})} X_{b_{n-1}} \tag{83}$$

The global salt-mass balance if we consider a control volume which includes the system as a whole is given by,

$$\dot{m}_{f_{tot}} X_f = \dot{m}_{b_n} X_b + \dot{m}_{d_{tot}} X_d \tag{84}$$

The assumption of salt-free distillate renders $X_d = 0$. The mass balance over the whole control volume gives,

$$\dot{m}_{f_{tot}} = \dot{m}_{b_n} + \dot{m}_{d_{tot}} \tag{85}$$

This states that the total produced distillate and the total rejected brine equals the total feed seawater supplied to the system. Equations (84) and (85) result in the equation for the ratio of total feed to the total distillate produced as a function of brine and feed salinity. The equation is simply,

$$\frac{\dot{m}_{f_{tot}}}{\dot{m}_{d_{tot}}} = \frac{X_b}{X_b - X_f} \tag{86}$$

The general equation for calculating the heat transfer area from thermal load is given by,

$$Q = U_e A_e \Delta \mathrm{T}_e \tag{87}$$

where $\Delta \mathrm{T}_e$ is defined as the temperature difference across the heat transfer surface, that is, the temperature of the vapor and that of the brine. The heat transfer area for the 1st, 2nd, i$^{\mathrm{th}}$, and the last effect can be calculated by the following:

$$A_{e1} = \frac{\left(\dot{m}_s + \dot{m}_r\right)\left(h_d - h_{fd}\right)}{U_{e1}\left(T_d - T_1\right)} \tag{88}$$

$$A_{e_2} = \frac{\left(\dot{m}_{d_1} + \dot{m}_r y_1 - \dot{m}_{f_1} y_1\right) L_1}{U_{e_2}\left(T_{v_1} - T_2\right)} \tag{89}$$

$$A_{e_{i+1}} = \frac{\left(\dot{m}_{d_i} + (\sum_{k=1}^{i-2} \dot{m}_{d_k} + \dot{m}_r) y_i - i.\dot{m}_{f_i} y_i\right) L_i}{U_{e_{i+1}} (T_{v_i} - T_{i+1})} \tag{90}$$

$$A_{e_n} = \frac{\left(\dot{m}_{d_{n-1}} + (\sum_{k=1}^{n-2} \dot{m}_{d_k} + \dot{m}_r) y_{n-1} - (n-1)\dot{m}_{f_n} y_{n-1}\right) L_{n-1}}{U_{e_n} (T_{v_{n-1}} - T_n)} \tag{91}$$

where U_e is the overall heat transfer coefficient and is calculated by the following equation [6]:

$$U_{e_i} = \frac{\left(1939.4 + 1.40562 T_i - 0.0207525\left(T_i\right)^2 + 0.0023186\left(T_i\right)^3\right)}{1000} \tag{92}$$

Applying the energy balance on the down condenser, the equation for calculating the cooling seawater flow rate is found by,

$$\dot{m}_{sw} = \frac{\dot{m}_{d_f} L_n}{C\left(T_f - T_c\right)} \tag{93}$$

Similar to the area of the effects, the heat transfer area of the down condenser is calculated using the thermal load. The condenser heat transfer area is given by the following equation:

$$A_c = \frac{\dot{m}_{d_f} L_n}{U_c (LMTD)_c} \tag{94}$$

where the logarithmic mean temperature difference is denoted by $(LMTD)_c$, and is given by,

$$(LMTD)_c = \frac{\left(T_{v_n} - T_f\right) - \left(T_{v_n} - T_c\right)}{\ln \dfrac{\left(T_{v_n} - T_f\right)}{\left(T_{v_n} - T_c\right)}} \tag{95}$$

And U_c is the overall heat transfer coefficient of the down condenser and it is calculated by,

$$U_c = 1.7194 + 3.2063 \cdot 10^{-2} T_{v_n} - 1.5971 \cdot 10^{-5} (T_{v_n})^2 + 1.9918 \cdot 10^{7} (T_{v_n})^3 \tag{96}$$

In a similar fashion, the heat transfer area for the feed preheaters can be calculated by the following equation:

$$A_{f_i} = \frac{i \cdot \dot{m}_{f_i} C \Delta T_f}{U_f (T_{f_i} - T_{f_{i+1}})} \ln \frac{(T_{v_i} - T_{f_{i+1}})}{(T_{v_i} - T_{f_i})} \qquad i = 1, 2, \ldots n-1 \tag{97}$$

As for the mathematical modeling related to the steam jet ejector, it should be noted that simplifying assumptions are made, these assumptions are [84],

- Processes involved within the steam jet ejector are adiabatic.
- Motive steam and entrained vapor are saturated.

Applying the energy conservation law on the steam jet ejector results in the following equation:

$$\dot{m}_s h_s + \dot{m}_r h_{g_n} = (\dot{m}_s + \dot{m}_r) h_d \tag{98}$$

h_{g_n} is the saturated vapor enthalpy of the entrained vapor extracted from the last effect.

Thus, the equation for evaluating the discharges steam enthalpy is given by,

$$h_d = \left(\frac{\left(\frac{\dot{m}_s}{\dot{m}_r} \right) h_s + h_{g_n}}{1 + \left(\frac{\dot{m}_s}{\dot{m}_r} \right)} \right) \tag{99}$$

The entrainment ratio defined as the ratio of motive steam to entrained vapor is the most important part in the modeling of the MEE-TVC desalination system. The entrainment ratio is a function of the compression and expansion ratio expressed as the ratio of discharged pressure to entrained vapor pressure and that of the motive steam pressure to entrained vapor pressure respectively [6], [84], [85]. Compression and expansion ratio are denoted by CR and ER respectively, and given as,

$$CR = \frac{P_d}{P_n} \tag{100}$$

$$ER = \frac{P_s}{P_n} \tag{101}$$

Two simple methods found in Literature are used to evaluate the entrainment ratio, power's graphical method [86], and Dessouki and Ettouneys' semi-empirical model [6]. Power's graphical method is illustrated in Figure 3.7 where the entrainment ratio is extracted from the graph by knowing the compression ratio and the expansion ratio.

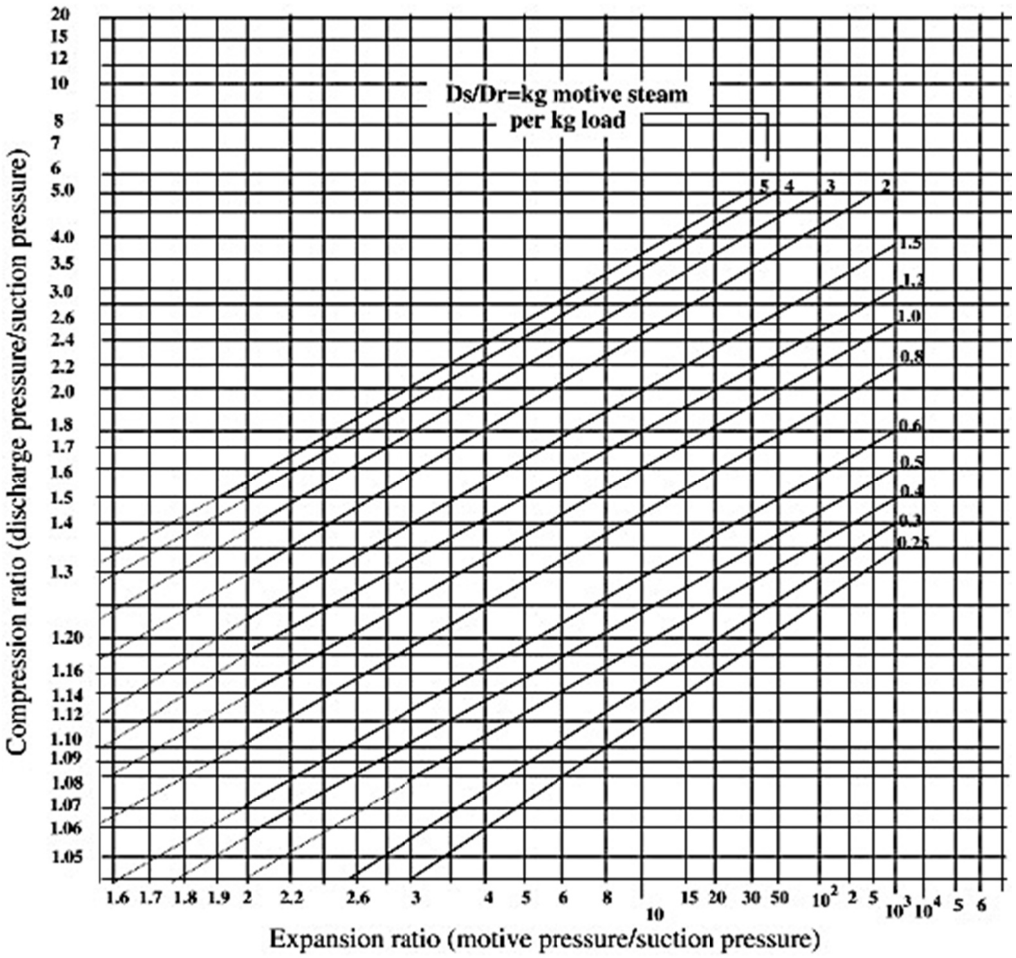

Figure 3.7 Power's graphical method (entrainment ratio function of CR and ER) [77]

Although Power's graphical method is an effective tool for evaluating the entrainment ratio, it would be difficult to utilize it in parametric studies, thus, the semi-empirical model developed by Dessouki and Ettouney will be utilized. The model is validated with Power's graphical data over the range of $3500kPa \geq P_s \geq 100kPa$ [6]. The entrainment ratio is given by,

$$\left(\frac{\dot{m}_s}{\dot{m}_r}\right) = 0.297\frac{\left(P_d\right)^{1.19}}{\left(P_n\right)^{1.04}}\left(ER\right)^{0.015}\left(\frac{PCF}{TCF}\right) \tag{102}$$

where PCF and TCF are the pressure and temperature correction factors respectively, and are given by,

$$PCF = 3\cdot 10^{-7}(P_s)^2 - 0.0009(P_s) + 1.6101 \tag{103}$$

$$TCF = 2\cdot 10^{-8}(T_{v_n})^2 - 0.0006(T_{v_n}) + 1.0047 \tag{104}$$

3.3.3 Performance of the MEE-TVC Desalination System

Parameters for the evaluation of the performance of a thermal desalination system is its gain output ratio defined as the ratio of the latent heat of the distillate produced to the heat input into the system, and the performance ratio defined as the ratio of distillate to motive steam, given by the following equations:

$$GOR = \frac{\dot{m}_{d_{tot}} h_{fg}}{Q_{des}} \tag{105}$$

$$PR = \frac{\dot{m}_{d_{tot}}}{\dot{m}_s} \tag{106}$$

Another parameter for evaluating a system's performance is its specific heat consumption given by the following equation:

$$Q_d = \frac{\dot{m}_s L_s}{\dot{m}_{d_{tot}}} \tag{107}$$

where L_s denotes the latent heat of motive steam.

In addition to the gain ratio and the specific heat consumption, the specific heat transfer area is an additional parameter accounted for in the study of the cost of the desalination system, it is given by,

$$A_{t_s} = \frac{1}{D}\left(\sum_{i=1}^{n} A_{e_i} + \sum_{i=1}^{n-1} A_{f_i} + A_c \right) \tag{108}$$

Equations (105)-(108) were written on EES [82] (Engineering Equation Solver) to utilize for simulation and parametric studies performed on the cogeneration system to be later introduced in this chapter.

3.3.4 Results Confirmation

The validation of the EES code is performed by comparing the results derived with previously found results in Literature. The results are thus compared with the results found in Bin Amer's study [31] and is shown in Table 3.3 below where the gain ratio calculated is compared to that found in literature for the same operating and design conditions.

Table 3.3 MEE-TVC gain ratio comparison with literature data [31]

n	Temperature			Ejector Design	PR	
	T[1]	T[n]	ΔT	CR	EES code	Literature [31]
4	55.8	46.7	3.03	1.81	7.862	8.52
5	55.8	46.1	2.42	1.81	9.72	9.87
6	55.8	44.3	2.3	1.98	11.3	11.4
7	56.4	42.8	2.26	2.2	12.72	12.28
8	58.8	42.8	2.28	2.46	13.56	13.08
9	60.9	42.8	2.26	2.7	14.43	14.14
10	63.3	42.8	2.27	3.01	15.09	15.23
11	65.4	42.8	2.26	3.31	15.77	16.52
12	67.8	42.8	2.27	3.68	16.31	17.88

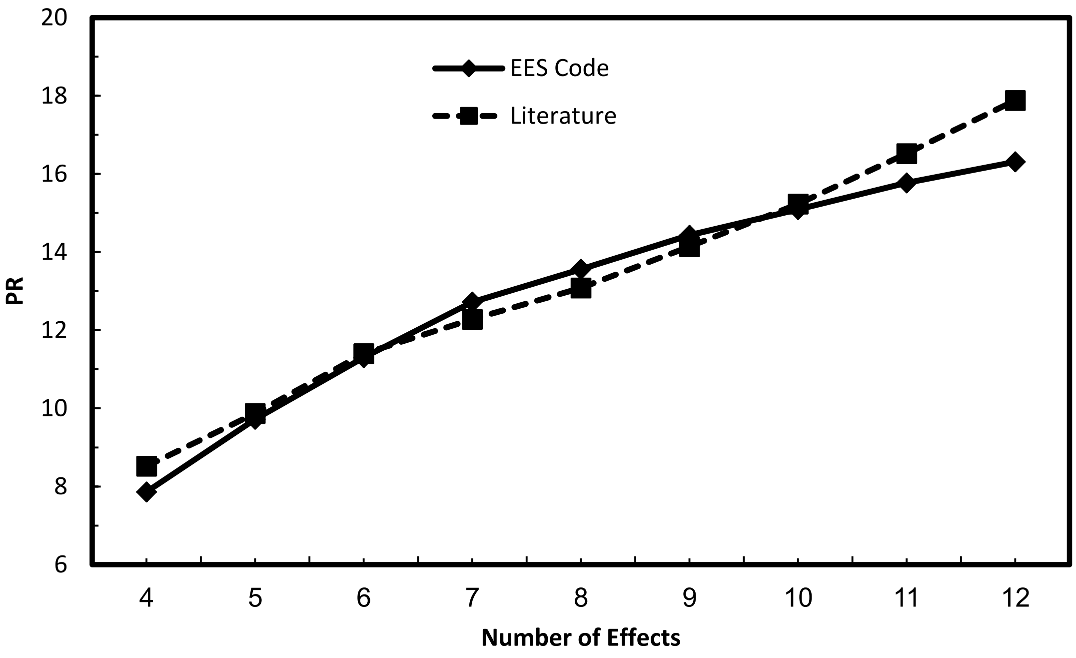

Figure 3.8 MEE-TVC gain ratio comparison with Literaure data [31]

The slight difference between the results generated and those found in Literature can be explained by the difference in salt-mass balance equations for each effect. While the MEE-TVC desalination system operates in a cross-flow mode, meaning that the brine resulting from each effect is entered into the next effect for brine flashing. Bin Amer's

[31] salt-mass balance equation is as follows $X_{b_{i+1}} = \dfrac{\dot{m}_{f_{i+1}}}{\sum_{k=1}^{i+1}(\dot{m}_{f_k} - \dot{m}_{d_k})} X_f$ compared to equation (82) in this study. We can see that the equation found in Literature does not account for the cross-flow mode; rather, it states that the stream involved in the salt-mass balance entering the effect is that of the feed only without the brine from the previous effect which is only true for the first effect.

3.3.5 Entropy Generation in MEE-TVC Desalination

In this section, entropy generation equations for each component in the MEE-TVC desalination system are addressed.

Steam Jet Ejector

$$\dot{m}_s s_s + \dot{m}_r s_{d_{gn}} - (\dot{m}_s + \dot{m}_r) s_d + \dot{S}_{gen_{SJE}} = 0 \tag{109}$$

where s_s is the specific entropy of motive steam, $s_{d_{gn}}$ is the specific entropy of vapor formed in the last effect, and s_d is that of the discharged steam. The entropy generated in the steam jet ejector is denoted by $\dot{S}_{gen_{SJE}}$.

Effects

The entropy generated in the first effect is calculated by the following equation:

$$(\dot{m}_s + \dot{m}_r)(s_d - s_{d_f}) + \dot{m}_{f_1} s_{f_1} - \dot{m}_{d_1} s_{d_{g1}} - \dot{m}_{b_1} s_{b_1} + \dot{S}_{gen_{eff\,1}} = 0 \tag{110}$$

s_{d_f} is the specific entropy of the condensed discharged stream leaving the first effect, s_{f_1} is the specific entropy of the feed stream entering the first effect, $s_{d_{g1}}$ is the specific entropy of the vapor distillate leaving the first effect, and s_{b_1} is that of the brine leaving the first effect. The entropy generated in the first effect is denoted by $\dot{S}_{gen_{eff\,1}}$.

Adding the effect of the brine entering from the first effect, entropy generation in the second effect can be calculated by,

$$\left(\dot{m}_{d_1}+\dot{m}_r y_1-\dot{m}_{f_1} y_1\right)\left(s_{d_{g1}}-s_{d_{f1}}\right)+\dot{m}_{f_2}s_{f_2}-\dot{m}_{d_2}s_{d_{g2}}+\dot{m}_{b_1}s_{b_1}-\dot{m}_{b_2}s_{b_2}+\dot{S}_{gen_{eff\,2}}=0 \qquad (111)$$

Similarly, the entropy generated in the rest of the effects is given by the following equation:

$for \quad i=2,n-1$

$$\left(\dot{m}_{d_i}+\left(\sum_{k=1}^{i-1}\dot{m}_{d_k}+\dot{m}_r\right)y_i-\dot{m}_{f_{i+1}}y_i\right)\left(s_{d_{gi}}-s_{d_{fi}}\right)+\dot{m}_{f_{i+1}}s_{f_{i+1}}-\dot{m}_{d_{i+1}}s_{d_{g(i+1)}}+\dot{m}_{b_i}s_{b_i}-\dot{m}_{b_{i+1}}s_{b_{i+1}}+\dot{S}_{gen_{eff\,(i+1)}}=0 \qquad (112)$$

where $s_{d_{gi}}$ and $s_{d_{fi}}$ are the specific entropies of the distillate from the ith effect in vapor and saturated liquid forms respectively.

Preheaters

The entropy generated in the first preheater is calculated as follows:

$$\dot{m}_{f_1}y_1\left(s_{d_{g1}}-s_{d_{f1}}\right)+\dot{m}_{f_2}s_{f_2}-\dot{m}_{f_1}s_{f_1}+\dot{S}_{gen_{ph1}}=0 \qquad (113)$$

where s_{f_1} and s_{f_2} are the specific entropies of the seawater feed stream entering the first and second effects respectively.

The second preheater,

$$2\dot{m}_{f_2}y_2\left(s_{d_{g2}}-s_{d_{f2}}\right)+2\dot{m}_{f_3}s_{f_3}-2\dot{m}_{f_2}s_{f_2}+\dot{S}_{gen_{ph2}}=0 \tag{114}$$

where s_{f_3} is the specific entropy of the seawater feed stream entering the third effect.

Similarly, the entropy generation in the rest of the feed preheaters is given by,

$for\ \ i=2,n-2$

$$\left(i+1\right)\dot{m}_{f_{i+1}}y_{i+1}\left(s_{d_{gi}}-s_{d_{fi}}\right)+\left(i+1\right)\dot{m}_{f_{i+2}}s_{f_{i+2}}-\left(i+1\right)\dot{m}_{f_{i+1}}s_{f_{i+1}}+\dot{S}_{gen_{ph(i+1)}}=0 \tag{115}$$

where s_{f_i} represents the specific entropy of the seawater feed stream entering the ith effect.

Flashboxes

Entropy generation in the first flashbox is given by the following equation:

$$\dot{m}_r s_{d_f}-\dot{m}_r y_1 s_{d_{g1}}-\left(\dot{m}_r-\dot{m}_r y_1\right)s_{d_{f1}}+\dot{S}_{gen_{fb1}}=0 \tag{116}$$

The second flashbox,

$$\left(\dot{m}_{d_1}+\dot{m}_r\right)s_{d_{f1}}-\left(\dot{m}_{d_1}+\dot{m}_r\right)y_2 s_{d_{g2}}-\left(\dot{m}_{d_1}+\dot{m}_r\right)\left(1-y_2\right)s_{d_{f2}}+\dot{S}_{gen_{fb2}}=0 \tag{117}$$

Similarly, entropy generation in the rest of the flashboxes is calculated by the following:

$for\ \ i=3,n-1$

$$\left(\sum_{k=1}^{i-1}\dot{m}_{d_k}+\dot{m}_r\right)s_{d_{f(i-1)}}-\left(\sum_{k=1}^{i-1}\dot{m}_{d_k}+\dot{m}_r\right)y_i s_{d_{gi}}-\left(\sum_{k=1}^{i-1}\dot{m}_{d_k}+\dot{m}_r\right)(1-y_i)s_{d_{fi}}+\dot{S}_{gen_{fb(i)}}=0 \quad (118)$$

Down Condenser

The equation for entropy generation in the down condenser is given by,

$$\dot{m}_f\left(s_{d_{gn}}-s_{d_{fn}}\right)+\dot{m}_{sw}\left(s_{sw_1}-s_{f_n}\right)+\dot{S}_{gen_{dc}}=0 \quad (119)$$

where s_{sw_1} denotes the specific entropy of seawater entering the down condenser.

3.4 Thermal Storage

In order for the system to run in the absence of solar irradiation (at night), the use of thermal storage is indispensable. In this section, the mathematical modeling of a two tank thermal storage utilizing molten salt as a storage medium is present. The thermal storage is illustrated in Figure 3.9.

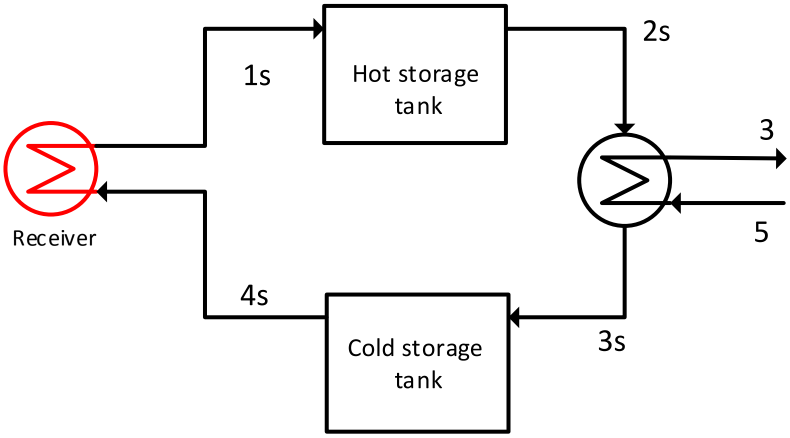

Figure 3.9 Two tank thermal heat storage schematic

3.4.1 Hot Storage Tank

The energy conservation law applied on the hot storage tank implies,

$$M_{hst} \frac{du_{hst}}{dt} = Q_{1s} - Q_{hst} - Q_{2s} \tag{120}$$

Rearranging and assuming a discrete interval instead of the infinitesimal time derivative,

$$M_{hst}^{+} u_{hst}^{+} = M_{hst} u_{hst} + \Delta t \left(Q_{1s} - Q_{hst} - Q_{2s} \right) \tag{121}$$

M_{hst} is defined as the mass of the hot storage tank fluid, u_{hst} denotes the hot storage internal energy after an interval of Δt. The loss to the ambient from the hot tank is denoted by Q_{hst} and is given by the following:

$$Q_{hst} = U_{hst} A_{hst} (T_{hst} - T_{amb}) \tag{122}$$

where A_{hst} is the heat transfer area, U_{hst} is the overall heat transfer coefficient, and T_{hst} is the temperature of the hot storage tank.

3.4.2 Cold Storage Tank

Applying energy balance on the cold storage tank,

$$M_{cst} \frac{du_{cst}}{dt} = Q_{3s} - Q_{cst} - Q_{4s} \tag{123}$$

Rewritten in the same fashion done for the hot storage tank,

$$M_{cst}^{+} u_{cst}^{+} = M_{cst} u_{cst} + \Delta t \left(Q_{3s} - Q_{cst} - Q_{4s} \right) \tag{124}$$

where M_{cst} represents the mass of the cold storage tank fluid, u_{cst}^{+} denotes the cold storage tank internal energy after an interval of Δt. The loss to the ambient from the cold tank is denoted by Q_{cst} and is given by the following equation:

$$Q_{cst} = U_{cst} A_{cst} (T_{cst} - T_{amb}) \tag{125}$$

where A_{cst} is the heat transfer area, U_{cst} is the overall heat transfer coefficient, and T_{cst} is the temperature of the cold storage tank.

3.5 Heat Exchangers

The modeling of the heat exchangers to be used in linking the components of the cogeneration system is present in this section. The equation defining the effectiveness of the heat exchanger is as follows:

$$\varepsilon_s = \frac{\dot{m} C_{p_{co}} (T_{co} - T_{ci})}{(\dot{m} C_p)_{\min} (T_{hi} - T_{ci})} \tag{126}$$

The subscrips co ,ci , and hi denote the cold fluid out, cold fluid in, and hot fluid in respectively.

3.6 Components Exergy Analysis

In order to analyze the system's components from a second law of thermodynamics viewpoint, an exergetic analysis is applied to each of the components of the cogeneration system. The first term being the exergetic fuel depletion ratio defined as the ratio of exergy destruction in a component to the total input flow exergy to the system given by,

$$Y_{\text{comp},j} = \frac{Ex_{\text{comp},j}}{Ex_{in,\text{total}}} \tag{127}$$

Another term utilized in exergy analysis is the irreversibility ratio of a component defined as the ratio of exergy destruction in a component to the total exergy destroyed in the cogeneration system as a whole, its expression is given by,

$$Y^*_{\text{comp},j} = \frac{Ex_{\text{comp},j}}{Ex_{D,total}} \tag{128}$$

The ratio of exergy destruction in a component to the input flow exergy to the component is given by,

$$Z_{\text{comp},j} = \frac{Ex_{\text{comp},j}}{Ex_{in,j}} \tag{129}$$

The last term in the components exergy analysis is the improvement potential, given by the following equation:

$$IP_{comp,j} = (1 - \frac{\eta_{cog_{sep}}}{100}) Ex_{\text{comp},j} \tag{130}$$

3.7 Solar Cogeneration Configurations

The modeling of the components of the solar cogeneration system is studied in details in the previous sections of this chapter. In this section, the way of integration forming the configurations that the study will be based upon will be discussed. Two configurations are basically studied, a solar cogeneration system utilizing solar tower integrated with a thermal heat storage used to drive a supercritical CO_2 cycle and a MEE-TVC desalination system. The difference between the two configurations is the use of a regenerative sCO_2 cycle in the first (Figure 3.10) and a recompression sCO_2 cycle in the second for comparison (Figure 3.11).

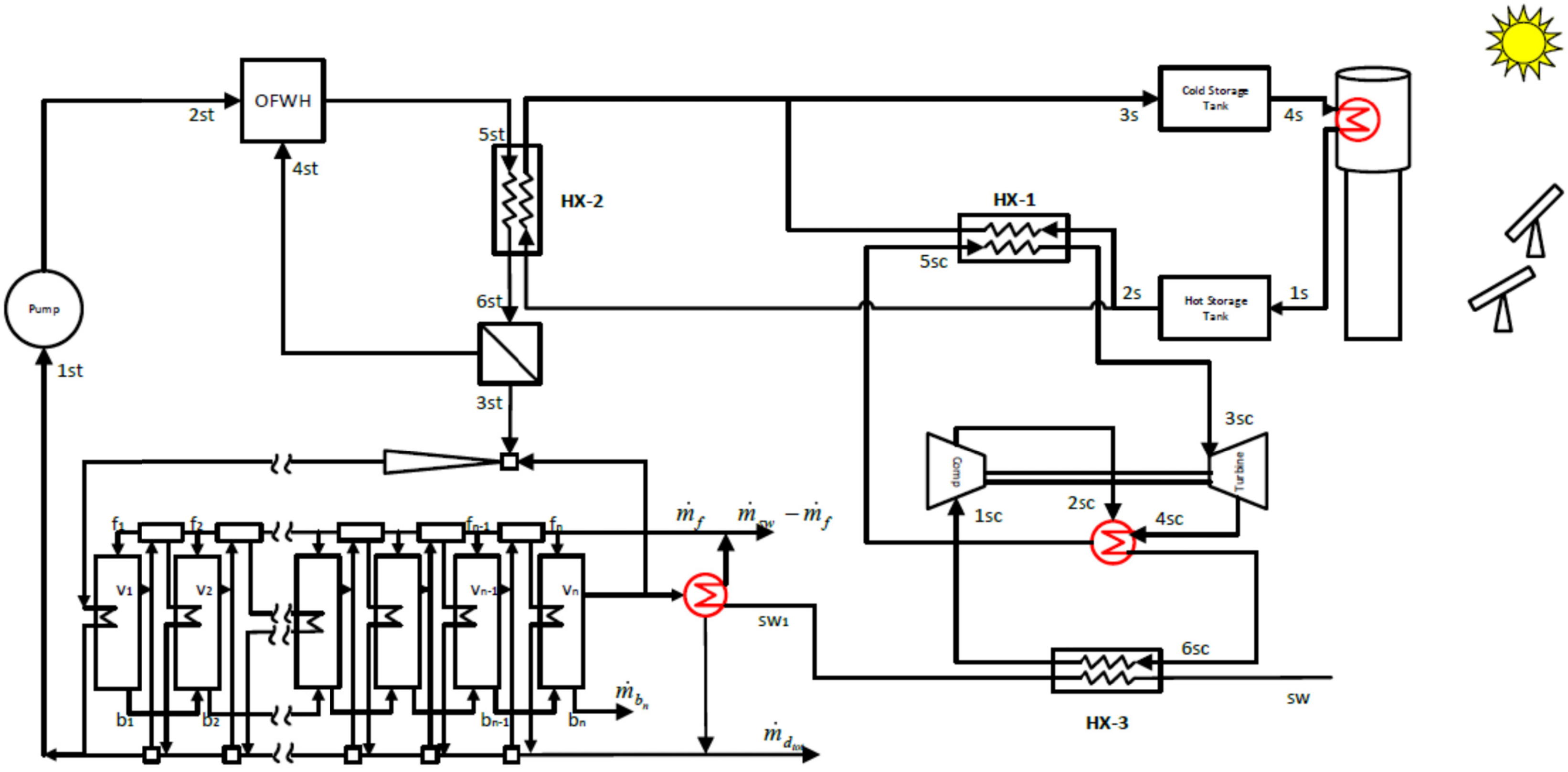

Figure 3.10 Solar cogeneration system utilizing regenerative sCO_2 cycle (Configuration 1)

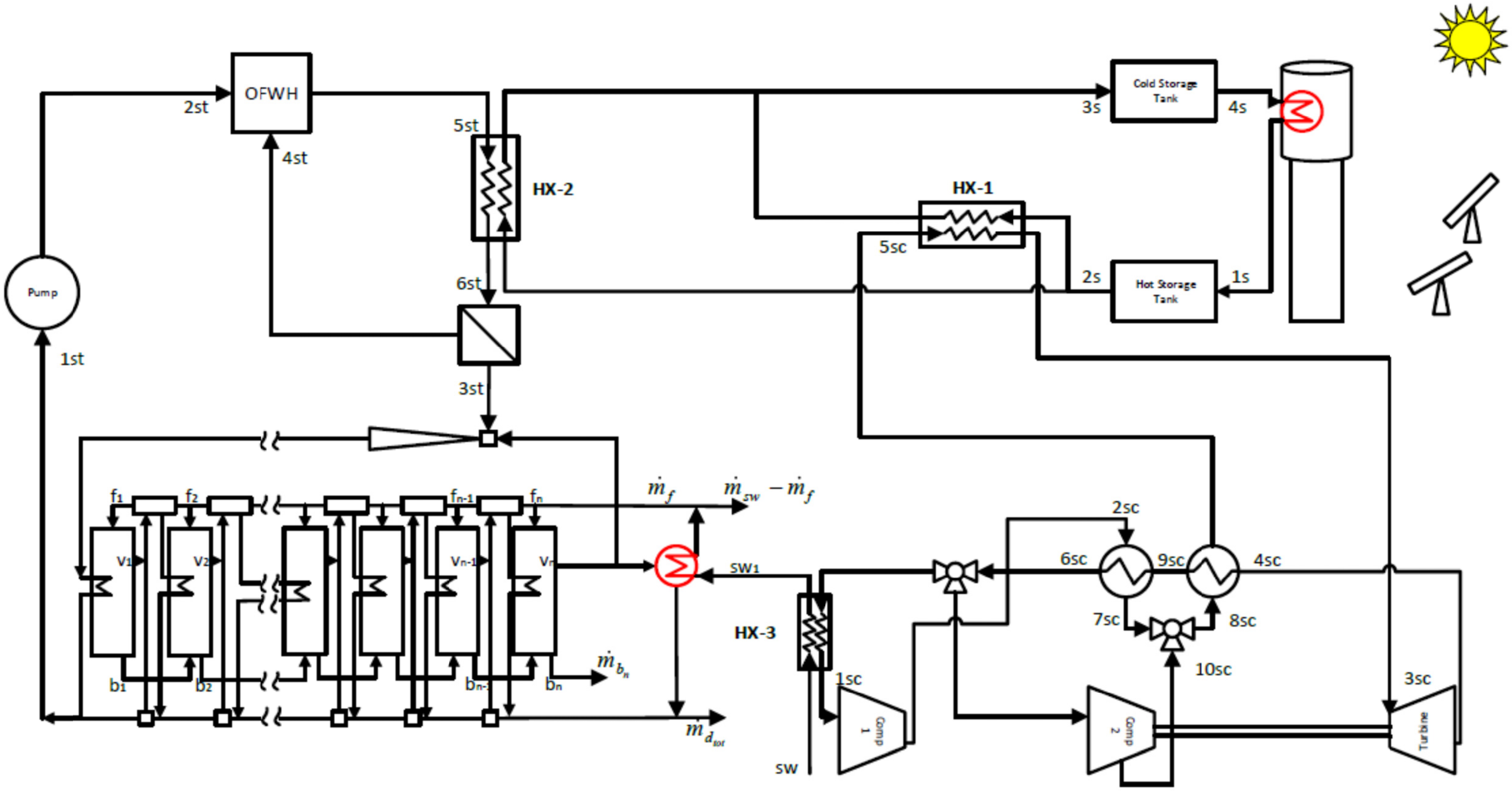

Figure 3.11 Solar cogeneration system utilizing recompression sCO_2 cycle (Configuration 2)

For the sake of explanation, it is worthy of noting that the cooler defined previously in the mathematical modeling of the sCO$_2$ cycles serve as a preheater for the incoming seawater in the configurations shown and is denoted by HX-3. Two heat exchangers from the thermal storage are utilized as well, one serving as a source of heat to the sCO$_2$ cycle, denoted by HX-1, and the other as a source of heat to the steam in the MEE-TVC desalination system, denoted by HX-2. It is therefore useful to state the energy balance and entropy generation equations applied on these heat exchangers. For HX-1, the energy balance equation implies,

$$\dot{m}_{2s}(\mathrm{f})(h_{2s} - h_{3s}) = \dot{m}_{CO_2}(h_{3sc} - h_{5sc}) \tag{131}$$

The entropy generation in HX-1 is calculated by,

$$\dot{m}_{2s}(\mathrm{f})(\mathrm{s}_{2s} - s_{3s}) + \dot{m}_{CO_2}(\mathrm{s}_{5sc} - s_{3sc}) + \dot{\mathrm{S}}_{genHX-1} = 0 \tag{132}$$

where $\dot{m}_{2s}$ is the total mass flow rate of molten salt leaving the hot storage tank, h_{2s} and h_{3s} are the enthalpy states of molten salt leaving the hot storage tank and entering the cold storage tank respectively. f is the fraction of molten salt flow rate passing through HX-1, thus, accounted for the sCO$_2$ power cycle. s_{2s} and s_{3s} are the entropy states of molten salt leaving the hot storage tank and entering the cold storage tank respectively. The entropy generation rate in HX-1 is denoted by $\dot{\mathrm{S}}_{genHX-1}$.

Applying the energy balance over HX-2,

$$\dot{m}_{2s}(1 - \mathrm{f})(h_{2s} - h_{3s}) = \dot{m}_{5st}(h_{6st} - h_{5st}) \tag{133}$$

The entropy generation in HX-3 is calculated by,

$$\dot{m}_{2s}(1-\mathrm{f})(\mathrm{s}_{2s}-s_{3s})+\dot{m}_{5st}(\mathrm{s}_{5st}-s_{6st})+\dot{\mathrm{S}}_{genHX-2}=0 \tag{134}$$

where $\dot{m}_{5st}$ is the mass flow rate of steam entering HX-2, and s_{5st} and s_{6st} are the entropy states of steam entering and leaving HX-2 respectively. The entropy generation rate in HX-2 is denoted by $\dot{\mathrm{S}}_{genHX-2}$.

Applying the energy and entropy balance on HX-3, we get, for the regenerative solar cogeneration cycle,

$$\dot{m}_{CO_2}(h_{6sc}-h_{1sc})=\dot{m}_{sw}(h_{sw1}-h_{sw}) \tag{135}$$

$$\dot{m}_{CO_2}(\mathrm{s}_{6sc}-s_{1sc})+\dot{m}_{sw}(\mathrm{s}_{sw}-s_{sw1})+\dot{\mathrm{S}}^{reg}_{genHX-3}=0 \tag{136}$$

where h_{sw} and h_{sw1} are the enthalpy states of seawater entering and leaving HX-3 respectively, s_{sw} and s_{sw1} are the entropy states of the seawater entering and leaving HX-3 respectively. The entropy generation rate in HX-3 for the regenerative solar cogeneration case is denoted by $\dot{\mathrm{S}}^{reg}_{genHX-3}$.

For the recompressive solar cogeneration cycle case, the energy and entropy balance over HX-3 implies,

$$x\dot{m}_{CO_2}(h_{6sc}-h_{1sc})=\dot{m}_{sw}(h_{sw1}-h_{sw}) \tag{137}$$

$$x\dot{m}_{CO_2}(\mathrm{s}_{6sc}-s_{1sc})+\dot{m}_{sw}(\mathrm{s}_{sw}-s_{sw1})+\dot{\mathrm{S}}^{rec}_{genHX-3}=0 \tag{138}$$

x is the fraction of CO_2 mass flow rate entering the first compressor in the recompressive power cycle and $\dot{S}^{rec}_{genHX-3}$ denotes the entropy generation rate in HX-3 for the recompressive solar cogeneration cycle case.

The entropy generation in the HST and the CST of the thermal storage is calculated for the whole day by,

$$\sum_{SH} \dot{m}_{1s} s_{1s} - 24\dot{m}_{2s} s_{2s} - 24\frac{Q_{hst_{day}}}{T_{amb}} + S_{gen_{HST}} = 0 \tag{139}$$

$$24\dot{m}_{3s} s_{3s} - \sum_{SH} \dot{m}_{4s} s_{4s} - 24\frac{Q_{cst_{day}}}{T_{amb}} + S_{gen_{CST}} = 0 \tag{140}$$

The entropy generation in the solar tower per day is given by the following [19]:

$$\frac{Q_{solar_{day}}}{T_{sun}} - \frac{Q_{solar_{lost_{day}}}}{T_{amb}} + \sum_{SH} \dot{m}_{1s} \left(s_{4s} - s_{1s}\right) + S^{ST}_{gen} = 0 \tag{141}$$

3.7.1 Cogeneration Cycle Efficiency

In order to evaluate the performance of the cogeneration cycle as a whole, defining efficiency for our system as a ratio of output energy to input solar energy is indispensable. From literature, the first law efficiency can be defined in two ways, the well-known conventional way relating the work output of the system to the heat input, given by the equation,

$$\eta_{conv} = \frac{W_{net_{power}}}{Q_{solar_{day}}} \tag{142}$$

Equation (142) however, if used for the cogeneration system in this study, underestimates the system's performance since it does not account for the desalinated water product from the MEE-TVC desalination system. The other way of evaluating the cogeneration system's performance is by calculating the utilization factor [87], [88]. The utilization factor is given by the following equation:

$$UF = \frac{W_{net_{power}} + Q_{des}}{Q_{solar_{day}}} \tag{143}$$

As one can see from equation(143), the utilization factor is calculated by adding the work output of the power cycle to the heat input into the desalination system, therefore, accounting for power and water output from the cogeneration cycle. However, although heat and work are expressed in the same units, the utilization factor accounts for the work and heat as having the same quality, which is false from a second law view point, thus, overestimating the cogeneration system's performance. Therefore, the problem is in the identification of an expression for the exergy of pure water, in a way that makes its comparison to the power output possible from both, the first and second law view point. Mistry et al.[89], [90] defined the exergy of pure water from desalination processes as the minimum least work of separation required to split the incoming seawater feed stream into brine and product water. The work of separation is illustrated in Figure 3.12

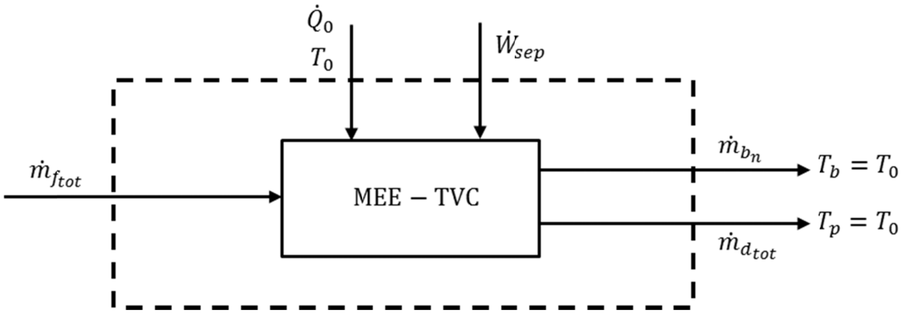

Figure 3.12 Work of Separation

The selection of the control volume far away from the physical plant is to demonstrate that the exergy of the product water due to thermal disequilibrium with the environment is not useful, as well as that of brine due to chemical and thermal disequilibrium with the environment. Therefore, they will be included in the entropy generation term.

Following the same procedure as Mistry et al. [89]–[91], applying first and second law balance on the distant control volume,

$$\dot{W}_{sep} + \dot{Q} + \dot{m}_{f_{tot}} h_{sw} = \dot{m}_{d_{tot}} h_{d_{fn}} + \dot{m}_{b_n} h_{b_n} \tag{144}$$

$$\frac{\dot{Q}}{T_0} + \dot{m}_{f_{tot}} s_{sw} + \dot{S}_{gen^{desalination}} = \dot{m}_{d_{tot}} s_{d_{fn}} + \dot{m}_{b_n} s_{b_n} \tag{145}$$

Multiplying equation (145) by temperature T_0 and subtracting it from equation(144), we obtain an expression for the work of separation given by,

$$\dot{W}_{sep} = \dot{m}_{d_{tot}} g_p + \dot{m}_{b_n} g_b - \dot{m}_{sw} g_{sw} + T_0 \dot{S}_{gen}^{RDS} \tag{146}$$

The superscript RDS denotes the restricted dead state which implies that the term refers to the entropy generated due to the system being brought to thermal and mechanical equilibrium with the environment, but chemical disequilibrium due to the difference in the salinity of rejected brine and seawater. The terms g_p , g_b , and g_{sw} refer to the specific free gibbs energy of product water, brine, and incoming seawater respectively. The least work of separation, however, is that of the operation under reversible conditions, hence, the entropy generation term is excluded, and the equation becomes,

$$\dot{W}_{sep_{least}} = \dot{m}_{d_{tot}} g_p + \dot{m}_{b_n} g_b - \dot{m}_{sw} g_{sw} \tag{147}$$

Combining equations (146) and (147) results in,

$$\dot{W}_{sep} = \dot{W}_{sep_{least}} + T_0 \dot{S}_{gen}^{RDS} \tag{148}$$

However, it was stated that the exergy associated with pure water, which is needed to define the efficiency of the system, is the minimum least work of separation. Unlike the least work of separation, the minimum least work of separation requires the outlet brine to reach thermal, mechanical, and chemical equilibrium with the environment. Thus, it could be found by the following equation,

$$\dot{W}_{sep} = \dot{W}_{sep_{least}}^{\min} + T_0 \dot{S}_{gen}^{TDS} \tag{149}$$

The superscript TDS denotes the total dead state referring to thermal, mechanical, and chemical equilibrium with the surrounding environment, given,

$$\dot{S}_{gen}^{TDS} = \dot{S}_{gen}^{RDS} + \dot{S}_{gen}^{brine\ RDS \to TDS} \tag{150}$$

The term $\dot{S}_{gen}^{brine\ RDS \to TDS}$ refers to the entropy generated in bringing the brine to chemical equilibrium with the environment.

In order to deduce an expression for thermal efficiency, a simplifying schematic of the cogeneration cycles in this study is present in Figure 3.13.

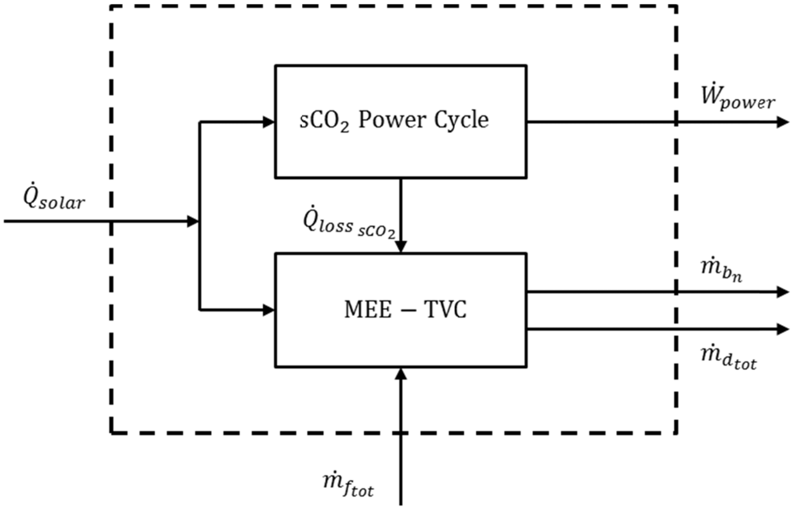

Figure 3.13 Cogeneration System Schematic

The first law efficiency represents the ratio of exergy of product, work output from the power cycle and exergy of pure water, to the heat input to the system, namely, solar energy. Thus, an additional form of the efficiency is given by,

$$\eta_{cog_{sep}} = \frac{W_{net_{power}} + W_{sep_{least}}^{\min}}{Q_{solar_{day}}} \tag{151}$$

Equation (151) represents a better expression of the first law efficiency compared to the previous expressions, the utilization factor which overestimates the performance of the cogeneration system and the conventional ratio of electrical work output to input energy which underestimates the performance of a system by not giving any regard to the water output. Thus, $\eta_{cog_{sep}}$ results in values in between. Although this might seem the most appropriate, the fact is that desalination systems, especially thermal desalination systems, are highly entropy generating processes, therefore, the entropy generation term in the expression of the work of separation in equation (149) largely exceeds the minimum least work of separation term, thus, resulting in a very low second law efficiency $(\dot{W}_{sep_{least}}^{\min} / \dot{W}_{sep})$ [89]–[91]. Therefore, in spite the fact that the values for such an expression for the second law efficiency would be in between those for the conventional and utilization factor expressions, the fact is, that the results will be closer to that of the conventional rather than the utilization factor. This would give a false impression that the first law efficiency of the cogeneration system is lower than the efficiency of running the system generating only electrical power with no fraction accounted for desalination.

However, in a further attempt to prove the superiority of the cogeneration system, an extra first law efficiency expression is to be derived. In order to prove this method, it should be first noted that the difference in running a standalone MEE-TVC desalination system and as part of the cogeneration system under study is that the number of effects in the cogeneration configuration can be increased. The reason is, as stated earlier in this chapter, that the temperature of the incoming seawater is increased allowing for enough feed seawater at the desired temperature to enter the system. Therefore, a new term for the heat accounted for desalination is to be defined, this term is referred to as the effective desalination input heat (Q_{des}^{eff}). The latter is not an actual heat input to the desalination system like the fraction of heat input into the desalination system (Q_{des}), rather, it is an imaginary value related to it by the mass flow rate of the output product water. Moreover, it is defined as the input heat required to extract the same amount of product water from the standalone desalination system that we can extract from the same desalination system working as a part of the cogeneration process. By logic, however, for a standalone case, it would require more heat to extract the same amount of product water resulting from cogeneration since the number of effects is less for the standalone case, and thus, less GOR.

The expression for the effective efficiency therefore shall be as follows:

$$\eta_{cog_{eff}} = \frac{W_{net_{power}} + Q_{des}^{eff}\, \eta_{th_{power}}}{Q_{solar_{day}}} \tag{152}$$

It could be seen in expression of equation (152) that the effective desalination input is multiplied by the efficiency of the power cycle. This serves in the favor of equalizing the quality of energy received from the power and desalination cycles. In other words, the term $Q_{des}^{eff}\, \eta_{th_{power}}$ is the amount of theoretical work produced from the effective desalination input heat if used in the power cycle of the cogeneration system.

An extra effective efficiency is also defined as the effective output divided by the net energy gained at the level of the central receiver, given by,

$$\eta_{cog_{rec}} = \frac{W_{net_{power}} + Q_{des}^{eff}\, \eta_{th_{power}}}{Q_{receiver}} \tag{153}$$

3.8 Cost Analysis

The levelized cost of energy is the per kilowatt hours of real currency stated here in dollars. To be more precise, the numerator of LCOE is a complete guide to summing up the project's capital cost with the cost of operation and maintenance and fuel costs [92], having the last to be null in this research for having the project to be a type of full clean energy concept. The denominator is the total energy generated for a period of time, here being 30 years converting it to hours by multiplying the years by the number 8760 which is the number of hours in 1 year. The more one can reduce levelized cost, the more the project is said to be economically attractive. It will be more preferable when a utility can be generating more kilowatt-hours at the same costs or in other sense decreasing the cost while maintaining the same energy generation and output production. To be more accurate, levelized cost of energy varies from region to another according to some parameters such as federal taxes, insurances, etc. Therefore it is necessary to define another term that will help make a difference in comparing distinct technologies. The capacity factor is known to be the ratio of the real power output reached to the nameplate capacity, where the nameplate capacity is simply a theoretical value of power output or the peak power considered. A capacity factor of 70% can be reached for a plant with thermal storage, and this value is used for calculation in this research [93]. The following formula is to be used assuming the project is not charged by any interest rate:

$$LCOE = \frac{\left[1+\frac{(C_i + C_L)}{100}\right] \times \begin{bmatrix} P_o \times 10^3 \times (CC_{cycle} + 8.76 \times OM_{\text{cycle}} \times N \times 10^3) \\ + W_p \times (CC_{med-tvc} + OM_{med-tvc}) \\ + (C_{storage} + OM_{storage}) \times SS_m \\ + CC_{sf} \times \mathrm{A}_s \end{bmatrix}}{E_t} \tag{154}$$

where E_t is the total lifetime energy generated,

$$E_t = 8760 \times P_o \times N$$

Levelized Cost of Water

Another method to compare different technologies efficiently is the use of LCOW or the Levelized cost of water. LCOW is calculated by evaluating the overall project expenditures including operation and maintenance costs divided this time by the amount of potable water produced. Therefore we obtain a value having the unit of dollars per cubic meters [94].

$$LCOW = \frac{\left[1+\frac{(C_i+C_L)}{100}\right]\times\begin{bmatrix} P_o\times10^3\times(CC_{cycle}+8.76\times OM_{\text{cycle}}\times N\times10^3) \\ +W_p\times(CC_{med-tvc}+OM_{med-tvc}) \\ +(C_{storage}+OM_{storage})\times SS_m \\ +CC_{sf}\times \mathrm{A}_s \end{bmatrix}}{W_T} \qquad (155)$$

where

$W_T = 365\times W_p\times N$

Net Levelized Cost of Energy

In order to evaluate the net cost of the total system, the use of a levelized cost based on the energy output from the power cycle and the work of separation from the desalination system is utilized, the equation is written as follows:

$$LCOE_{WS} = \frac{\left[1+\frac{(C_i+C_L)}{100}\right]\times\begin{bmatrix} P_o\times10^3\times(CC_{cycle}+8.76\times OM_{\text{cycle}}\times N\times10^3) \\ +W_p\times(CC_{med-tvc}+OM_{med-tvc}) \\ +(C_{storage}+OM_{storage})\times SS_m \\ +CC_{sf}\times \mathrm{A}_s \end{bmatrix}}{8760\times(P_o+\dot{W}_{sep_{least}}^{\min})\times N} \qquad (156)$$

CHAPTER 4

RESULTS AND DISCUSSION

In this chapter, the results of the thermodynamic performance of the cogeneration systems will be presented. The mathematical formulation written previously is implemented into the EES software for the parametric studies of different operational parameters and their effect on the thermodynamic performance of the system as a whole. The study is carried out for different cities in Saudi Arabia to be listed in later sections of this chapter. A basic cost analysis involving capital and operating costs is studied as well. Furthermore, entropy generation in the cogeneration system components is analyzed.

4.1 Solar Tower

4.1.1 Heliostat Field Operating Parameters

It is essential to state the basic operating parameters prior to presenting calculation results concerning the solar tower system's performance. Therefore, stated in Table 4.1, is the basic sizing of the heliostats and the central receiver [11], [14], [16], [95].

Table 4.1 Basic design of the heliostats and the central receiver [14], [16], [95].

Number of Heliostats	2646
Heliostat height, LH	9.75 m
Heliostat width, LW	12.3 m
Heliostat mirror area fraction	0.9642
Tower height, THT	130 m
Receiver size LR	9.44 m
Receiver diameter DR	9.44 m
Mirror reflectivity × cleanliness	0.88 × 0.95
Emissivity of the receiver surface, ε	0.85
Absorptivity of the receiver surface, α	0.95

The annual optimization of the heliostat field is carried out by Atif and Al-Sulaiman [11]. The optimization is done under the design considerations stated in Table 4.1. One of the results pertaining to the optimization of the heliostat field in the region of Dahran, KSA, by Atif and Al-Sulaiman is visualized in the difference of the contours of un-optimized and optimized heliostat fields shown in Figure 4.1 and Figure 4.2, respectively. The contours of the optical efficiency of the un-optimized heliostat field is described with slight discontinuities in the transition from one zone to the other, however, this discontinuity vanishes to a certain extent due to optimization.

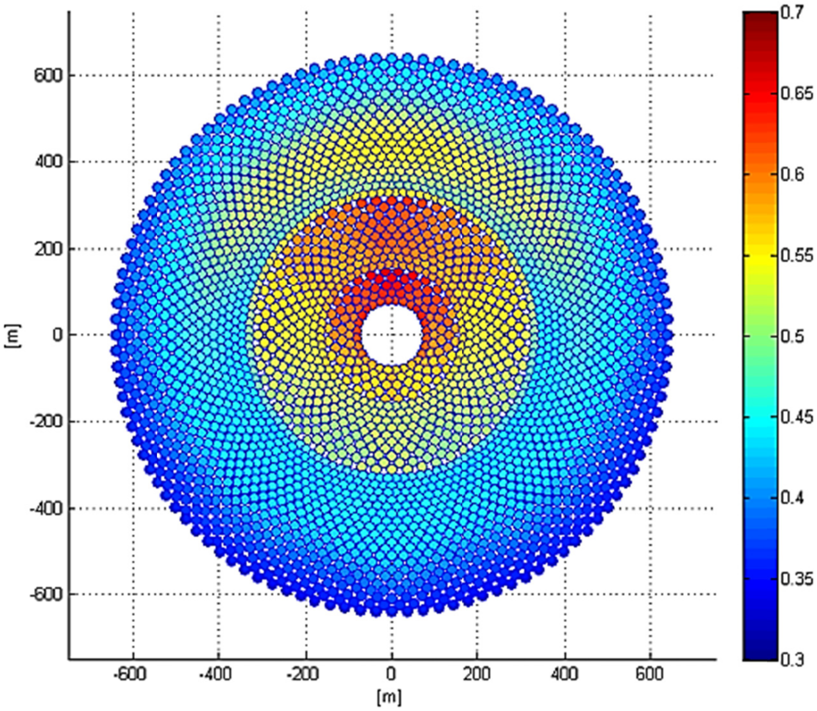

Figure 4.1 Contours of the optical efficiency of the un-optimized heliostat field on annual basis for Dhahran, Saudi Arabia.[11]

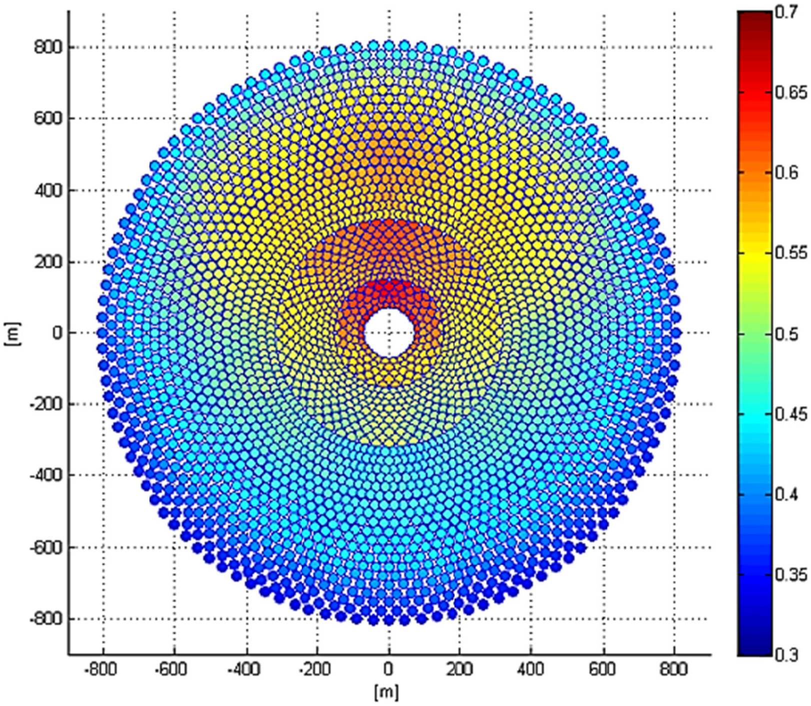

Figure 4.2 Contours of the optical efficiency of the optimized heliostat field on annual basis for Dhahran, Saudi Arabia.[11]

Moreover, the average annually optimized efficiency is obtained by optimizing the azimuthal spacing and radial spacing using four variables [11]. The optimum parameters were found for the cities of Dhahran, Tabouk, Riyadh, Najran, Madinah, and Bishah. However, for the analysis of solar cogeneration of power and desalination to make sense, the use of the same coordinates might be misleading since some of the mentioned cities do not lie on the sea, and thus, should be eliminated from the study. However, the optical efficiency calculated depends on the latitude, but has no dependence on the longitude of the region under consideration, and thus, finding the cities that lie on the shore of the Kingdom of Saudi Arabia and coincide with the latitudes of the cities studied by Atif and Al-Sulaiman [11] is recommended and is to be considered in this study. The cities studied, are stated in Table 4.2 below with their latitudes and longitudes.

Table 4.2 Basic geographic data for different cities in Saudi Arabia

Location	Latitude	Longitude	Sea
Dhahran	26.5 ° N	50.5 ° E	Arabian Gulf
Yanbu Al-Nakhil	24.5 ° N	37.4 ° E	Red Sea
Jizan	17.5 ° N	42.24 ° E	Red Sea
Khabt Al-Ghusn	20.5 ° N	39.64 ° E	Red Sea
Al-Khafji	28.5 ° N	48.5 ° E	Arabian Gulf
Jabal Al Rughamah	28.5 ° N	34.8 ° E	Gulf of Aqaba

4.1.2 Direct Normal Irradiation Information

The monthly averaged data for direct normal irradiation for different geographic locations found in Table 4.3 are obtained averaged over 22 year period from a renewable energy website sponsored by NASA [96].

4.1.3 Heat Collected at the Central Receiver Level

In this subsection, the average heat collected at the central receiver is calculated for each month of the year for the different locations of Saudi Arabia stated in Table 4.2. Although the optimum parameters of the optical efficiency do not change for the same latitude, the difference in longitude is associated with a difference in the direct normal irradiance. Furthermore, at the level of the central receiver, the heat losses encountered are radiation, convection, and conduction heat losses. The latter is negligible compared to the rest of the losses associated. Radiation losses, however, have more impact than convection losses due to the high concentration ratios of the solar tower system. The energy obtained at the level of the central receiver is the direct normal irradiation with the optical losses from the heliostat field, radiation, convection, and conduction eliminated. Figure 4.3 through Figure 4.8 represent the monthly averaged daily heat collected at the central receiver level for Dhahran, Yanbu Al-Nakhil, Jizan, Khabt Al-Ghusn, Al-Khafji, and Jabal Al-Rughamah respectively.

Table 4.3 Monthly Averaged Direct Normal Irradiation for different locations of Saudi Arabia

	Dhahran		Yanbu		Jabal Al-Rughamah		Khabt Al-Ghusn		Al-Khafji		Jizan	
	DNI $(\frac{kWh}{m^3 / day})$	DH (hours)	DNI $(\frac{kWh}{m^3 / day})$	DH (hours)	DNI $(\frac{kWh}{m^3 / day})$	DH (hours)	DNI $(\frac{kWh}{m^3 / day})$	DH (hours)	DNI $(\frac{kWh}{m^3 / day})$	DH (hours)	DNI $(\frac{kWh}{m^3 / day})$	DH (hours)
Month												
January	4.92	10.7	6.91	10.8	6.22	10.5	6.94	11	5.25	10.5	5.95	11.2
February	5.49	11.3	7.63	11.3	6.66	11.2	7.38	11.5	6.01	11.2	6.1	11.5
March	5.43	12	7.78	12	7.04	12	7.95	12	5.61	12	6.75	12
April	5.98	12.7	8.17	12.7	7.23	12.8	8.32	12.6	5.49	12.8	7.27	12.5
May	7.27	13.4	7.83	13.3	7.68	13.5	8.38	13.1	6.62	13.5	7.04	12.9
June	8.48	13.7	9.03	13.6	8.85	13.9	8.36	13.3	8.28	13.9	6.62	13.1
July	7.65	13.6	8.59	13.5	8.48	13.7	7.9	13.2	7.98	13.7	6.1	13
August	7.62	13	7.99	12.9	8.11	13.1	7.67	12.8	7.98	13.1	5.68	12.7
September	7.77	12.3	7.77	12.3	7.51	12.3	7.64	12.2	8.07	12.3	6.4	12.2
October	7.1	11.5	7.35	11.6	6.28	11.5	7.82	11.7	6.86	11.5	7.28	11.7
November	5.63	10.8	7.17	10.9	6.02	10.7	7.01	11.1	5.24	10.7	6.65	11.3
December	4.63	10.5	6.68	10.6	5.76	10.3	6.47	10.9	4.69	10.3	6.47	11.1

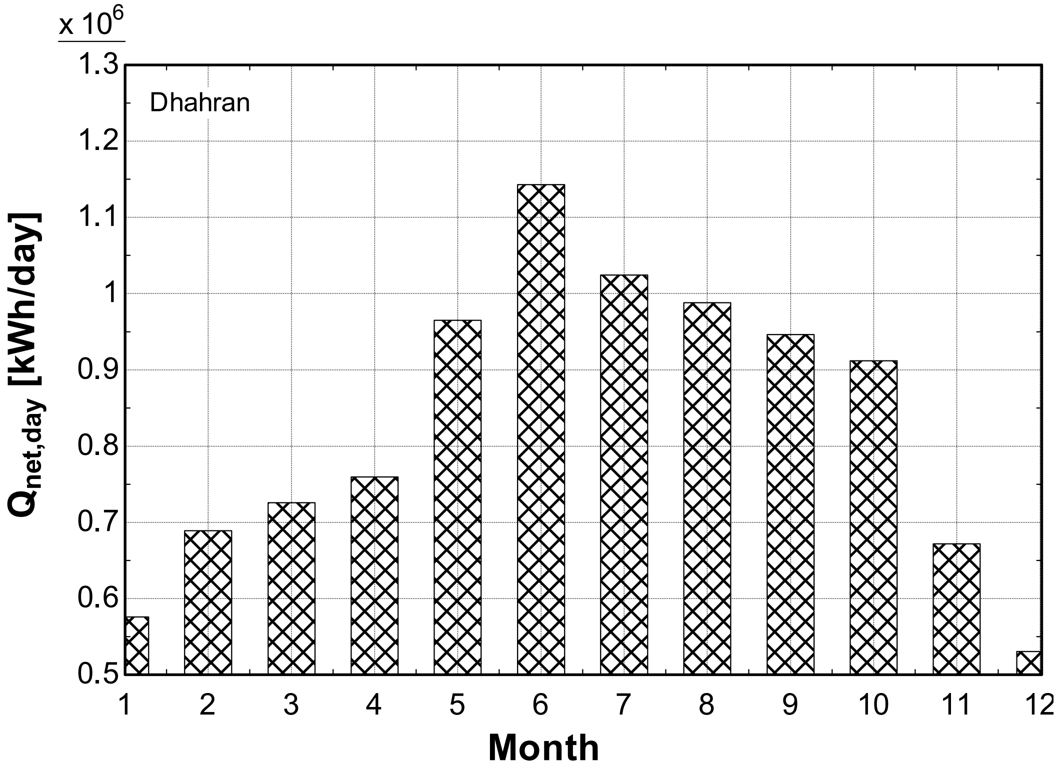

Figure 4.3 Monthly average heat per day collected at the receiver level for Dhahran, Saudi Arabia

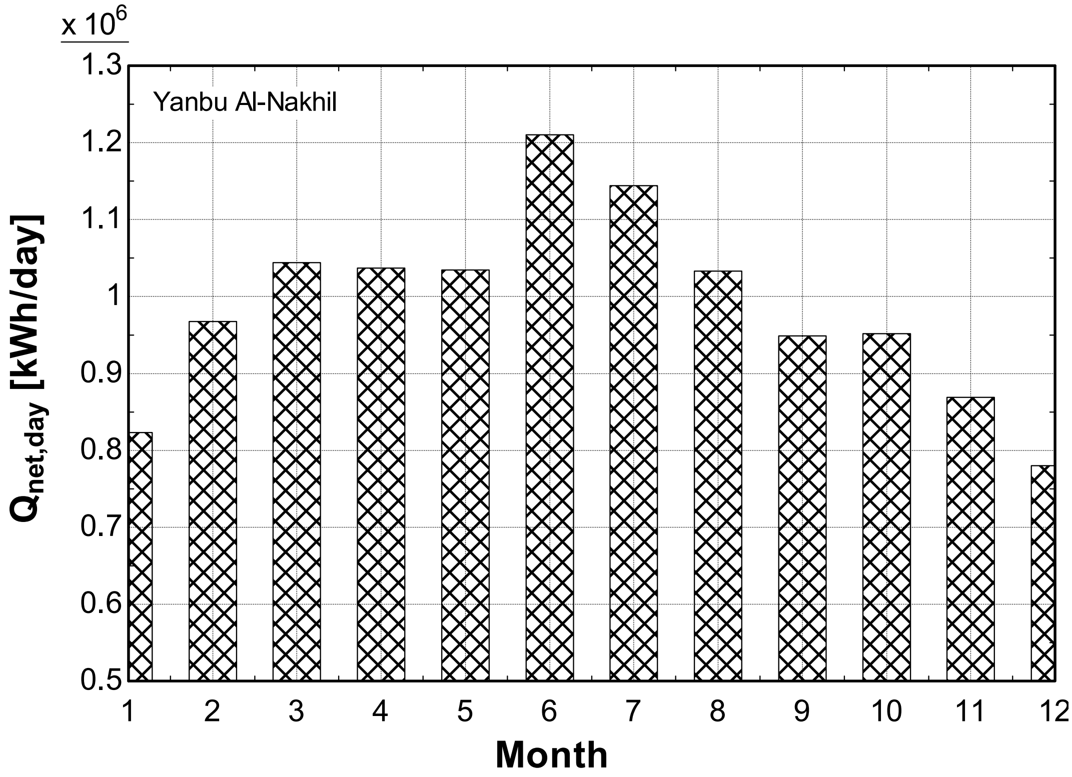

Figure 4.4 Monthly average heat per day collected at the receiver level for Yanbu Al-Nakhil, Saudi Arabia

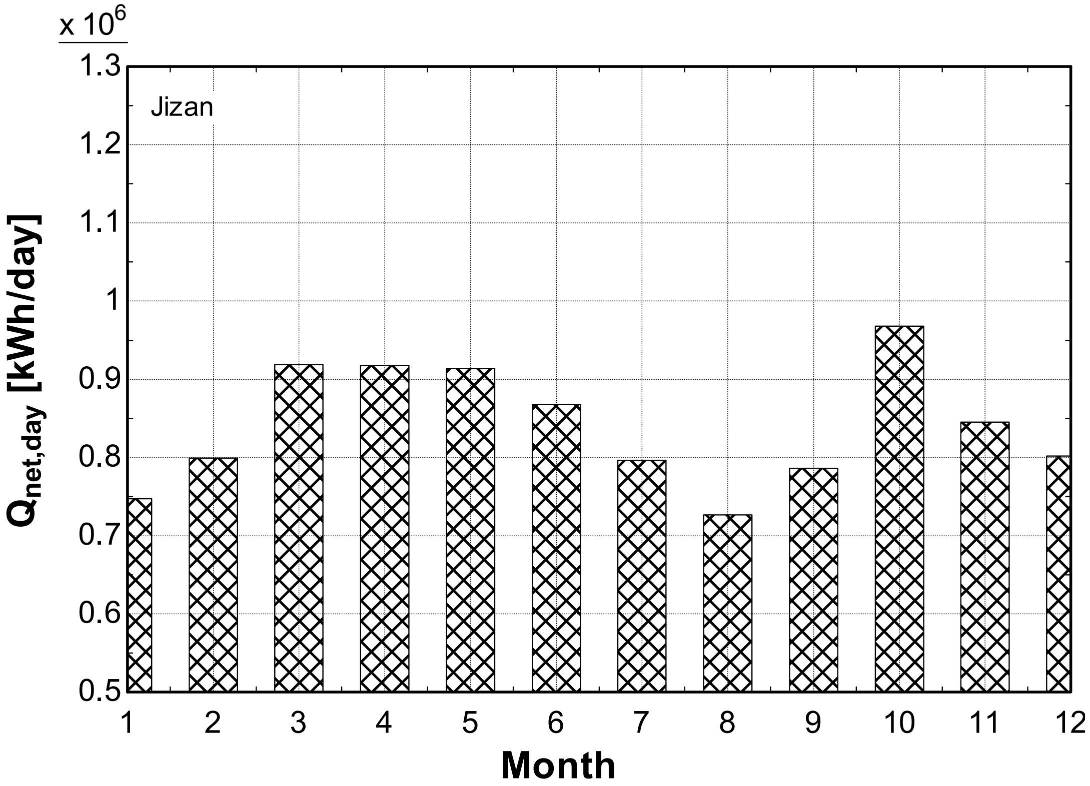

Figure 4.5 Monthly average heat per day collected at the receiver level for Jizan, Saudi Arabia

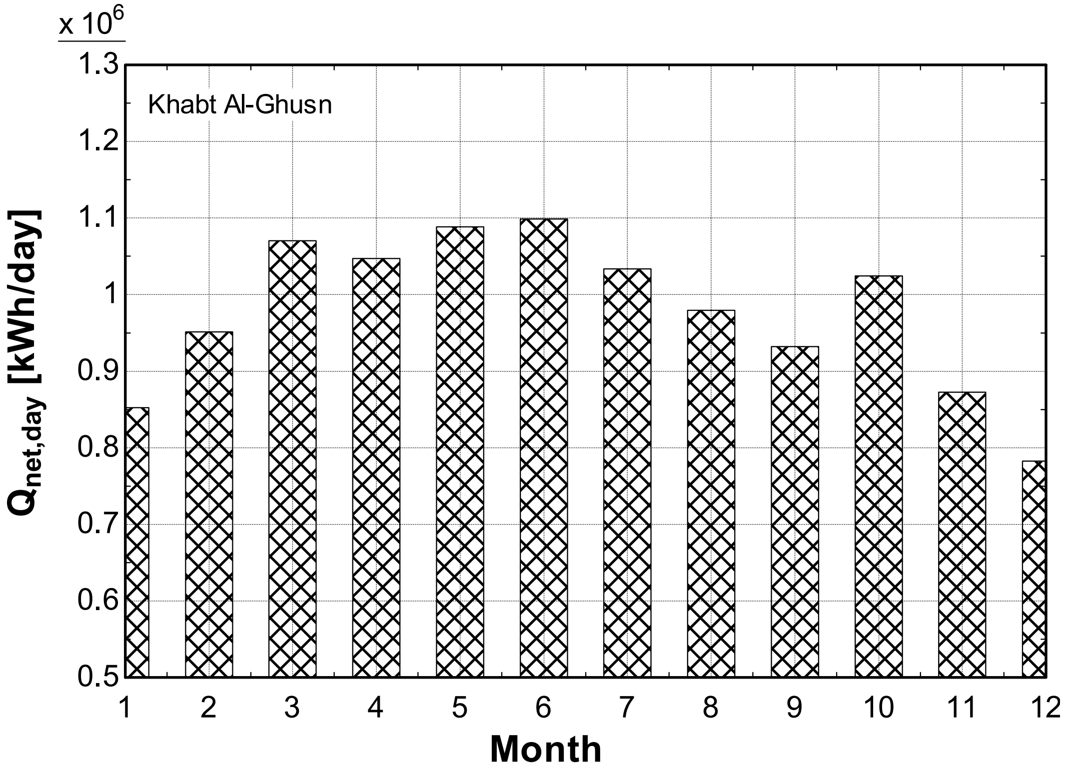

Figure 4.6 Monthly average heat per day collected at the receiver level for Khabt Al-Ghusn, Saudi Arabia

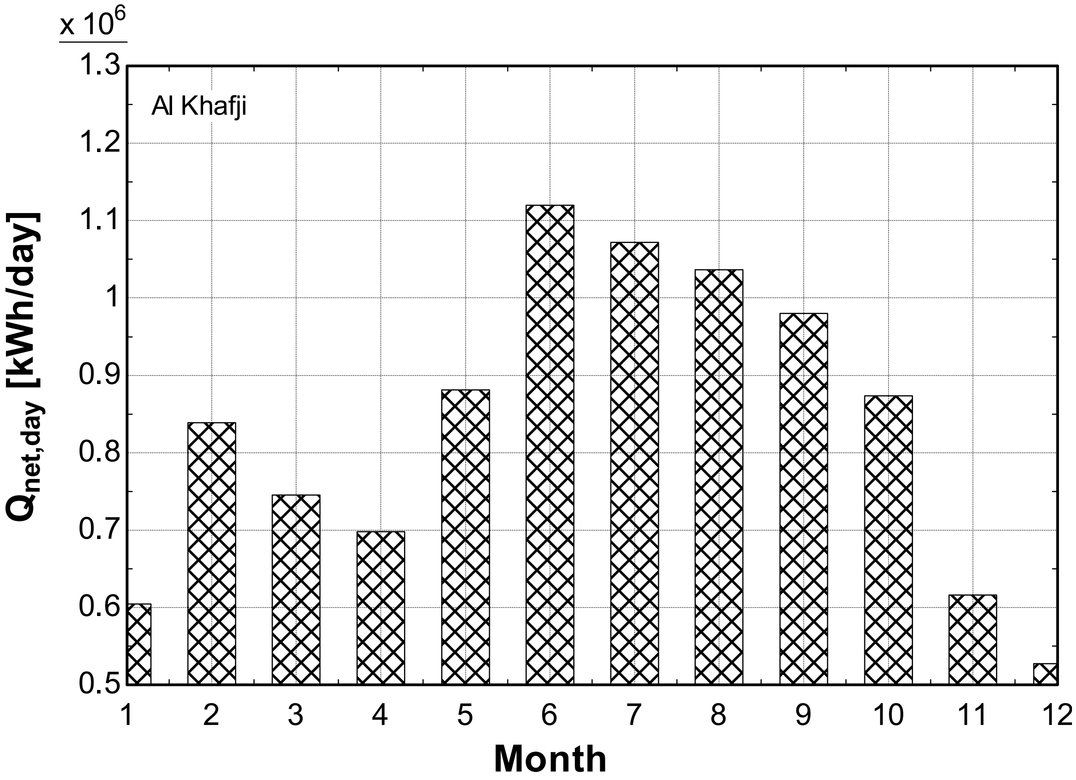

Figure 4.7 Monthly average heat per day collected at the receiver level for Al Khafji, Saudi Arabia

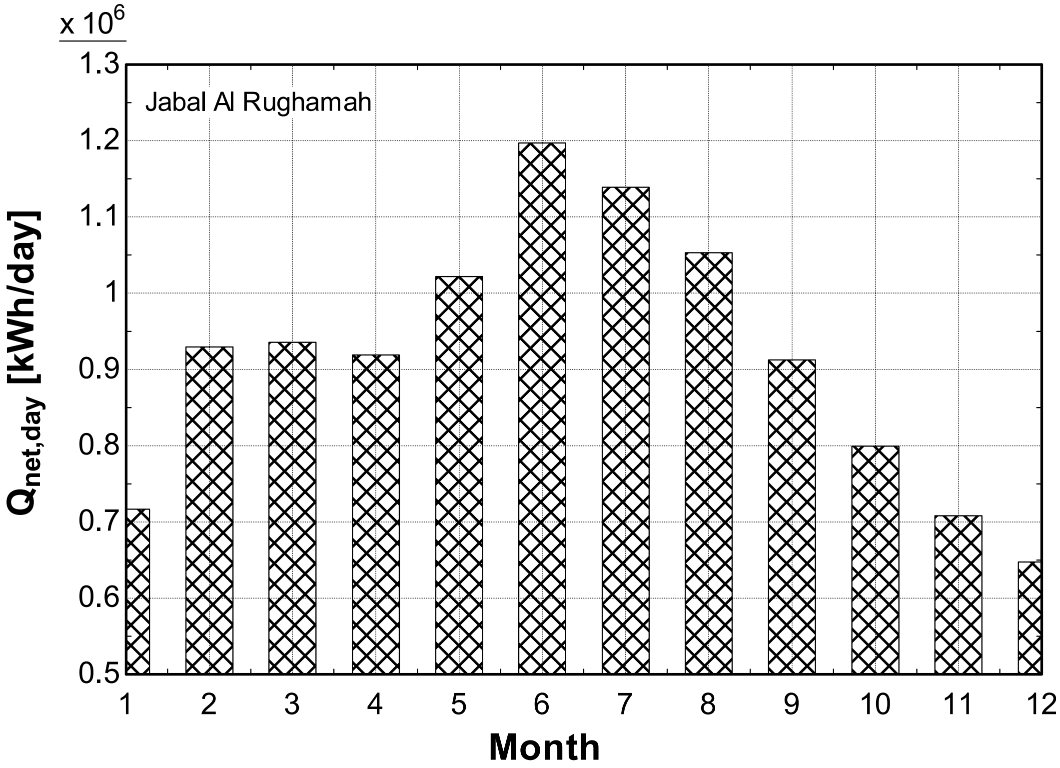

Figure 4.8 Monthly average heat per day collected at the receiver level for Jabal Al-Rughamah, Saudi Arabia

4.2 Two Tank Molten Salt Storage

A transient code is developed and implemented in EES to solve for the temperatures and mass flow rates at hourly instants throughout the day for a two tank molten salt storage. The commonly used mixture of molten salt is that of 60 percent sodium nitrate and 40 percent potassium nitrate [97], thus, it will be utilized in this study. It is also demonstrated in the Solar Two plant in Spain that it has an efficiency of 99 percent, which makes the method a desirable one. The tank storage wall material however, is composed of, 2 cm of alumina lining, 5 cm of SS304 (stainless steel), and 60 cm mineral wool for insulation [98]. Convective losses with the surrounding are calculated at an assumed constant wind velocity of 5 m/s.

For the area of Dhahran, where measured hourly values of direct solar irradiation is available, the change in the mass of molten salt in the hot and cold storage tanks during operation for different average days of the months June, March, and December are illustrated in the graph of Figure 4.9. It could be seen however, that the gap between the curves representing the hot and cold storage molten salt mass is higher for that of the month of June than the other two, and the gap for the month of December is the least. This is due to the higher solar flux in the month of June, which implies that more mass flow rate for charging the energy at the receiver level is required. Also, in all the graphs, it could be seen that the mass of the hot storage tank is decreasing during the time from 1am until 6 or 7am (depends on the month) due to discharging mass to the MEE-TVC and power cycle, and due also to the absence of charging since there is no solar flux at the time. However, from that point forward until reaching 5 or 6 pm (depending on the month), the mass of the hot storage tank increases due to the availability of solar irradiation. After that, the mass of molten salt in the hot storage tank decreases due to the absence of solar flux reaching its initial value. On the contrary, the cold storage tank undergoes the opposite behavior since the total mass of the molten salt is equal to the sum of the molten salt in both tanks.

The storage works in charging mode for all the period of daylight radiation, in other words, molten salt at a temperature of about 420 °C flows from the cold storage tank into the central receiver where it is heated to a temperature of 600 °C. This operation ensures that the temperature entering the hot storage tank is constant; however, the mass flow rate is changing, increasing with the solar flux increase reaching a maximum at solar noon, and decreasing after that. While the charging operation experiences a variation in flow rate, discharging, however, has a constant flow rate flowing from the hot storage tank passing through the heat exchangers, where the energy is released to the sCO_2 power cycle and MEE-TVC desalination. The molten salt is then directed back to the cold storage tank at a lower temperature. The constant mass flow rate is important to ensure a steady operation of the power cycle and the MEE-TVC desalination system. It is worthy of noting that, initially, the total mass of molten salt is divided equally in the hot and cold storage tanks. The total cycle is repeated daily, that is, by the end of a certain day, the mass of the molten salt in each of the tanks goes back to its initial state demonstrated in Figure 4.9. It could be seen that the charging mass flow rate experiences an increase from sunshine at 6 or 7 am and reaches a maximum at noon, then decreases beyond that. This is due to the increase and decrease of solar flux throughout the day, mainly, from the variation of the angle of incidence. It could be also visualized that June experiences the highest mass flow rates while December the lowest, and March coming in between.

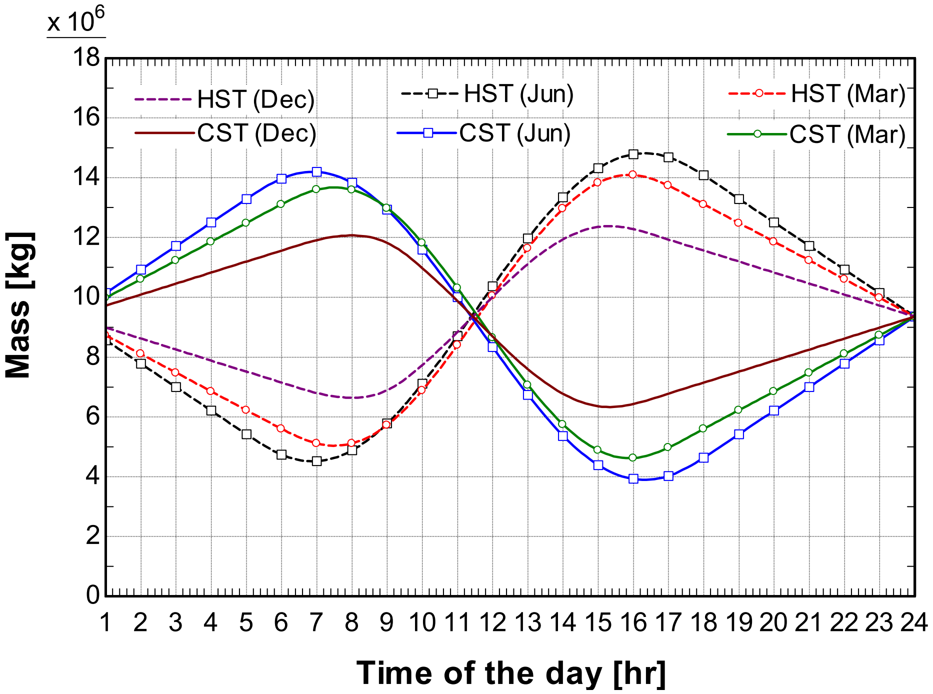

Figure 4.9 Molten salt mass variation in the thermal storage tanks for the whole day on the months of June, March, and December; Dhahran

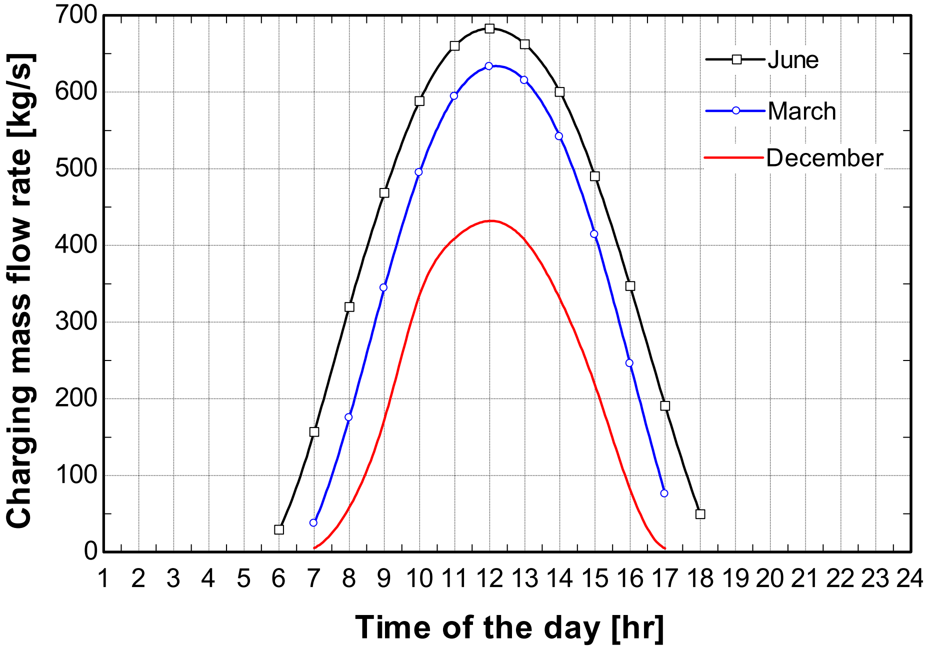

Figure 4.10 Charging mass flow rate variation for the whole day operation for different months of the year, Dhahran

It is essential, however, for the sake of storage sizing and cost analysis later on in this Chapter to evaluate the total salt mass in the two tanks. The total molten salt mass in the storage is evaluated based on the average yearly amount of heat per day collected at the level of the central receiver for each location separately. That is, the charging mass flow rate as previously stated is strongly dependent upon the solar irradiation. The increase in the amount of charging mass needed implies an increase in the total mass of the molten salt. The average yearly heat collected per day for different locations studied and the total mass of the molten salt in the thermal storage tanks are listed in Table 4.4. It could be seen from the table that the amount of molten salt needed for the locations of Yanbu and Khabt Al-Ghusn is relatively higher than the rest, that is, due to the higher collected heat. Jabal Al-Rughamah comes in the second place. Dhahran, Jizan, and Al-Khafji have the least amount of total molten salt required.

Table 4.4 Averaged yearly amount of heat per day collected at the level of the central receiver and total mass of molten salt

Location	$Q_{net,day}$ (kWh/day)	$M_{salt,tot}$ (ton)
Dhahran	827411.8	12,850
Yanbu Al-Nakhil	986783.3	15,320
Jizan	840730.8	13,060
Khabt Al-Ghusn	977689.4	15,180
Al-Khafji	832678.1	12,930
Jabal Al Rughamah	914835.5	14,210

4.3 Supercritical CO_2 Brayton cycles

Given the direct normal irradiance and operating parameters of the solar tower and the type of salt and its mass in the two tank thermal storage in the previous sections, it would be useful to discuss the operating parameters of the sCO_2 cycles involved in the cogeneration systems studied, namely recompression and regeneration cycles. The operating parameters include the turbine inlet temperature and pressure, pressure ratio, recuperator effectiveness, and isentropic efficiencies of the turbine and compressors used. As will be discussed later, the cooler in both cycles are replaced with heat exchangers in the cogeneration system in order to utilize the lost heat from the power cycle to heat the inlet seawater to the multiple effect evaporation desalination system. Table 4.5 contains the operating parameters used in evaluating the performance of the power cycles in the cogeneration schemes.

Table 4.5 Operating parameters of the sCO_2 cycles [25]

Operating Parameter	Value
Temperature at the inlet of compressor (first compressor)	31.25° C
Pressure at the inlet of the compressor (first compressor)	7.4 MPa
Pressure ratio	2.7
High temperature regenerator effectiveness	0.85
Low temperature regenerator effectiveness	0.7
Isentropic efficiencies of the compressors	0.8
Isentropic efficiencies of the turbines	0.9

The effectiveness of the recuperators and isentropic efficiencies of the compressors and turbine are found in [25].

4.4 MEE-TVC Desalination System

The MEE-TVC operating parameters are given in Table 4.6. The desalination system is studied for different number of effects for parametric studies.

Table 4.6 Operating parameters of the MEE-TVC system [31]

N	Temperature (^oC)			Steam Jet Ejector
	T [1]	T [n]	ΔT	CR
4	55.8	46.7	3.03	1.81
5	55.8	46.1	2.42	1.81
6	55.8	44.3	2.3	1.98
7	56.4	42.8	2.26	2.2
8	58.8	42.8	2.28	2.46
9	60.9	42.8	2.26	2.7
10	63.3	42.8	2.27	3.01
11	65.4	42.8	2.26	3.31
12	67.8	42.8	2.27	3.68

The input parameters are tabulated and present in Table 4.7. These include the feed seawater salinity and temperature, the motive steam pressure, and the cooling seawater temperature.

Table 4.7 Input parameters of the MEE-TVC system [31]

MEE-TVC Input Parameter	Value
Cooling seawater temperature	24° C
Feed seawater temperature	40° C
Feed seawater salinity	36000 ppm
Motive steam pressure	2500 kPa
Specific Pumping Electrical Consumption	1.5 kWh/m^3

The MEE-TVC system is a thermal desalination system; therefore, it utilizes heat to produce water. However, it should be noted that electrical energy is needed for brine, feed, and distillate pumping. Although the pumping energy required is less than MSF (2.5 – 4 kWh/m^3) and reverse osmosis (5 – 8 kWh/m^3), it is still significant to address it in the current study. In Literature, the electrical pumping energy required for desalination systems is found as values of energy per metric cube of distillate. To the author's best knowledge, the pumping energy requirement is not modeled in a way that makes it dependent on the system design. Rather, it is given a single value for each case, based on industrial practices. The values reported in the literature for MEE and MEE-TVC systems range between 1.2 kWh/m^3 and 2.2 kWh/m^3 [99]–[109]. The average however tends to vary closely in the range of 1.5 kWh/m^3, and therefore, the value will be adopted in this study as shown in Table 4.7.

4.5 Solar Cogeneration system

Figure 4.11 through Figure 4.28 represent the average power and water production for different months of the year corresponding to the six regions of Saudi Arabia and fractions of 0.5, 0.7, and 0.9. These results represent those for the cogeneration system utilizing the regenerative cycle. Figure 4.29 through Figure 4.46 represent similar results for the cogeneration system utilizing the recompressive cycle. From the graphs representing different fractions for the same cogeneration system and the same region, it can be seen that the power production increases on the expense of the decrease in the water production for increasing fractions. Hence, for higher fractions, more power is generated and less water is produced. This result is justifiable in a sense that it goes hand in hand with the definition of the fraction, which is, the percentage of input heat from total accounted for the power cycle. Furthermore, the results for the region of Dhahran, Jabal Al-Rughamah, and Al-Khafji are shown to have an increasing production of power and water reaching a maximum at the month of June (summer season). However, Jabal Al-Rughamah and Al-Khafji regions experience a decrease in the months of March and April, which is slight for Jabal Al-Rughamah region, but is shown clearly for Al-Khafji. Yanbu follows the same trend as the regions mentioned earlier with a slight decrease in production for the months of April and May. Moreover, the regions of Khabt Al-Ghusn can be best described by a somewhat uniform pattern for all the months with slight increase and decrease at the beginning and the end of the year respectively. The city of Jizan experiences an increase at the beginning of the year, with local maximum uniform pattern for the month of March, April, and May. The production then decreases to a minimum for the month of August, after which an increase is encountered reaching a maximum for the month of October, and decreasing afterwards. The difference between the regeneration cogeneration cycle and the recompression cogeneration cycle is that the latter results in slightly higher power production for similar regions and fractions, which is due to the higher efficiency of the recompression cycle compared to the regeneration one. The results for monthly power and water production for the different regions and fractions are summarized in Table 4.8 and Table 4.9 for the regeneration and recompression cogeneration cycles respectively.

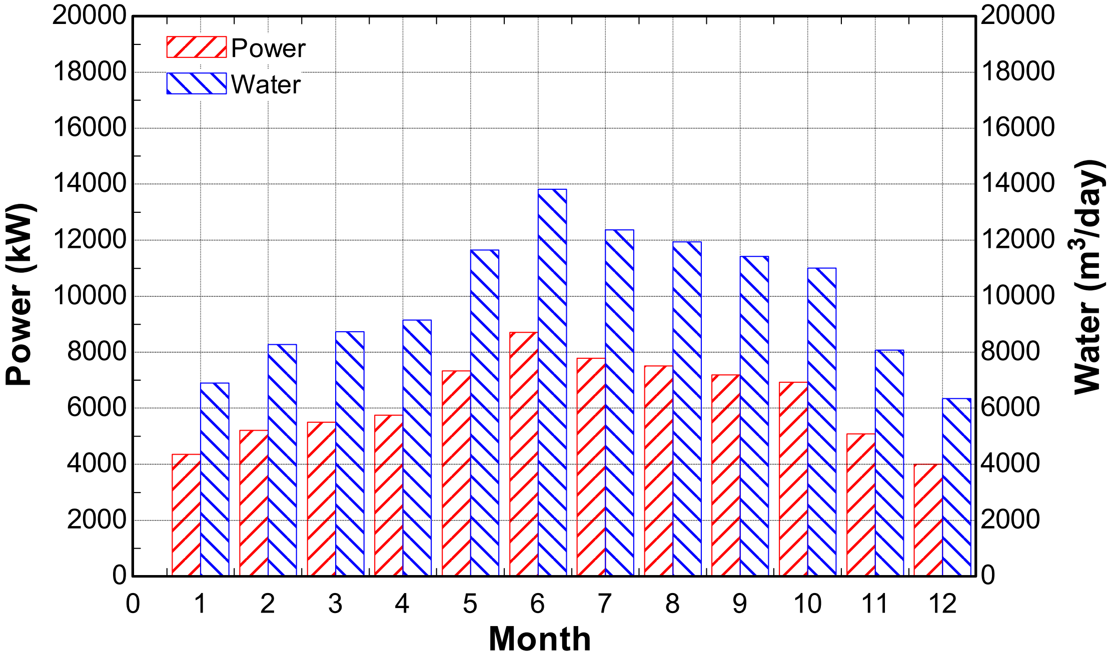

Figure 4.11 Average monthly power and water production for the region of Dahran, regenerative, f=0.5, n=12

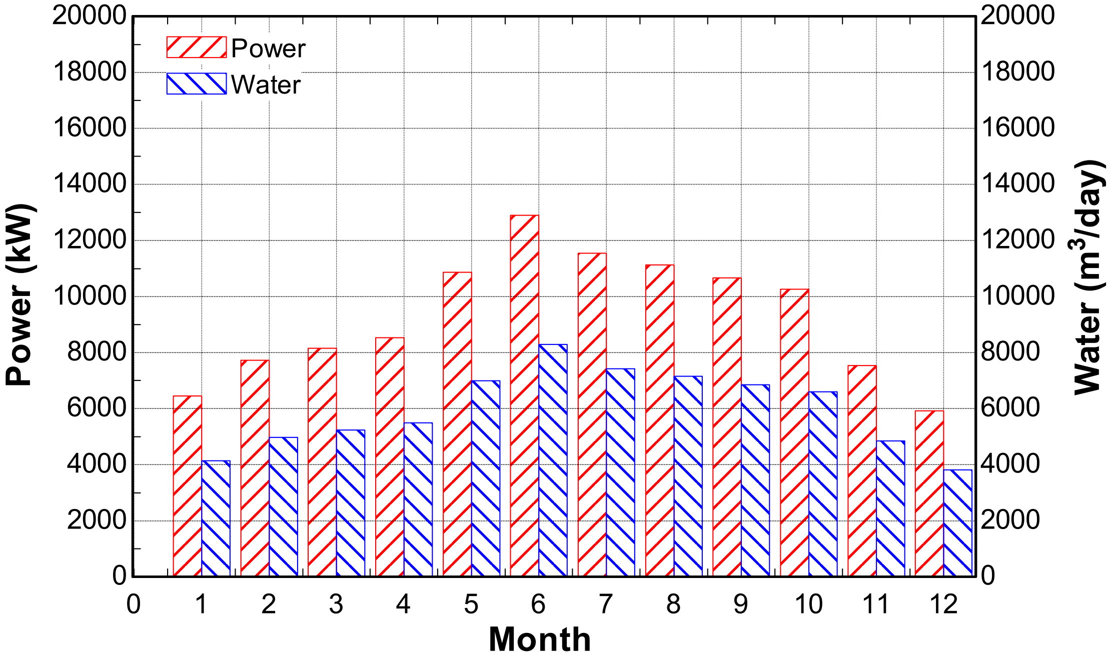

Figure 4.12 Average monthly power and water production for the region of Dahran, regenerative, f=0.7, n=12

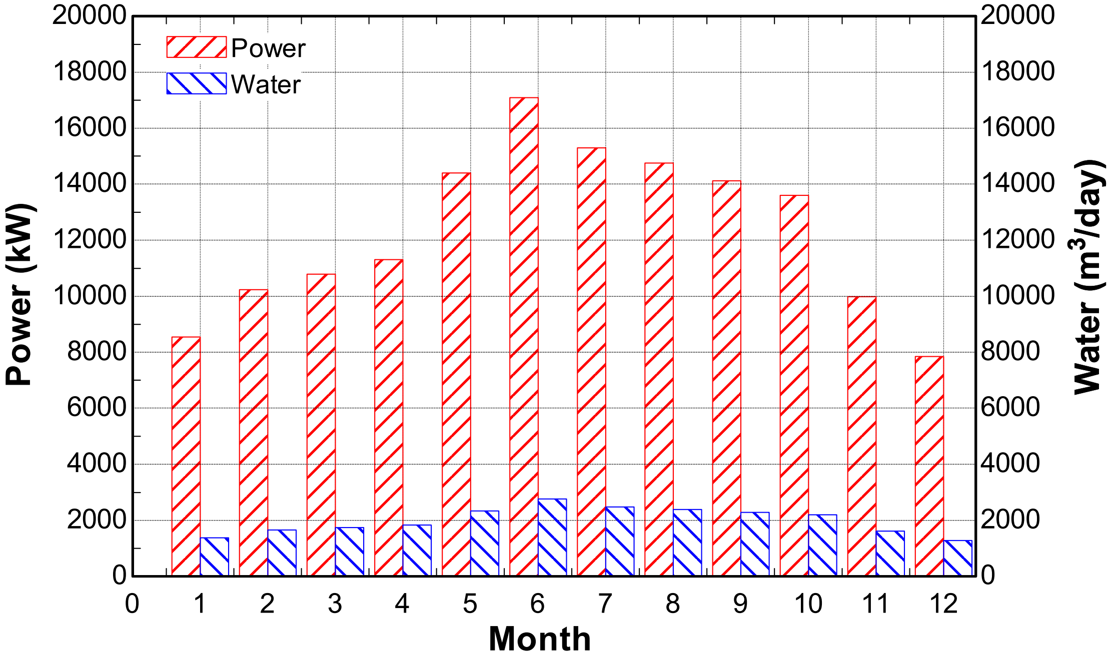

Figure 4.13 Average monthly power and water production for the region of Dahran, regenerative, f=0.9, n=12

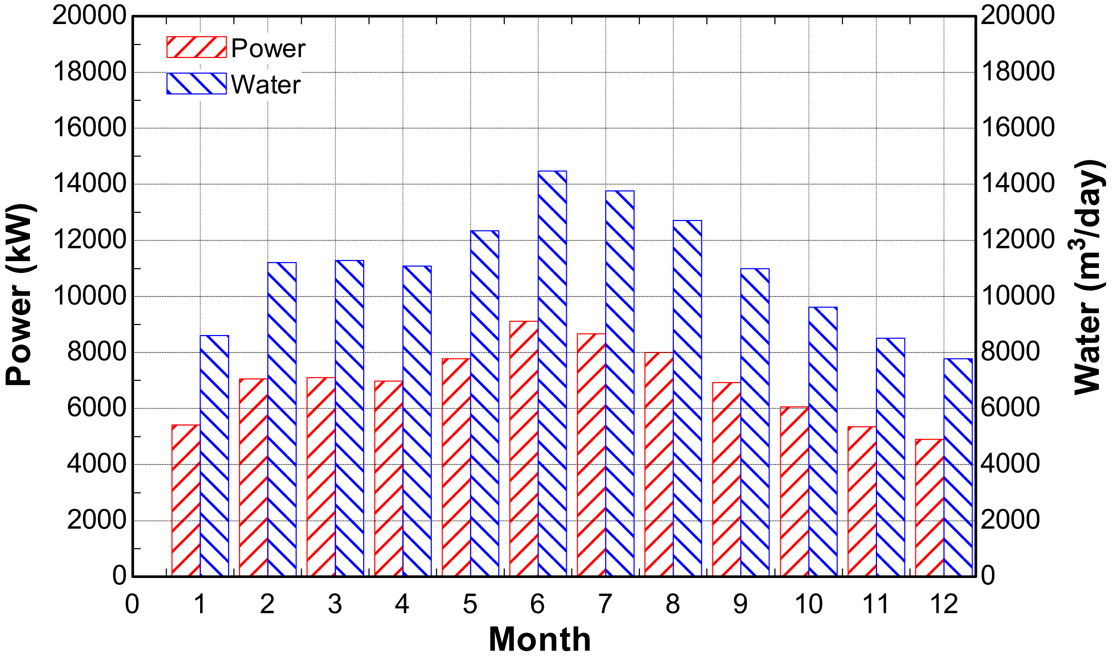

Figure 4.14 Average monthly power and water production for the region of Jabal Al Rughamah, regenerative, f=0.5, n=12

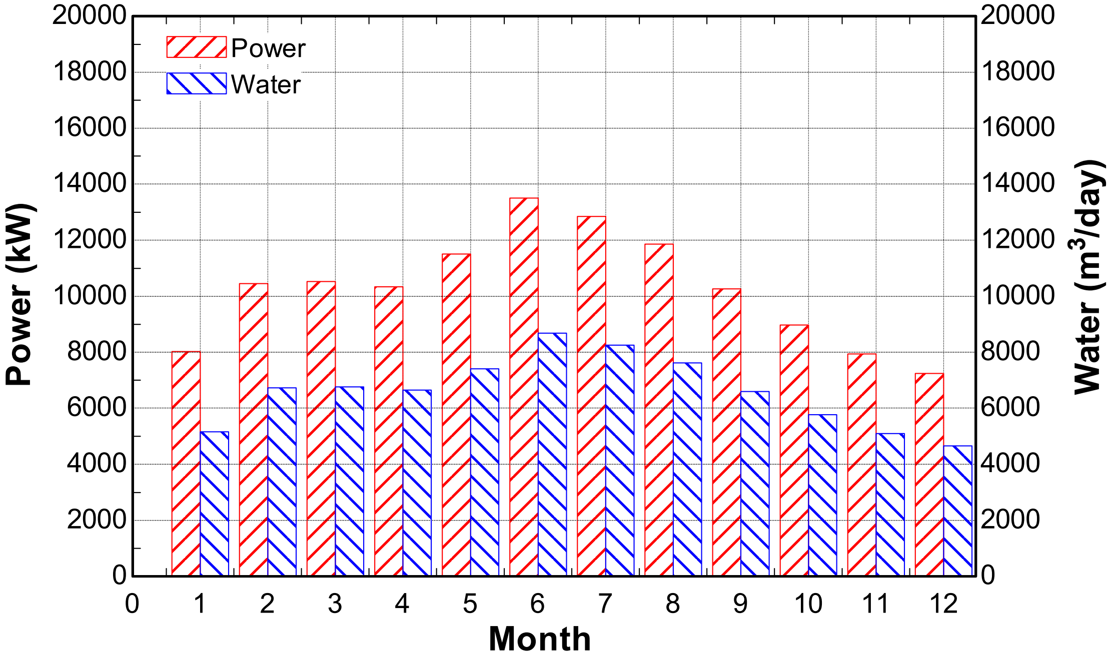

Figure 4.15 Average monthly power and water production for the region of Jabal Al Rughamah, regenerative, f=0.7, n=12

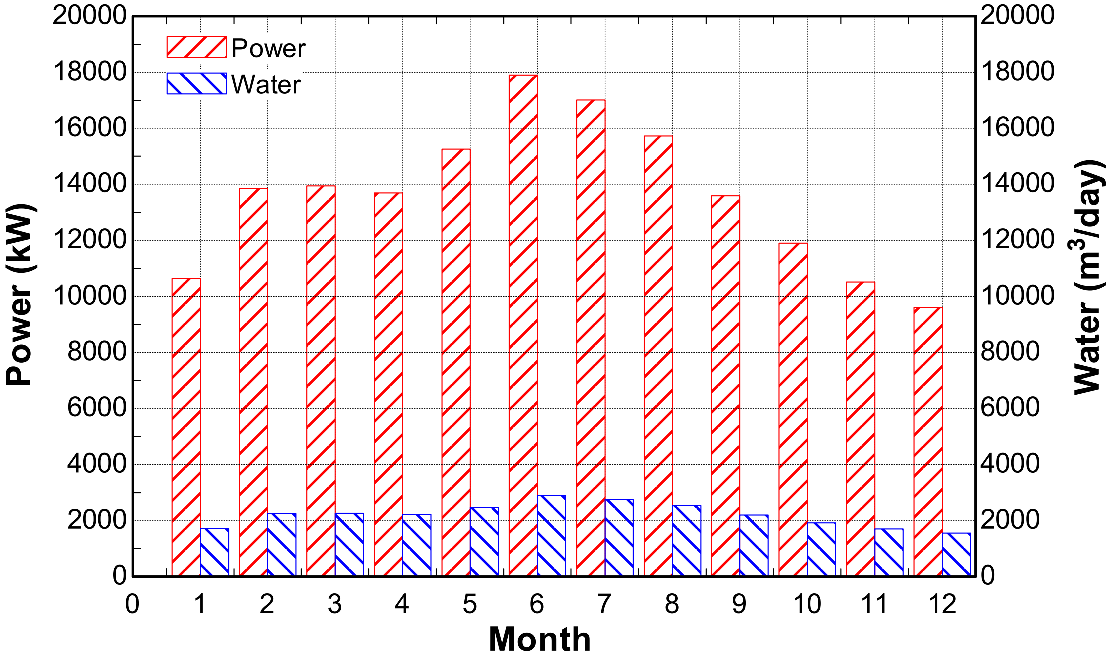

Figure 4.16 Average monthly power and water production for the region of Jabal Al Rughamah, regenerative, f=0.9, n=12

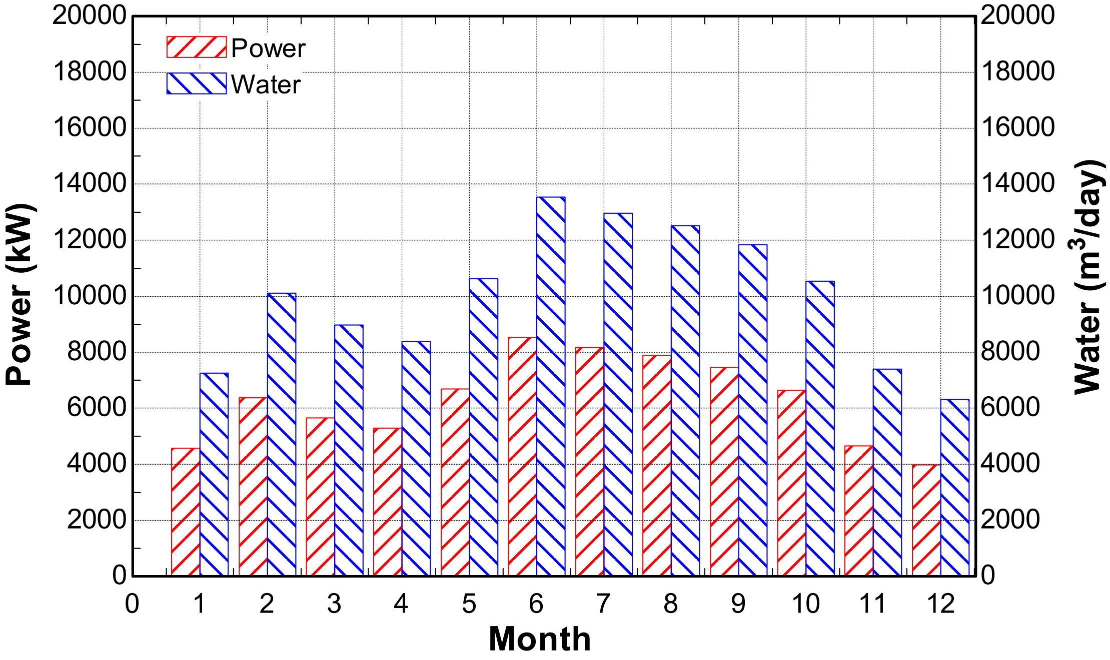

Figure 4.17 Average monthly power and water production for the region of Al-Khafji, regenerative, f=0.5, n=12

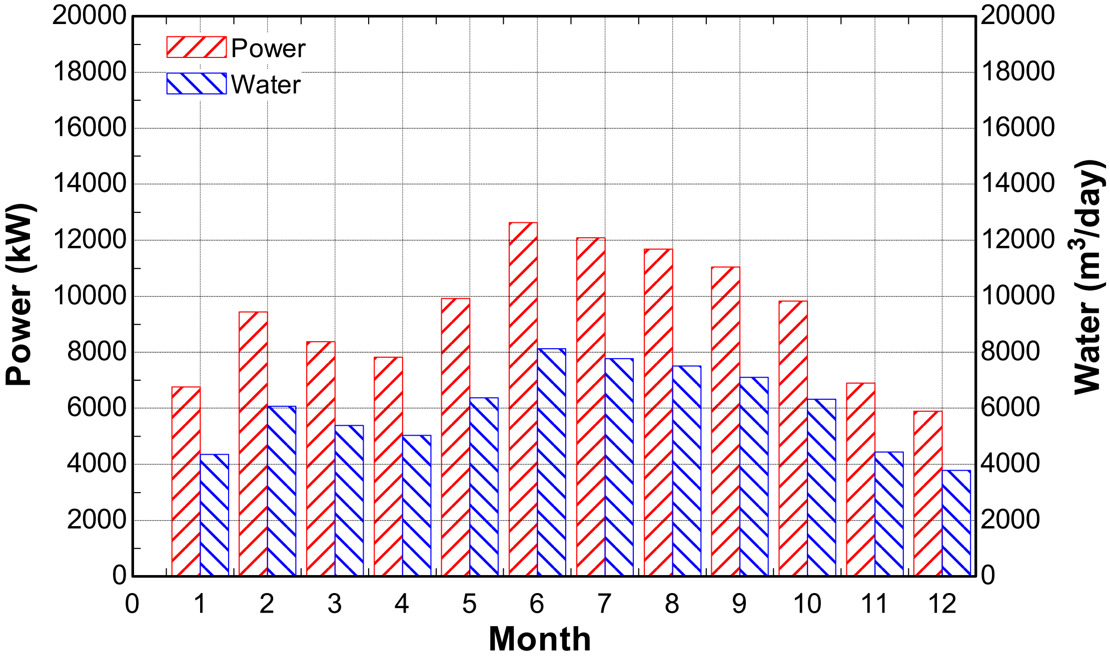

Figure 4.18 Average monthly power and water production for the region of Al-Khafji, regenerative, f=0.7, n=12

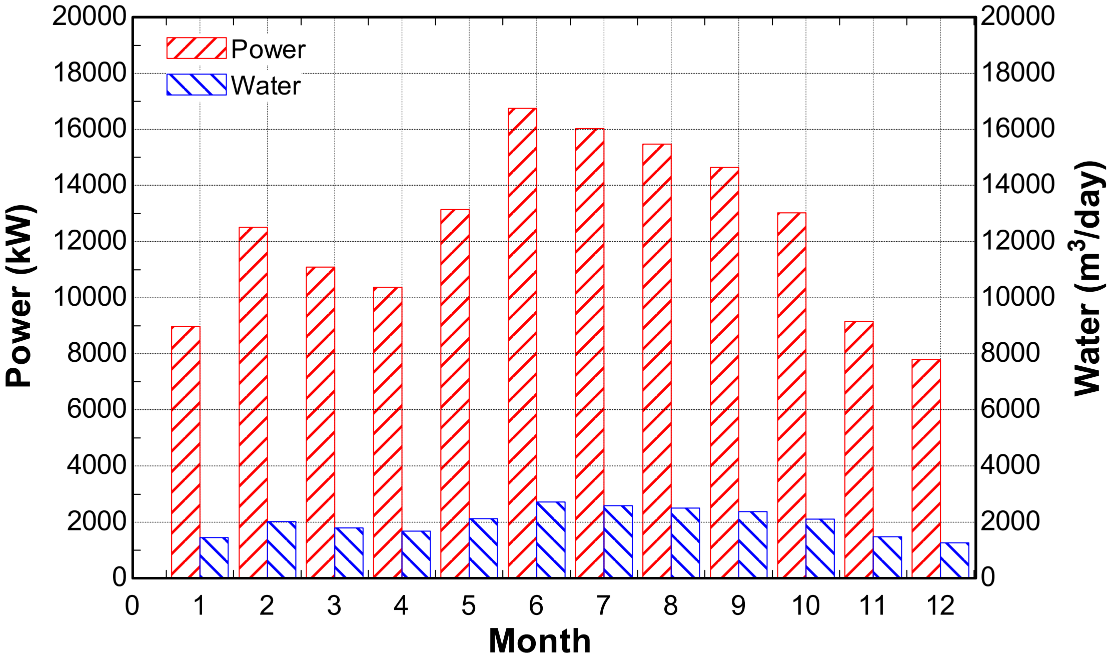

Figure 4.19 Average monthly power and water production for the region of Al-Khafji, regenerative, f=0.9, n=12

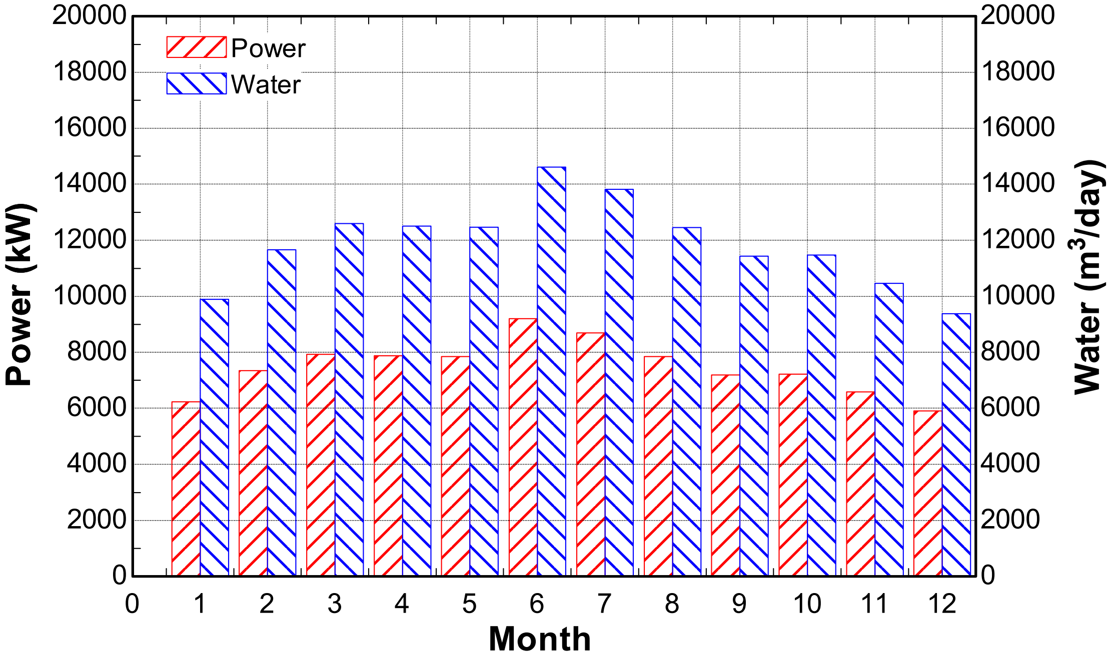

Figure 4.20 Average monthly power and water production for the region of Yanbu, regenerative, f=0.5, n=12

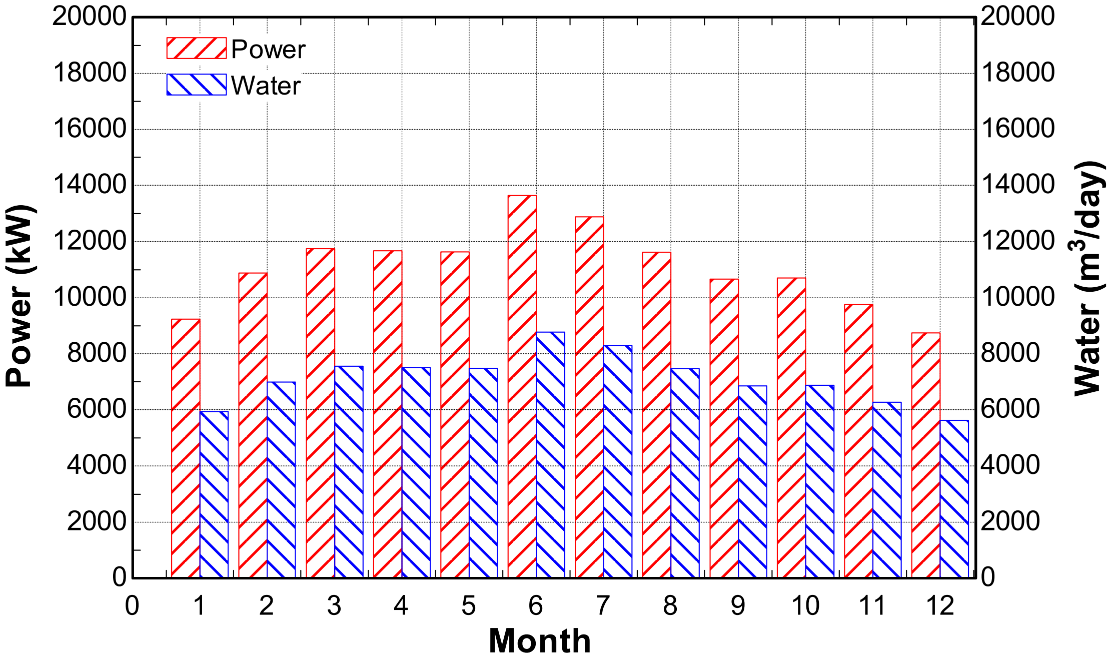

Figure 4.21 Average monthly power and water production for the region of Yanbu, regenerative, f=0.7, n=12

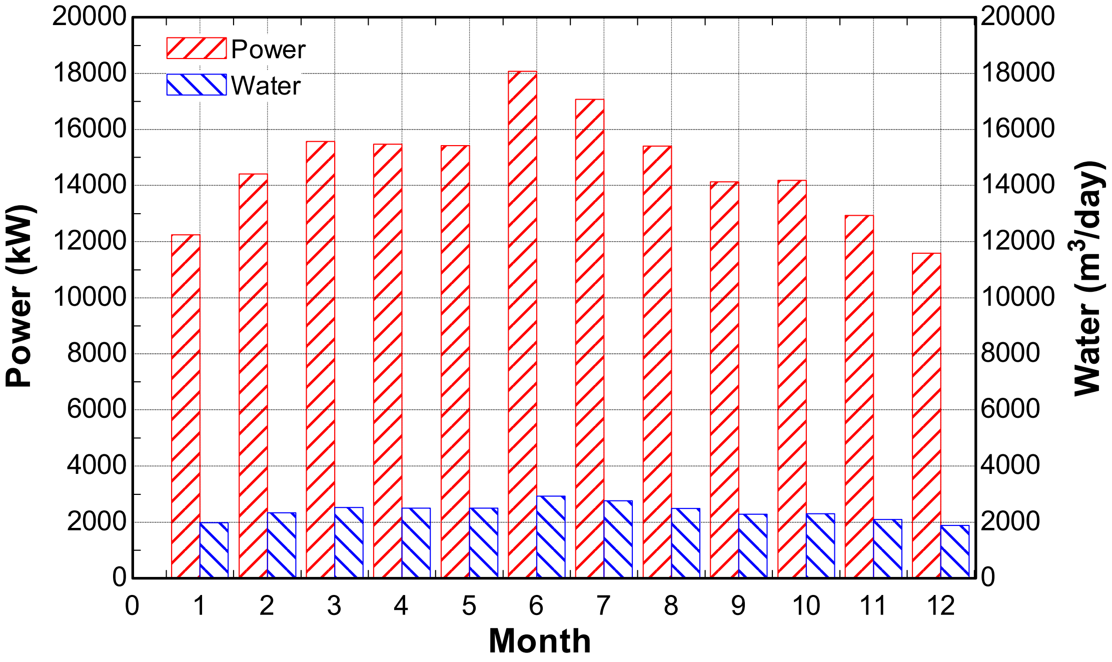

Figure 4.22 Average monthly power and water production for the region of Yanbu, regenerative, f=0.9, n=12

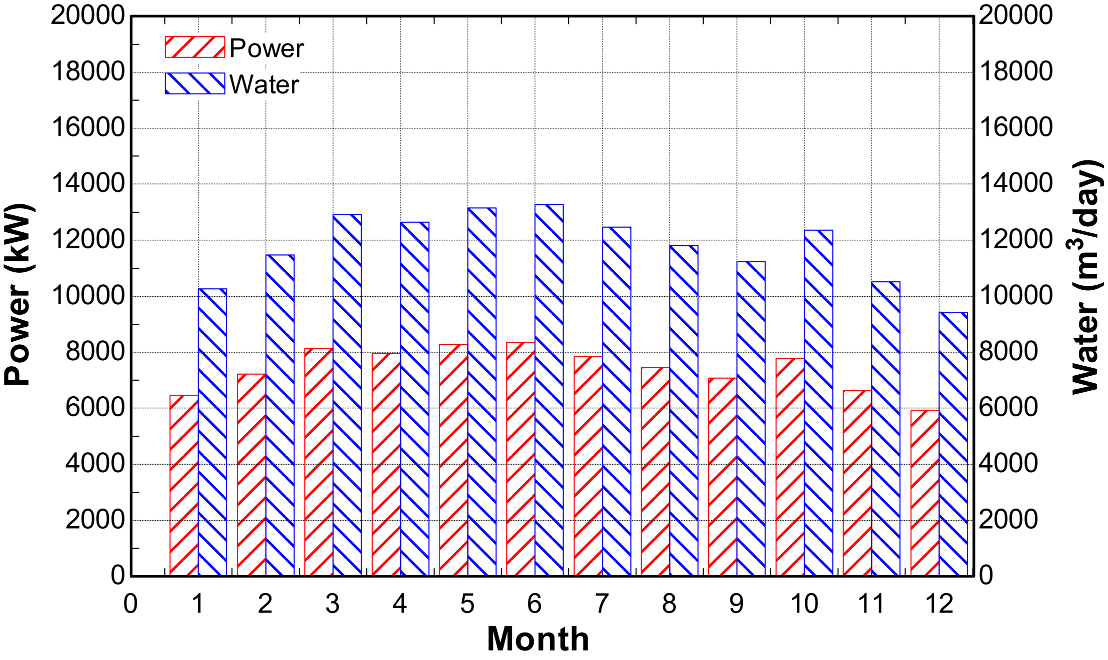

Figure 4.23 Average monthly power and water production for the region of Khabt Al-Ghusn, regenerative, f=0.5, n=12

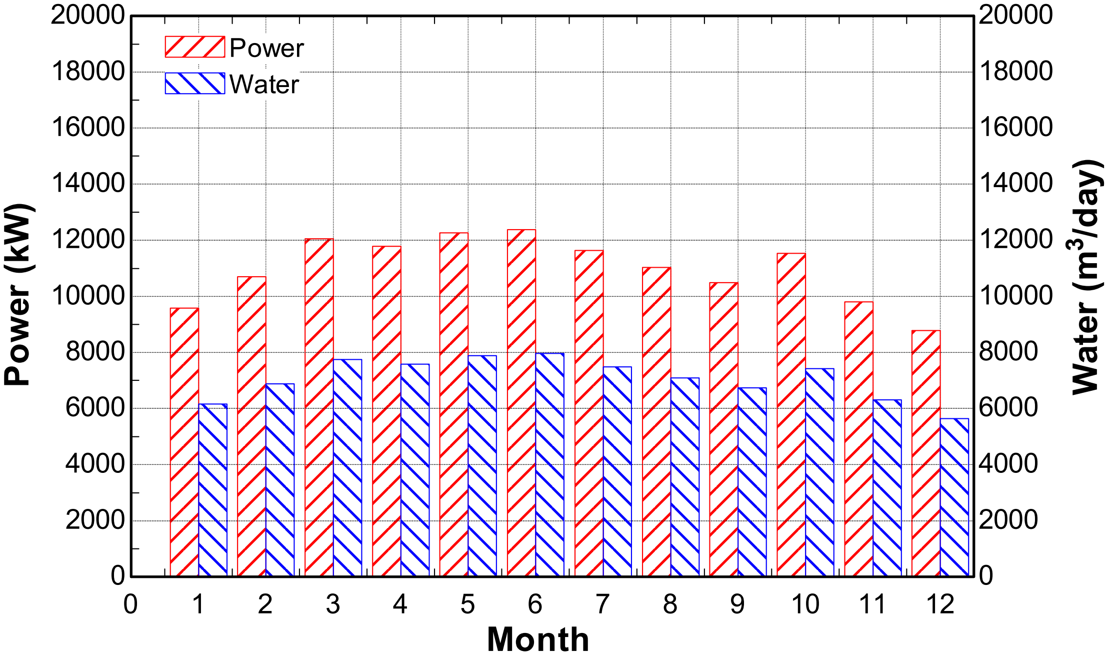

Figure 4.24 Average monthly power and water production for the region of Khabt Al-Ghusn, regenerative, f=0.7, n=12

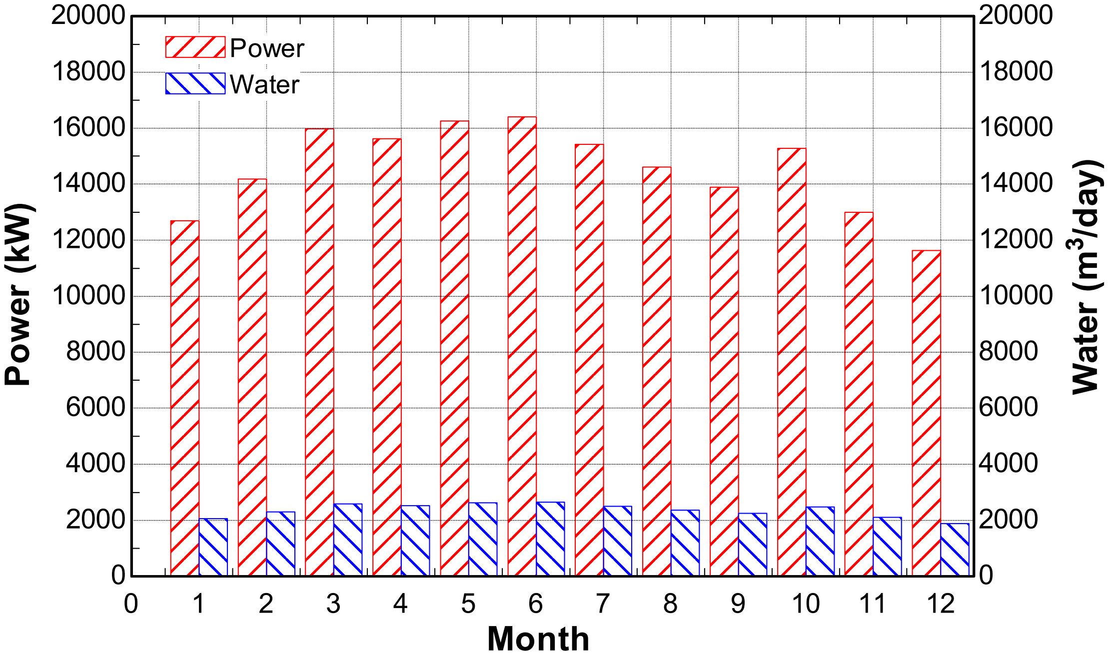

Figure 4.25 Average monthly power and water production for the region of Khabt Al-Ghusn, regenerative, f=0.9, n=12

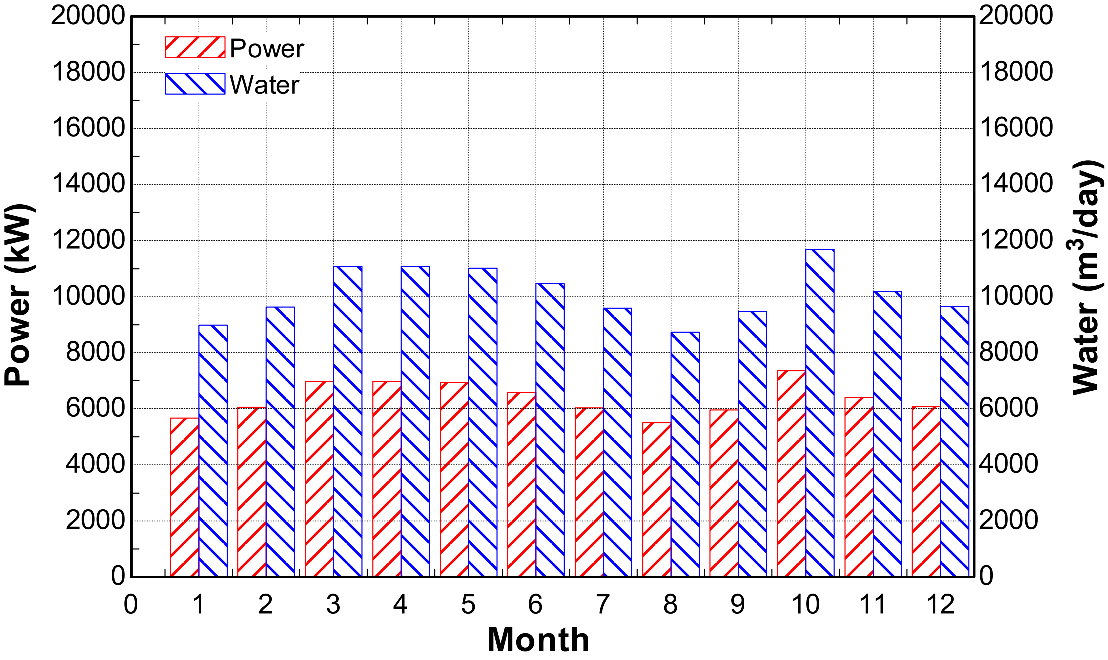

Figure 4.26 Average monthly power and water production for the region of Jizan, regenerative, f=0.5, n=12

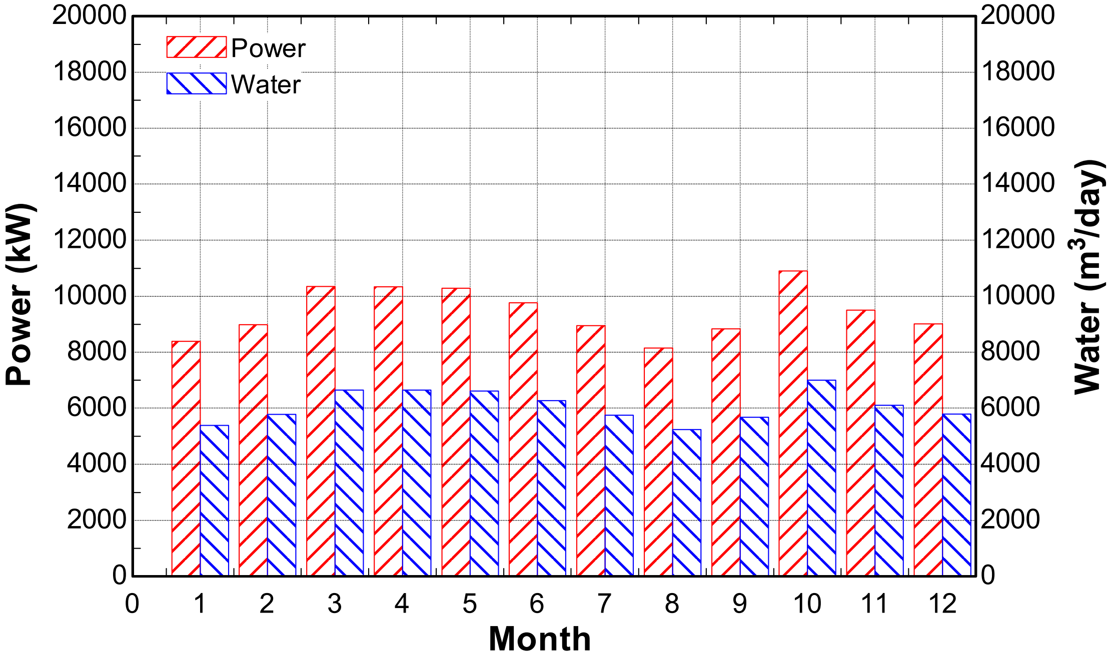

Figure 4.27 Average monthly power and water production for the region of Jizan, regenerative, f=0.7, n=12

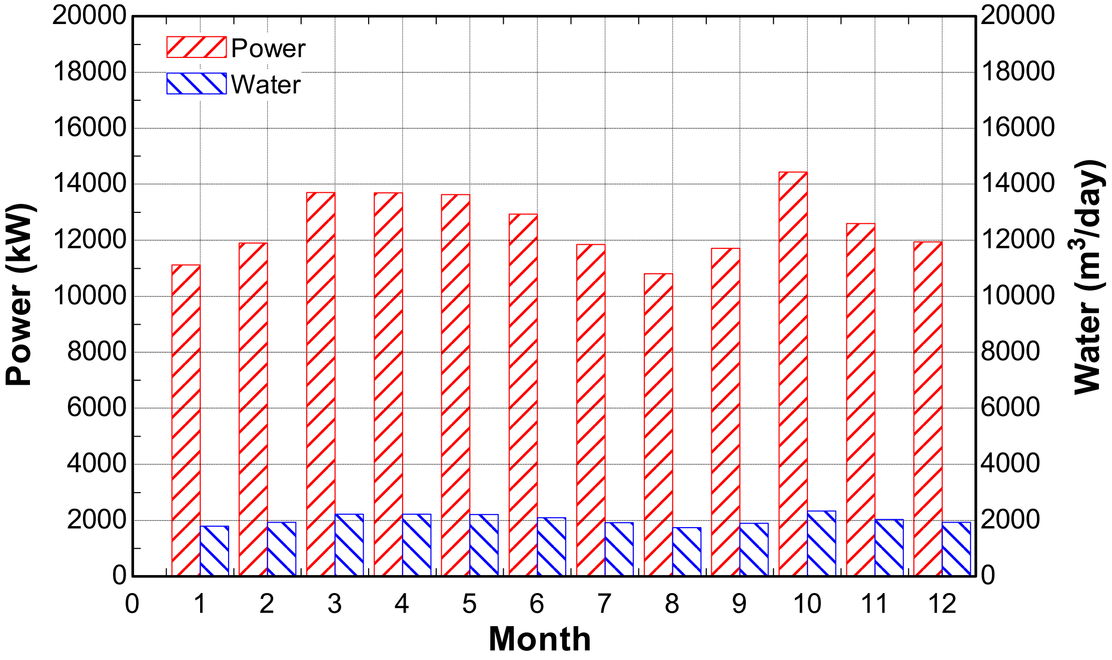

Figure 4.28 Average monthly power and water production for the region of Jizan, regenerative, f=0.9, n=12

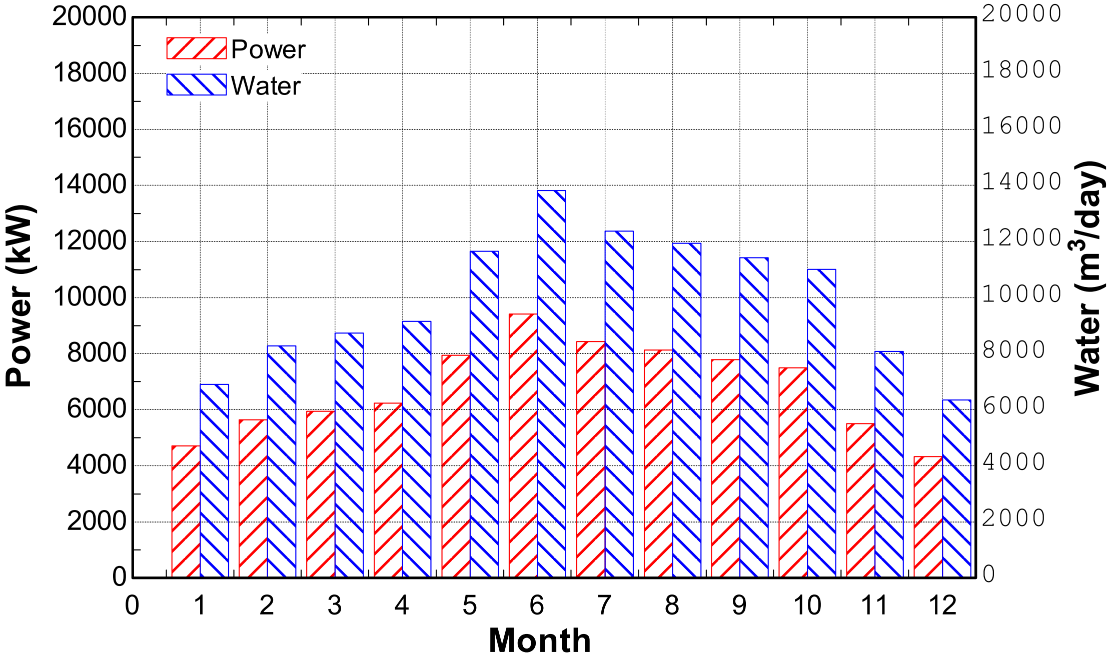

Figure 4.29 Average monthly power and water production for the region of Dahran, recompressive, f=0.5, n=12

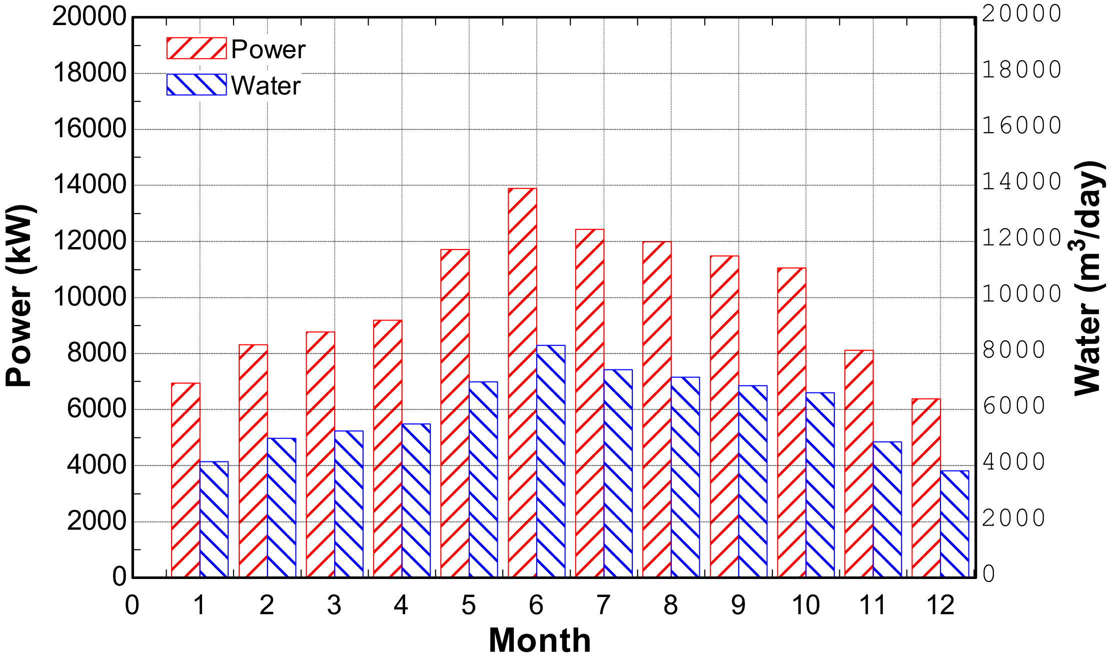

Figure 4.30 Average monthly power and water production for the region of Dahran, recompressive, f=0.7, n=12

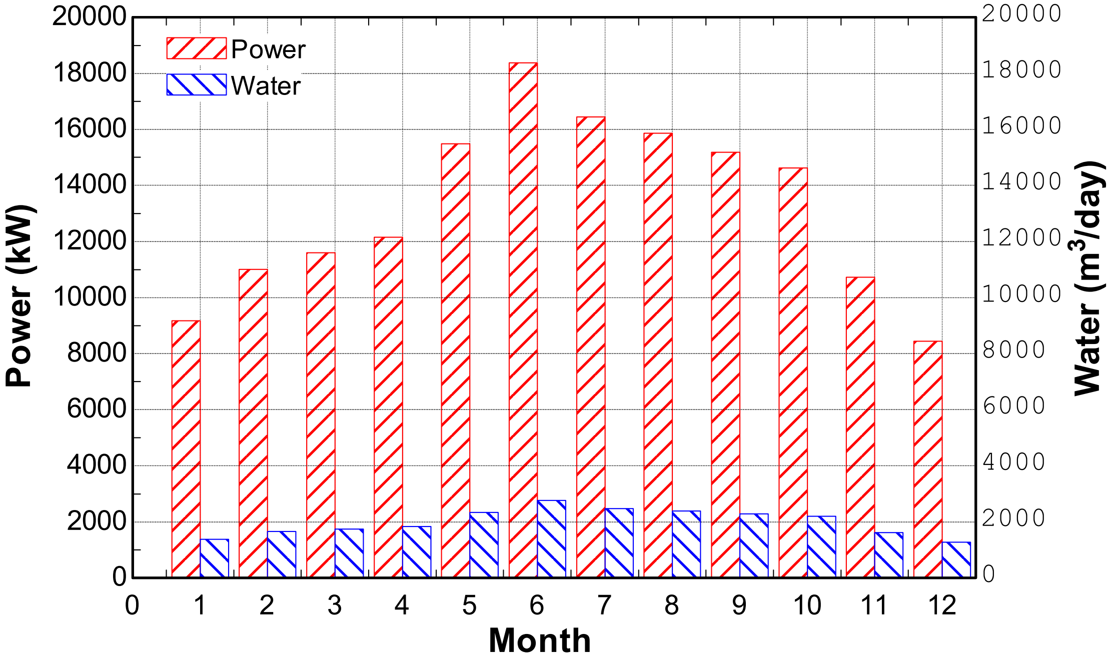

Figure 4.31 Average monthly power and water production for the region of Dahran, recompressive, f=0.9, n=12

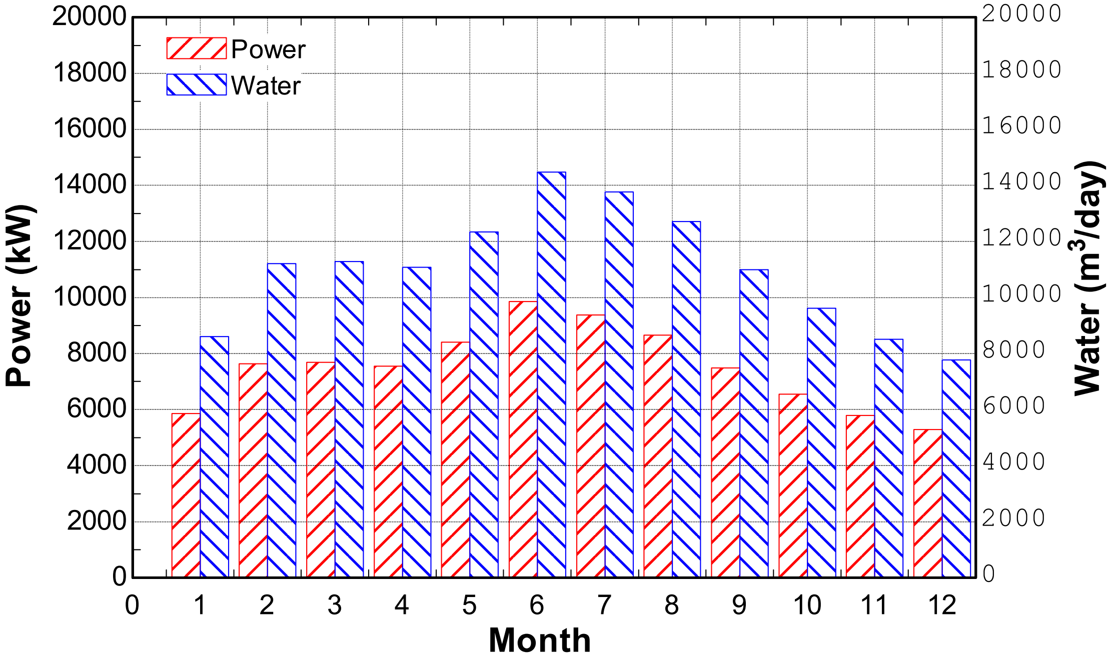

Figure 4.32 Average monthly power and water production for the region of Jabal Al-Rughamah, recompressive, f=0.5, n=12

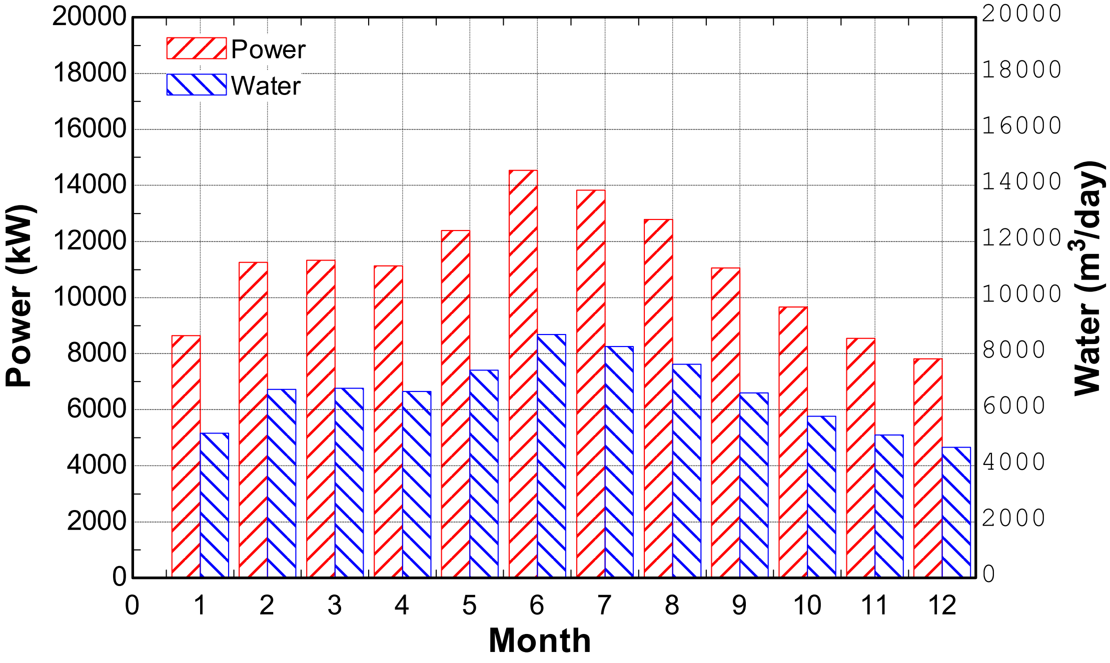

Figure 4.33 Average monthly power and water production for the region of Jabal Al-Rughamah, recompressive, f=0.7, n=12

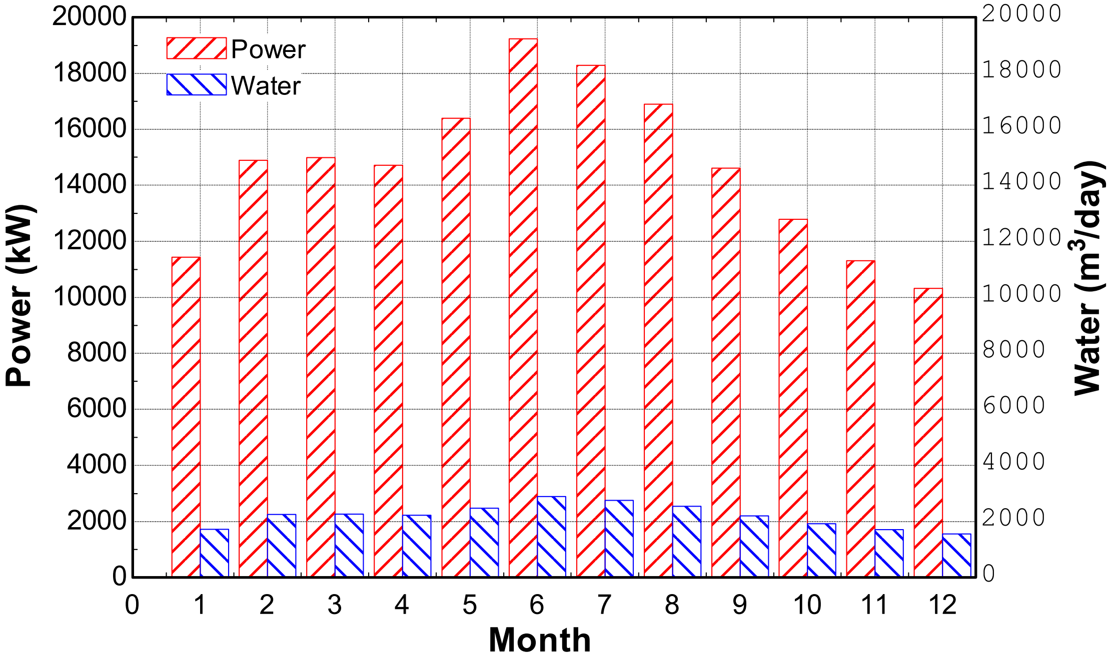

Figure 4.34 Average monthly power and water production for the region of Jabal Al-Rughamah, recompressive, f=0.9, n=12

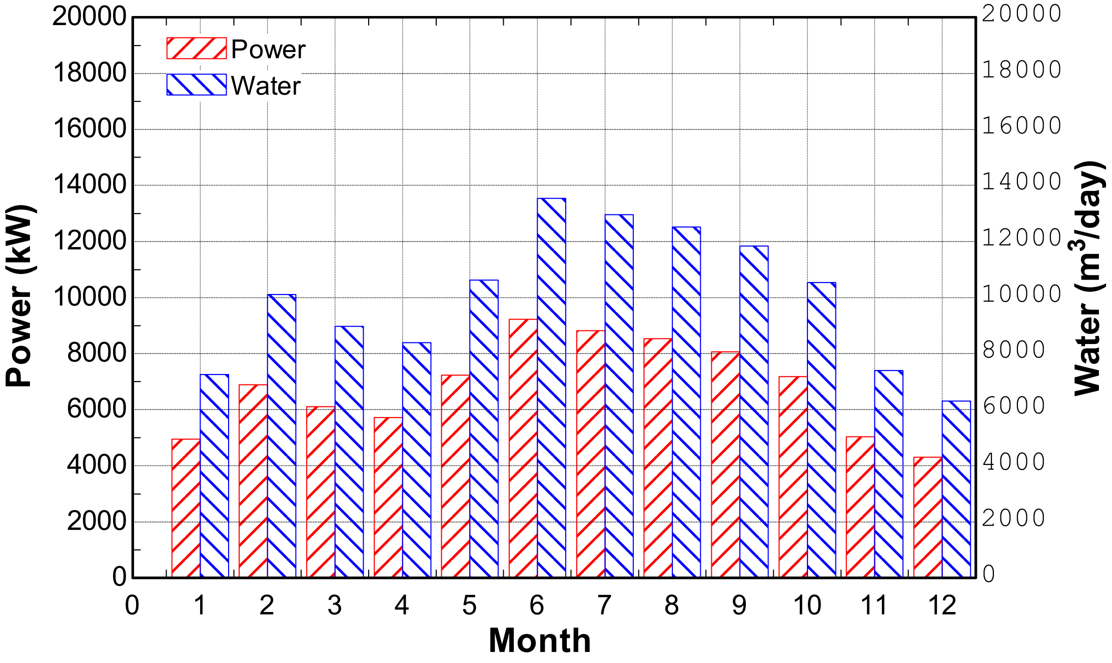

Figure 4.35 Average monthly power and water production for the region of Al-Khafji, recompressive, f=0.5, n=12

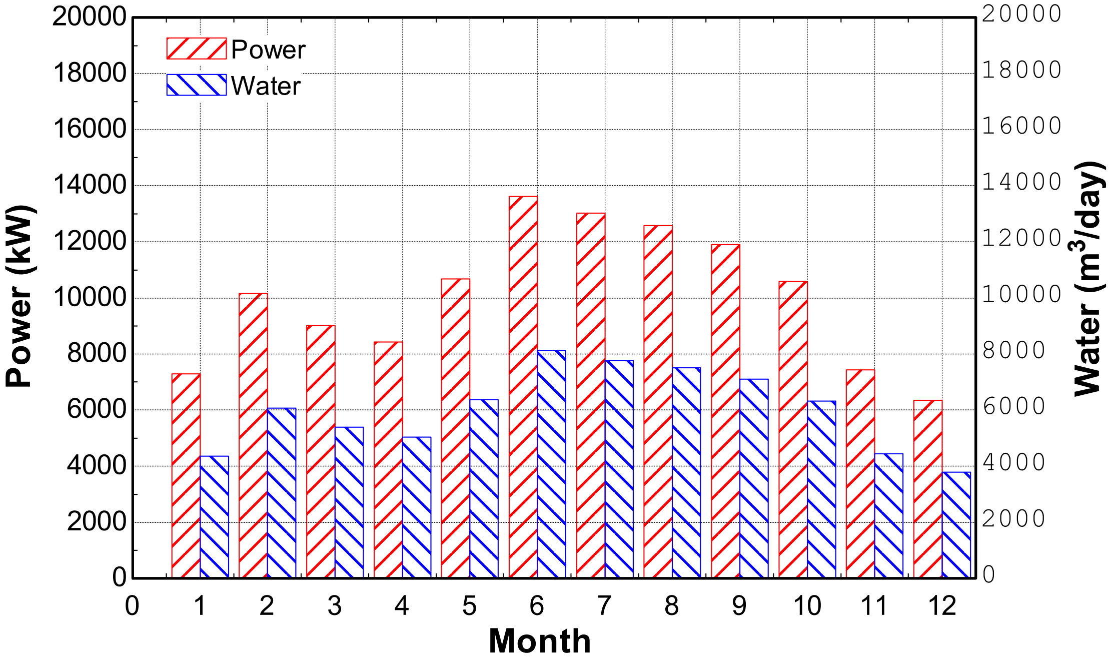

Figure 4.36 Average monthly power and water production for the region of Al-Khafji, recompressive, f=0.7, n=12

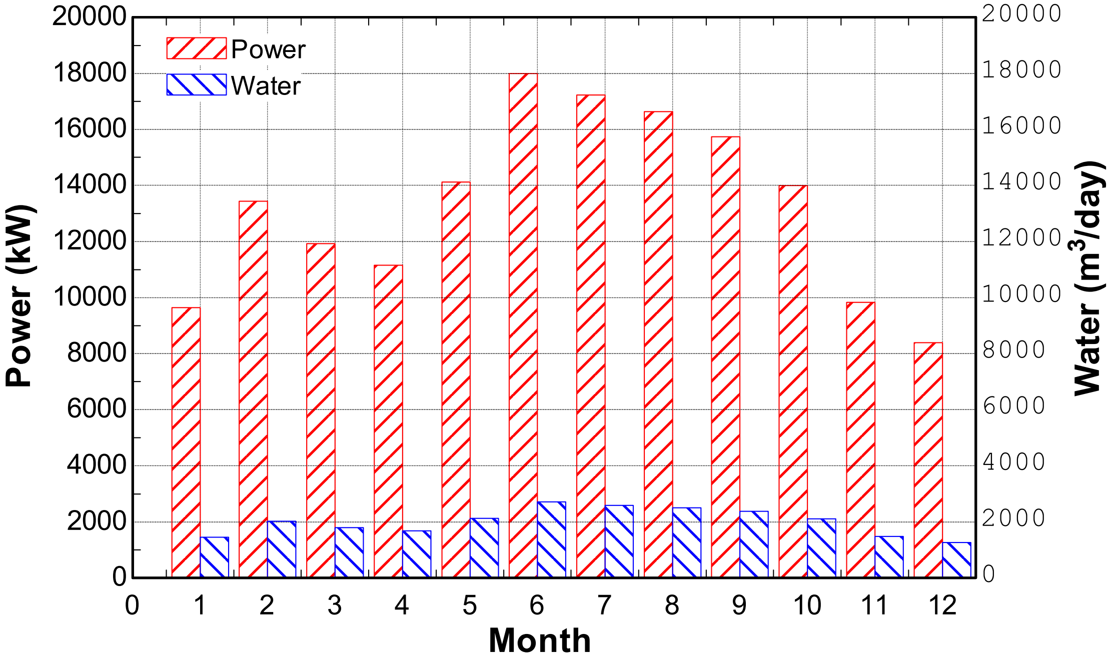

Figure 4.37 Average monthly power and water production for the region of Al-Khafji, recompressive, f=0.9, n=12

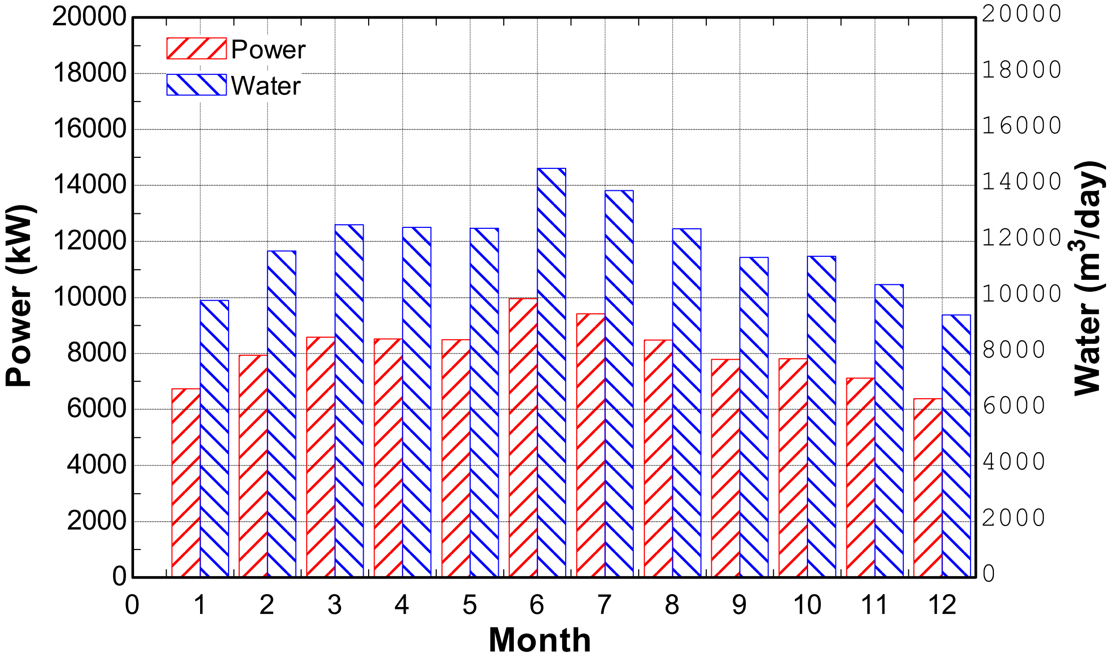

Figure 4.38 Average monthly power and water production for the region of Yanbu, recompressive, f=0.5, n=12

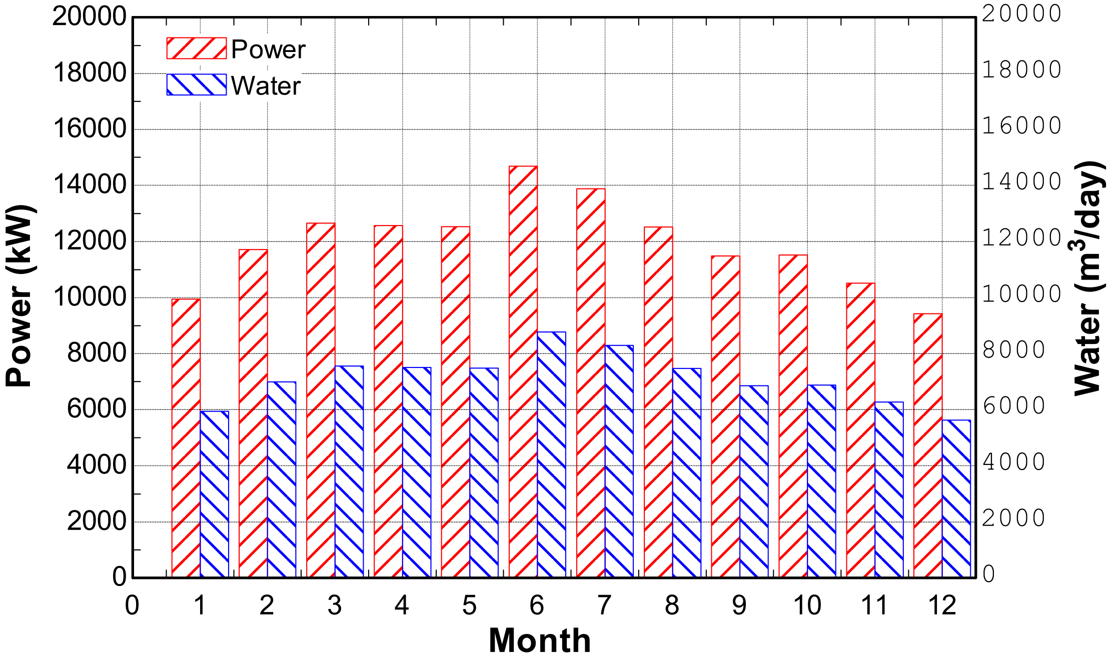

Figure 4.39 Average monthly power and water production for the region of Yanbu, recompressive, f=0.7, n=12

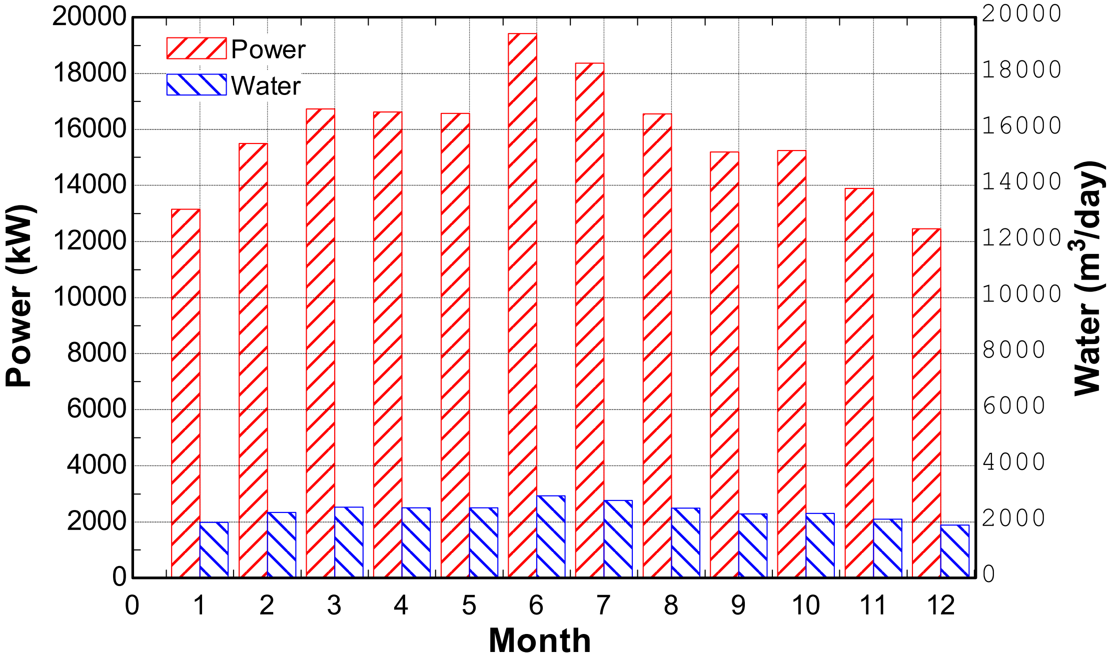

Figure 4.40 Average monthly power and water production for the region of Yanbu, recompressive, f=0.9, n=12

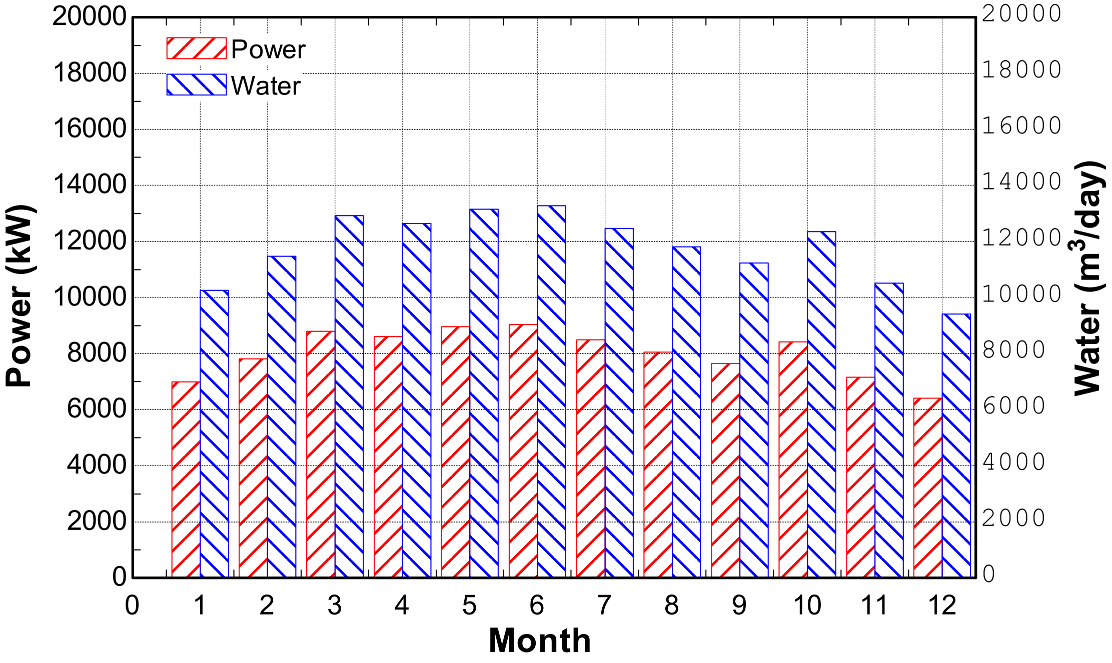

Figure 4.41 Average monthly power and water production for the region of Khabt Al Ghusn, recompressive, f=0.5, n=12

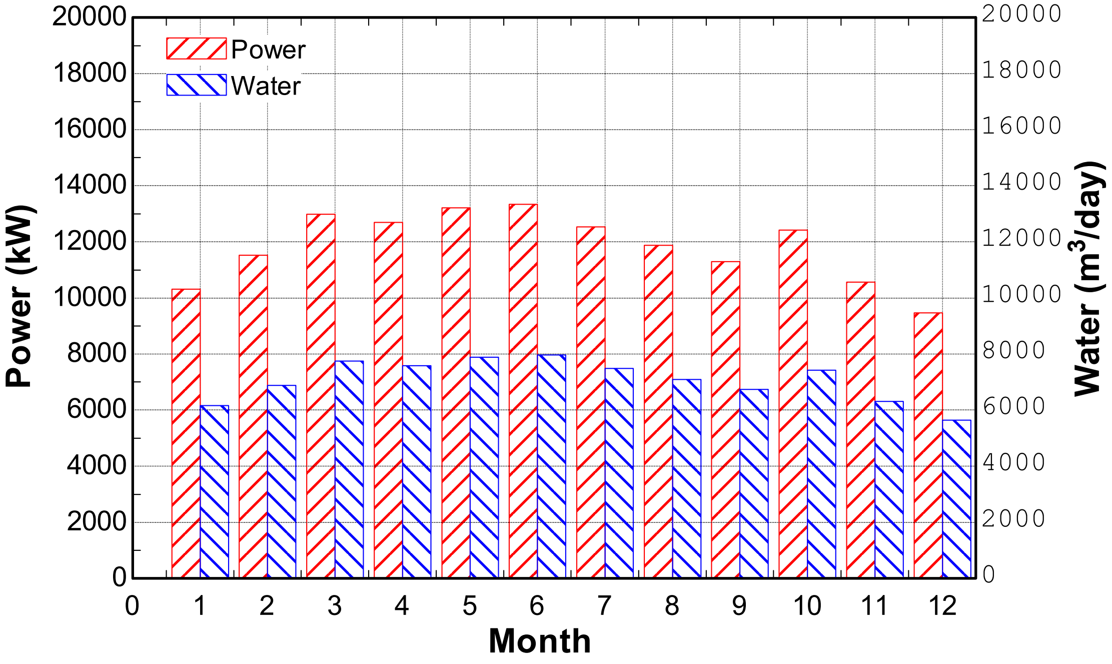

Figure 4.42 Average monthly power and water production for the region of Khabt Al Ghusn, recompressive, f=0.7, n=12

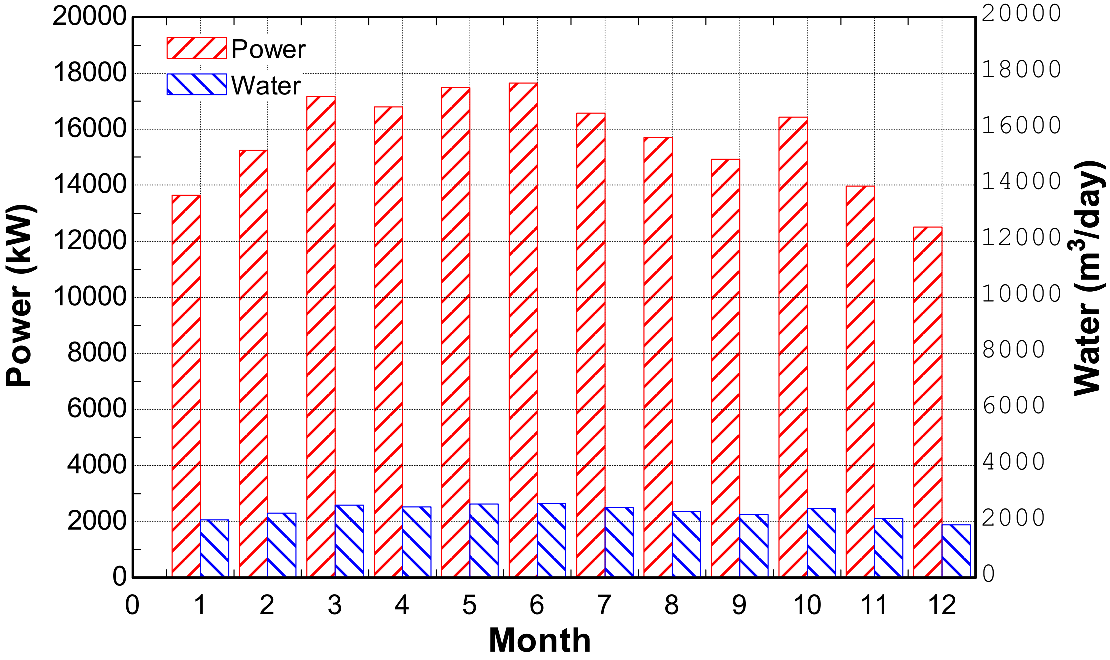

Figure 4.43 Average monthly power and water production for the region of Khabt Al Ghusn, recompressive, f=0.9, n=12

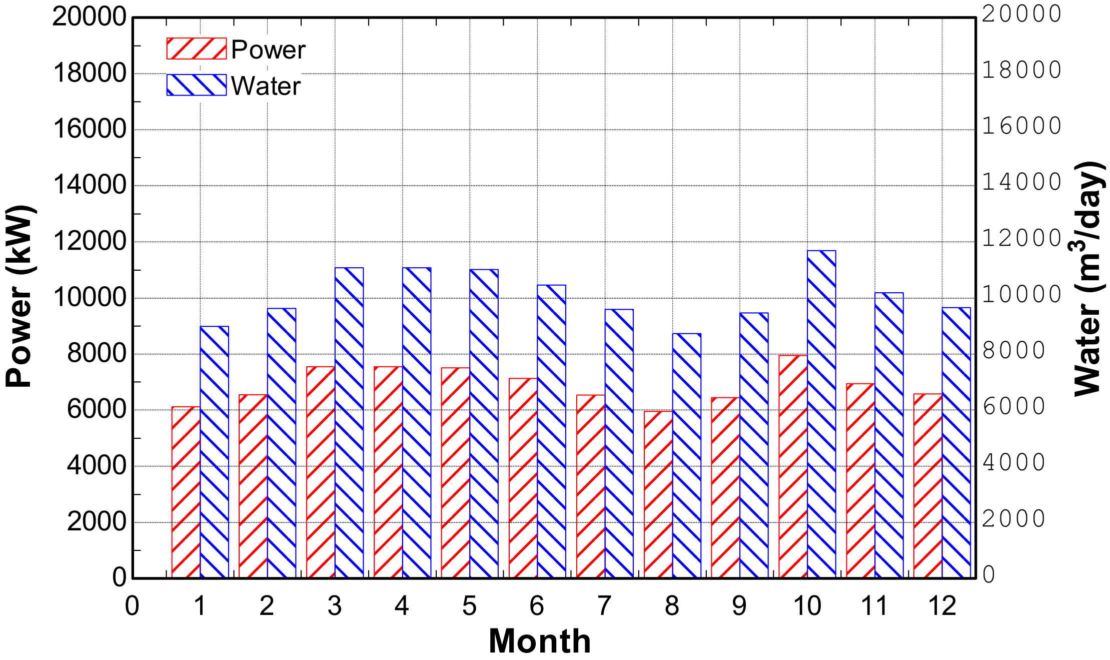

Figure 4.44 Average monthly power and water production for the region of Jizan, recompressive, f=0.5, n=12

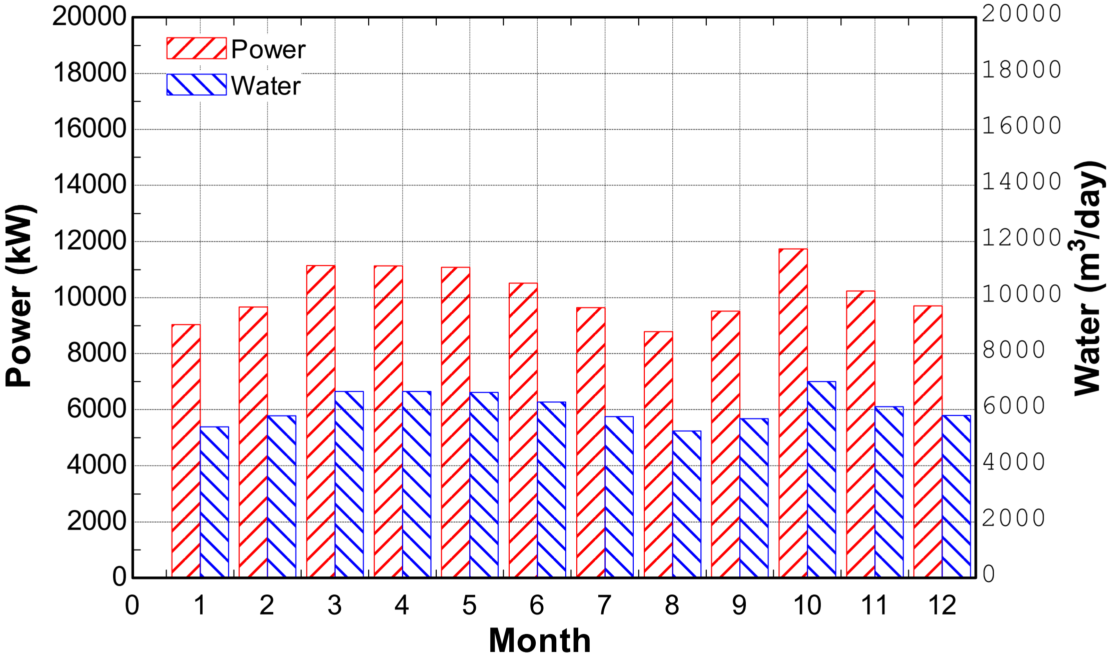

Figure 4.45 Average monthly power and water production for the region of Jizan, recompressive, f=0.7, n=12

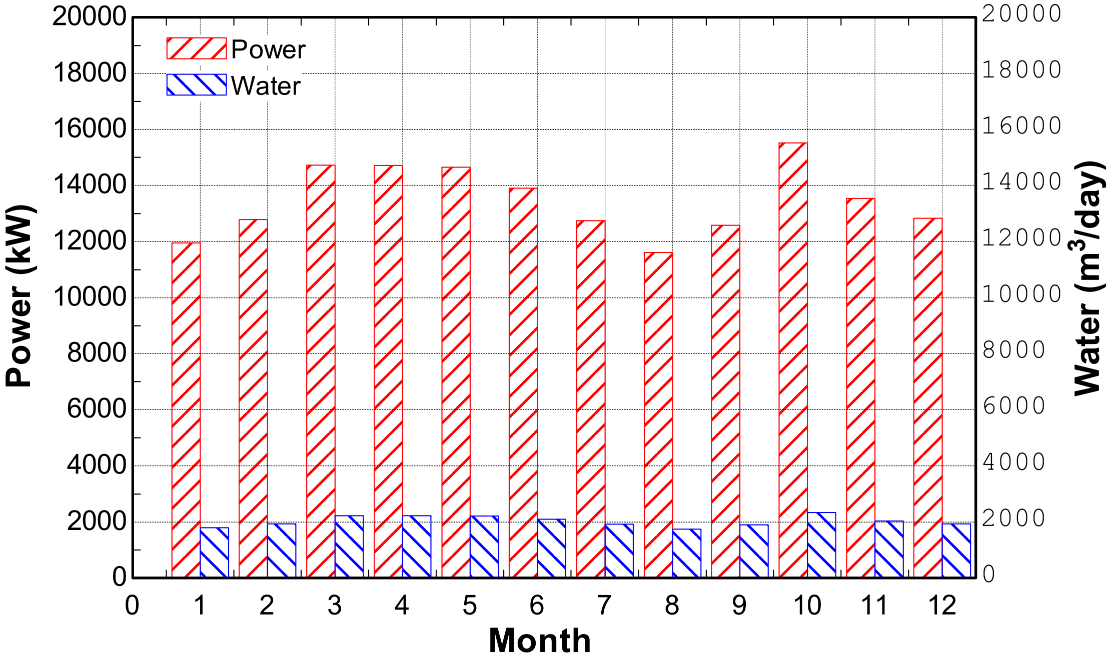

Figure 4.46 Average monthly power and water production for the region of Jizan, recompressive, f=0.9, n=12

Table 4.8 Average monthly power and water production for different regions and fractions, regenerative.

Regenerative																									
P (kW)		Month																							
W (m3/d)		Jan		Feb		Mar		Apr		May		Jun		Jul		Aug		Sep		Oct		Nov		Dec	
Region	f	P	W	P	W	P	W	P	W	P	W	P	W	P	W	P	W	P	W	P	W	P	W	P	W
Dhahran	0.5	4348	6905	5213	8279	5497	8730	5759	9146	7334	11647	8704	13822	7790	12371	7513	11931	7192	11422	6927	11001	5083	8073	3996	6347
	0.7	6442	4143	7724	4967	8146	5238	8534	5488	10867	6988	12897	8293	11542	7423	11132	7159	10657	6853	10264	6600	7532	4844	5922	3808
	0.9	8537	1381	10236	1656	10794	1746	11308	1829	14400	2329	17090	2764	15295	2474	14751	2386	14121	2284	13601	2200	9981	1615	7847	1269
Al Rughamah	0.5	5419	8606	7055	11205	7103	11280	6974	11076	7767	12335	9111	14469	8665	13762	8005	12713	6923	10994	6058	9620	5354	8503	4891	7767
	0.7	8030	5164	10454	6723	10524	6768	10334	6646	11509	7401	13500	8682	12840	8257	11861	7628	10258	6597	8976	5772	7933	5102	7247	4660
	0.9	10640	1721	13853	2241	13946	2256	13694	2215	15250	2467	17890	2894	17015	2752	15718	2543	13593	2199	11894	1924	10513	1701	9603	1553
Al Khafji	0.5	4568	7255	6366	10110	5650	8974	5283	8391	6690	10625	8527	13542	8158	12957	7882	12517	7453	11836	6632	10533	4657	7396	3974	6312
	0.7	6769	4353	9433	6066	8373	5384	7829	5034	9913	6375	12635	8125	12089	7774	11679	7510	11043	7102	9827	6320	6901	4438	5889	3787
	0.9	8970	1451	12500	2022	11095	1795	10374	1678	13136	2125	16743	2708	16019	2591	15476	2503	14634	2367	13022	2107	9144	1479	7804	1262
Yanbu	0.5	6232	9897	7341	11659	7929	12593	7876	12507	7852	12471	9204	14618	8697	13813	7845	12459	7195	11427	7220	11467	6584	10457	5901	9371
	0.7	9234	5938	10878	6995	11749	7556	11670	7504	11635	7482	13639	8771	12887	8288	11624	7475	10662	6856	10699	6880	9756	6274	8744	5623
	0.9	12237	1979	14414	2332	15569	2519	15464	2501	15418	2494	18073	2924	17077	2763	15403	2492	14128	2285	14177	2293	12929	2091	11587	1874
Khabt Al Ghosn	0.5	6463	10264	7221	11467	8134	12918	7957	12637	8280	13150	8357	13272	7850	12467	7440	11816	7074	11235	7781	12357	6618	10511	5926	9411
	0.7	9576	6158	10699	6880	12053	7751	11791	7582	12269	7890	12383	7963	11632	7480	11024	7089	10482	6741	11529	7414	9807	6307	8781	5647
	0.9	12690	2053	14178	2293	15971	2584	15625	2527	16258	2630	16409	2654	15413	2493	14608	2363	13891	2247	15278	2471	12995	2102	11635	1882
Jizan	0.5	5661	8990	6060	9624	6979	11084	6972	11073	6940	11021	6587	10461	6037	9588	5501	8736	5961	9467	7354	11680	6412	10184	6078	9653
	0.7	8388	5394	8980	5774	10342	6651	10331	6644	10283	6613	9760	6277	8946	5753	8151	5241	8833	5680	10897	7008	9501	6110	9007	5792
	0.9	11115	1798	11899	1925	13704	2217	13690	2215	13627	2204	12934	2092	11854	1918	10801	1747	11705	1893	14440	2336	12591	2037	11935	1931

Table 4.9 Average monthly power and water production for different regions and fractions, recompressive.

Recompressive																									
P (kW)		Month																							
W (m3/d)		Jan		Feb		Mar		Apr		May		Jun		Jul		Aug		Sep		Oct		Nov		Dec	
Region	f	P	W	P	W	P	W	P	W	P	W	P	W	P	W	P	W	P	W	P	W	P	W	P	W
Dhahran	0.5	4702	6905	5638	8279	5946	8730	6229	9146	7932	11647	9414	13822	8426	12371	8127	11931	7780	11422	7493	11001	5499	8073	4323	6347
	0.7	6938	4143	8320	4967	8773	5238	9192	5488	11705	6988	13892	8293	12433	7423	11992	7159	11480	6853	11057	6600	8114	4844	6380	3808
	0.9	9175	1381	11001	1656	11601	1746	12154	1829	15477	2329	18369	2764	16440	2474	15856	2386	15179	2284	14621	2200	10730	1615	8436	1269
Al Rughamah	0.5	5861	8606	7630	11205	7682	11280	7543	11076	8401	12335	9855	14469	9373	13762	8659	12713	7489	10994	6553	9620	5792	8503	5291	7767
	0.7	8648	5164	11260	6723	11335	6768	11131	6646	12396	7401	14542	8682	13831	8257	12777	7628	11050	6597	9669	5772	8547	5102	7807	4660
	0.9	11435	1721	14889	2241	14989	2256	14718	2215	16391	2467	19229	2894	18289	2752	16895	2543	14612	2199	12786	1924	11301	1701	10323	1553
Al Khafji	0.5	4941	7255	6885	10110	6111	8974	5714	8391	7236	10625	9223	13542	8825	12957	8526	12517	8062	11836	7175	10533	5038	7396	4300	6312
	0.7	7291	4353	10160	6066	9018	5384	8432	5034	10677	6375	13610	8125	13022	7774	12581	7510	11896	7102	10587	6320	7434	4438	6344	3787
	0.9	9640	1451	13434	2022	11924	1795	11150	1678	14119	2125	17996	2708	17219	2591	16635	2503	15730	2367	13999	2107	9830	1479	8389	1262
Yanbu	0.5	6740	9897	7940	11659	8576	12593	8518	12507	8493	12471	9956	14618	9408	13813	8486	12459	7784	11427	7811	11467	7123	10457	6384	9371
	0.7	9945	5938	11716	6995	12655	7556	12569	7504	12533	7482	14691	8771	13882	8288	12522	7475	11485	6856	11525	6880	10510	6274	9420	5623
	0.9	13151	1979	15492	2332	16733	2519	16620	2501	16572	2494	19426	2924	18356	2763	16557	2492	15187	2285	15240	2293	13898	2091	12456	1874
Khabt Al Ghosn	0.5	6990	10264	7809	11467	8798	12918	8607	12637	8956	13150	9039	13272	8491	12467	8048	11816	7653	11235	8417	12357	7160	10511	6411	9411
	0.7	10314	6158	11523	6880	12982	7751	12700	7582	13215	7890	13338	7963	12529	7480	11875	7089	11292	6741	12420	7414	10565	6307	9459	5647
	0.9	13638	2053	15238	2293	17166	2584	16793	2527	17475	2630	17637	2654	16568	2493	15703	2363	14931	2247	16423	2471	13970	2102	12508	1882
Jizan	0.5	6122	8990	6554	9624	7549	11084	7541	11073	7506	11021	7125	10461	6530	9588	5950	8736	6449	9467	7956	11680	6937	10184	6576	9653
	0.7	9034	5394	9671	5774	11139	6651	11128	6644	11076	6613	10513	6277	9636	5753	8780	5241	9515	5680	11739	7008	10236	6110	9703	5792
	0.9	11946	1798	12788	1925	14729	2217	14714	2215	14646	2204	13902	2092	12742	1918	11610	1747	12582	1893	15523	2336	13535	2037	12830	1931

The average yearly power and water productivity for different regions of the Kingdom of Saudi Arabia, namely, Dhahran, Jabal Al-Rughamah, Al-Khafji, Yanbu Al-Nakhil, Khabt Al-Ghusn, and Jizan are presented in Figure 4.47 through Figure 4.50. These figures show the results for Regenerative and Recompressive cycles under an operating condition of fractions of 0.5 and 0.7. It could be also seen from Figure 4.47 through Figure 4.50 that the cogeneration plant production in different regions of Saudi Arabia has comparable values. The highest productivity, however, is that of the region of Yanbu, followed by Khabt Al-Ghusn in the second place, and the rest are as follows, Jabal Al-Rughamah, Jizan, Al-Khafji, and Dhahran in descending order. While Figure 4.11 through Figure 4.28 and Figure 4.29 through Figure 4.46 represent the average monthly power and water production rate for each of the regions under study, Figure 4.47 through Figure 4.50 represent these results averaged over the whole year for the fractions of 0.5 and 0.7 for power and water productivity comparison between the regions. Figure 4.47 and Figure 4.48 represent the results for the regenerative cogeneration cycle and Figure 4.49 and Figure 4.50 represent the results for the recompressive cogeneration cycle. The difference between the regenerative and recompressive cogeneration cycles at the same value of fraction is that they produce the same amount of water with slightly more power production for the recompressive cycle due to the higher efficiency of the recompressive cycle compared with the regenerative cycle, this can be seen in comparing Figure 4.47 and Figure 4.49, and Figure 4.48 and Figure 4.50 for fractions of 0.5 and 0.7 respectively. These results represent the general capacity of the solar cogeneration systems studied. Further elaboration on the efficiency of the solar cogeneration systems subject to variations in the fraction accounted for the power cycle and the turbine inlet pressure and temperature is studied later on in this chapter.

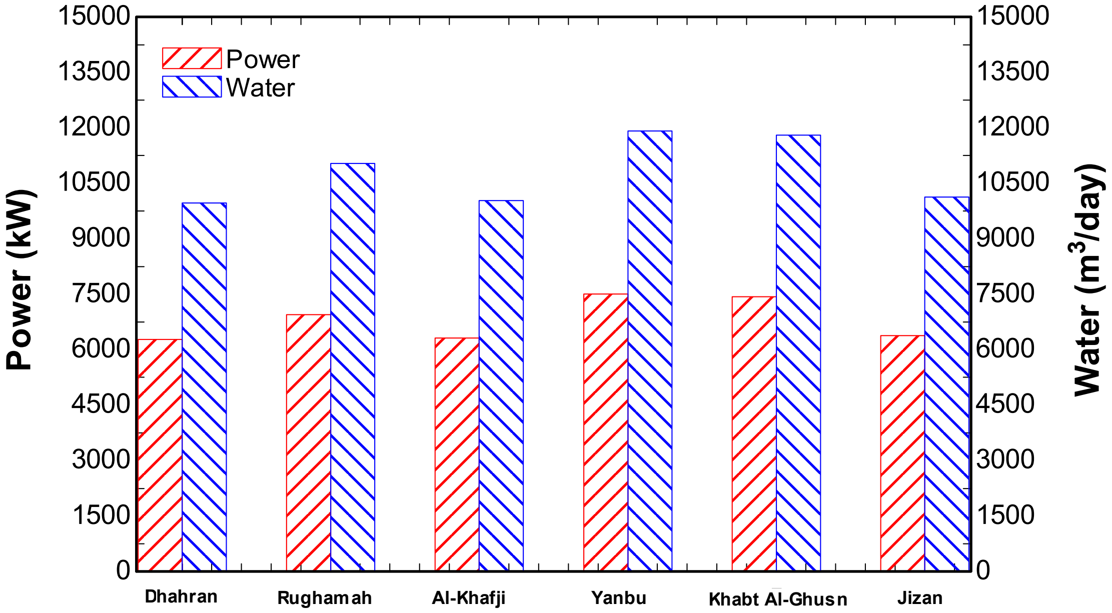

Figure 4.47 Average yearly power and water production for different regions, regenerative, f=0.5, n=12

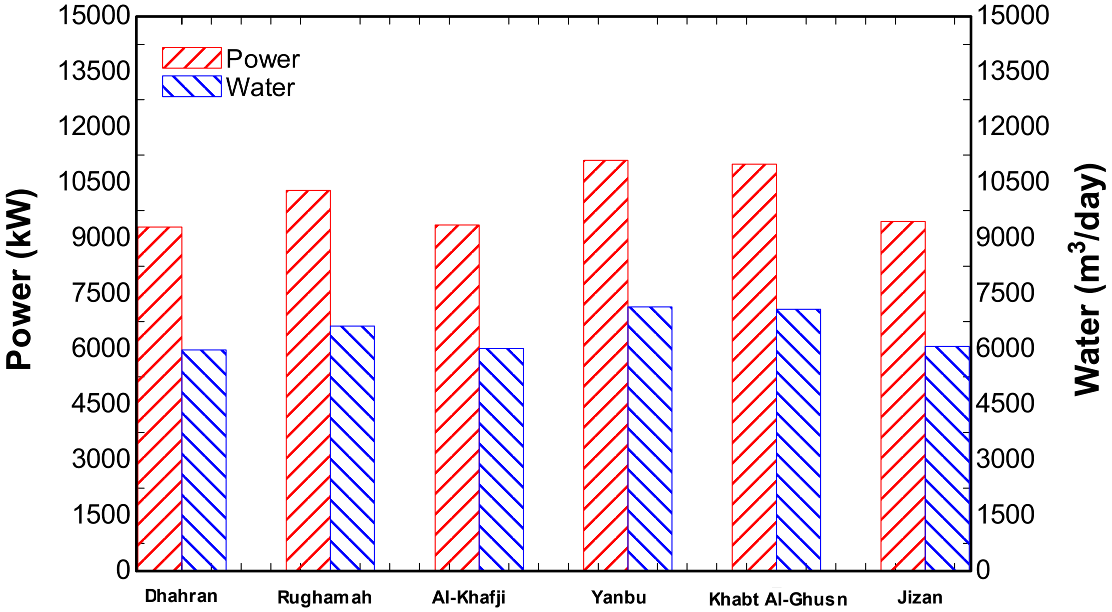

Figure 4.48 Average yearly power and water production for different regions, regenerative, f=0.7, n=12

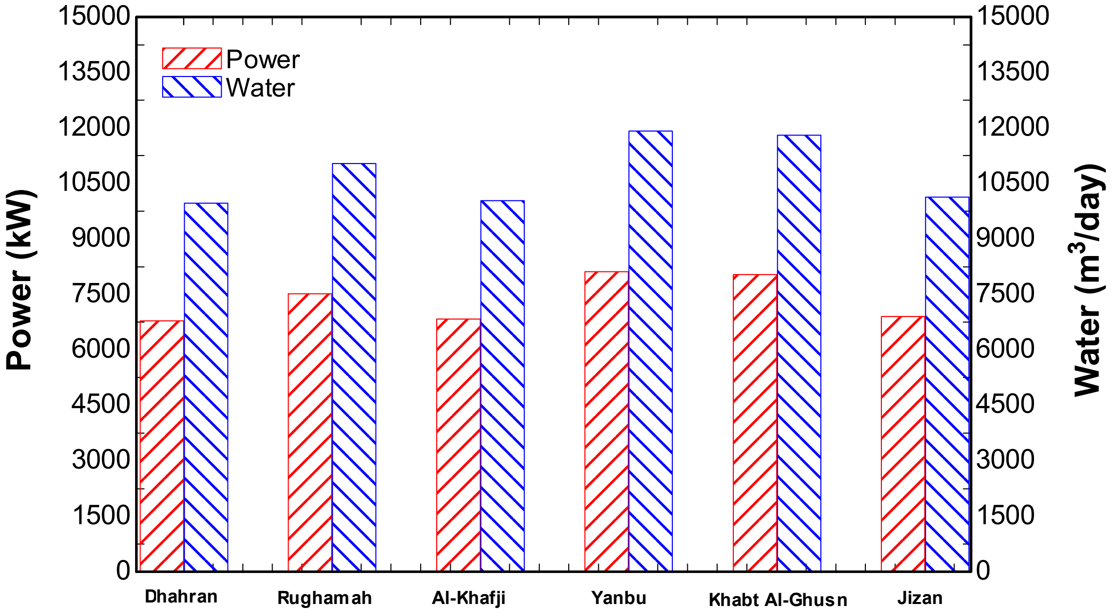

Figure 4.49 Average yearly power and water production for different regions, recompressive, f=0.5, n=12

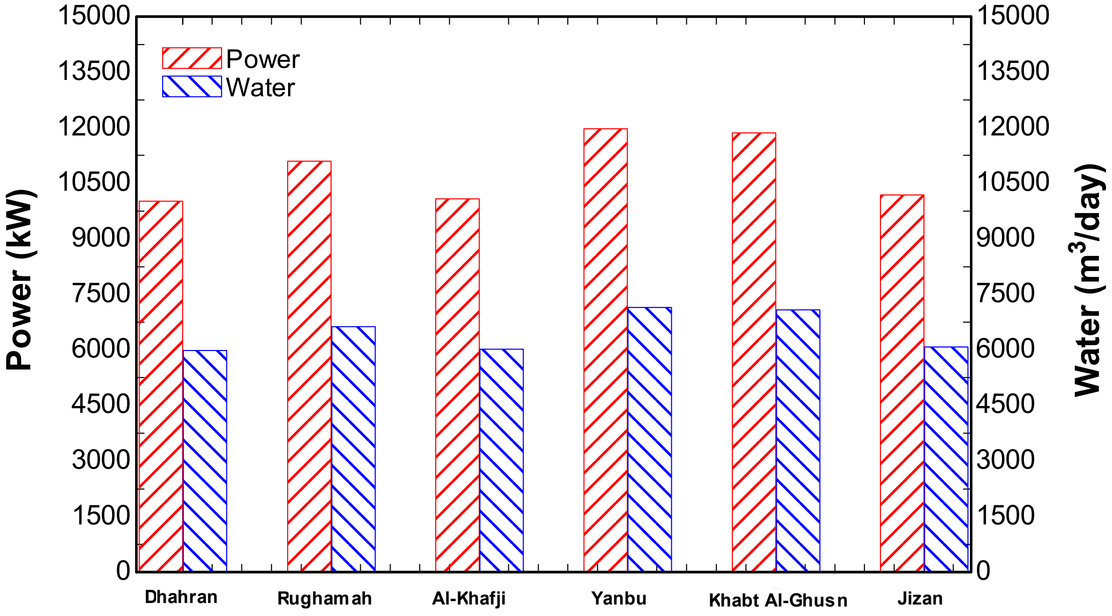

Figure 4.50 Average yearly power and water production for different regions, recompressive, f=0.7, n=12

Figure 4.51 and Figure 4.52 represent the values for the different efficiency expressions for different values of fraction for the regenerative and the recompressive cogeneration cycles respectively. The utilization factor as can be seen in the figures metioned has the highest values since it overestimates the performance of the system. The conventional efficiency expressions results in the least values since it only accounts for the power output with no account for the heat utilized by the desalination system. The values of the work of separation efficiency expression are slightly higher than those of the conventional expression; that is due to the added value of the work of separation in the desalination system. However, the work of separation is very small due to the high entropy generation in the desalination system, thus, underestimating the performance of the cogeneration system as well. A logic choice would be that of the cogeneration efficiency developed in the previous chapter. The cogeneration efficiency accounts for the effective heat input to the desalination system. The values resulting from that expression are intermediate, in between the values of the utilization factor and the conventional efficiency. The efficiency expression accounting for the heat input at the receiver level is shown to have the highest value since the ratio is that of the effective output to the net energy collected at the central receiver level and not the total solar energy entering the system at the heliostats level. It can be seen, also, that the utilization factor, effective efficiency, and the receiver level efficiency is decreasing with the increasing fraction; that is, because increasing the fraction of heat into the sCO_2 power cycle results in a more low quality heat lost from the power cycle to heat up the seawater entering the MEE-TVC system, and thus, more rejected seawater, which will imply a loss of energy. The conventional and separation efficiency expressions, however, increase with the increase in fraction since their value depends critically on the production of the

sCO_2 power cycle. In comparing Figure 4.51 and Figure 4.52, recompressive cogeneration efficiency expressions achieve higher values than that of the regenerative.

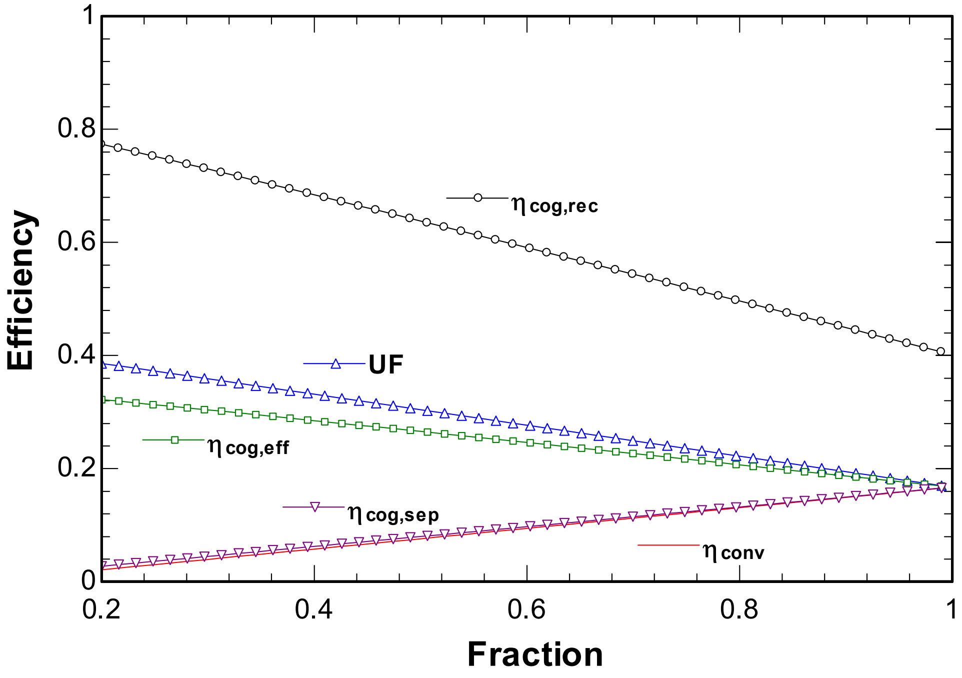

Figure 4.51 Average yearly different efficiency expressions values, regenerative, n=12

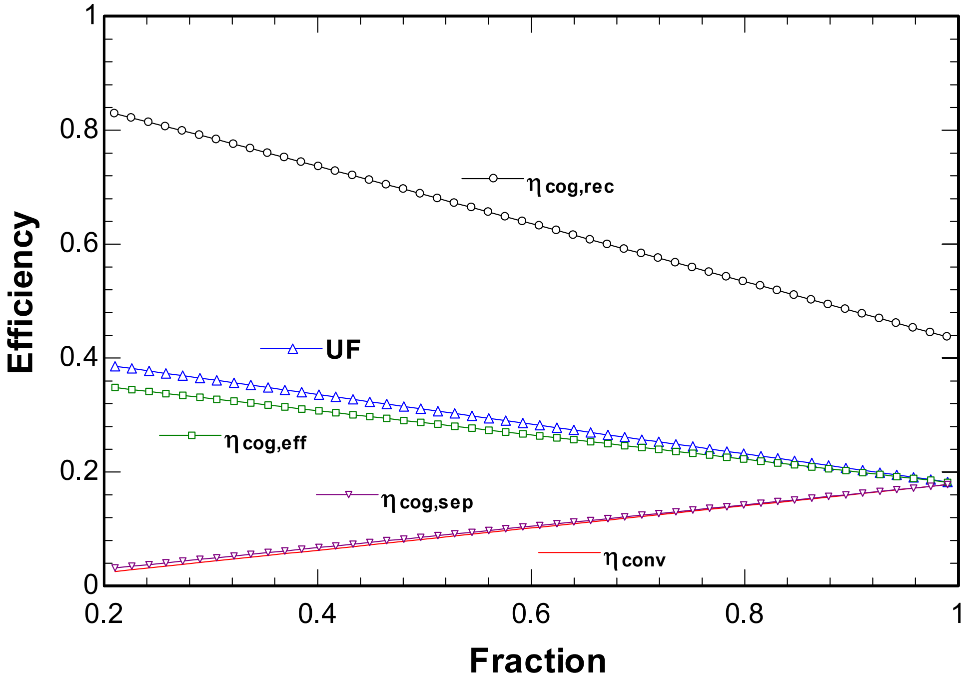

Figure 4.52 Average yearly different efficiency expressions values, recompressive, n=12

Figure 4.53 and Figure 4.54 represent the effect of fraction over the power to water ratio for the regenerative and recompressive cycles, respectively. Figure 4.55 and Figure 4.56 represent the effect of the turbine inlet temperature over the power to water ratio for the regenerative and recompressive cogeneration cycles respectively for fractions of 0.4, 0.6, and 0.8 and different number of effects. The turbine inlet temperature variation has a larger effect over the power to water ratio of the recompressive cogeneration cycle than that of the regenerative cogeneration cycle. The increase in the fraction of heat accounted for the power cycle results in increasing the power to water ratio and a lower number of effects results in an increase in the power to water ratio since the amount of distilled water produced is less.

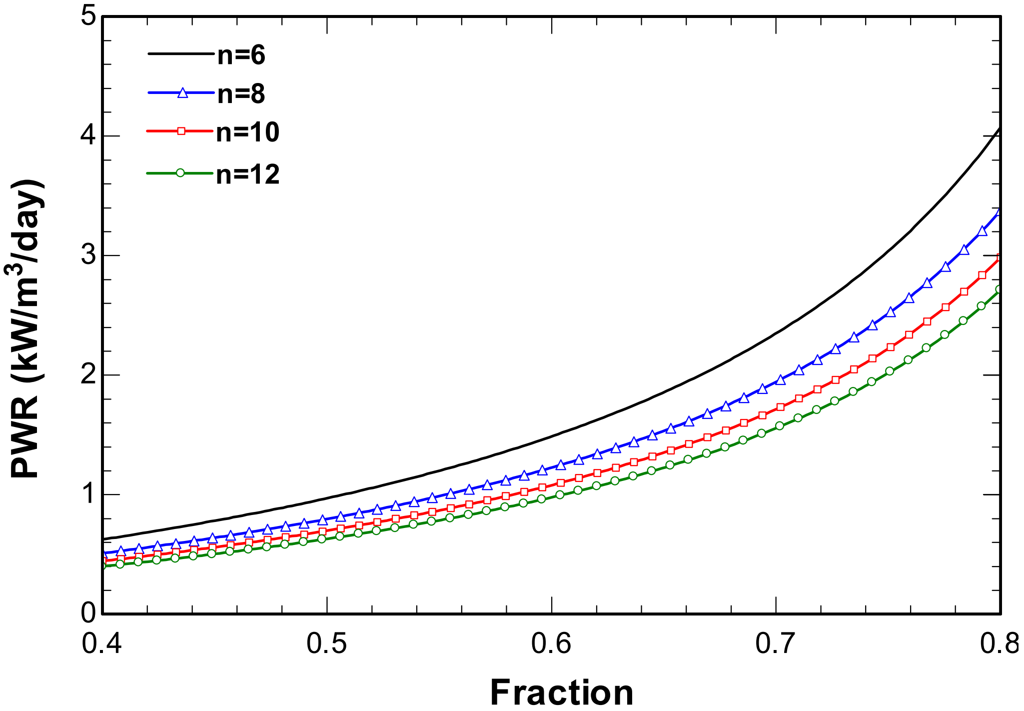

Figure 4.53 Power to water ratio versus fraction, regenerative

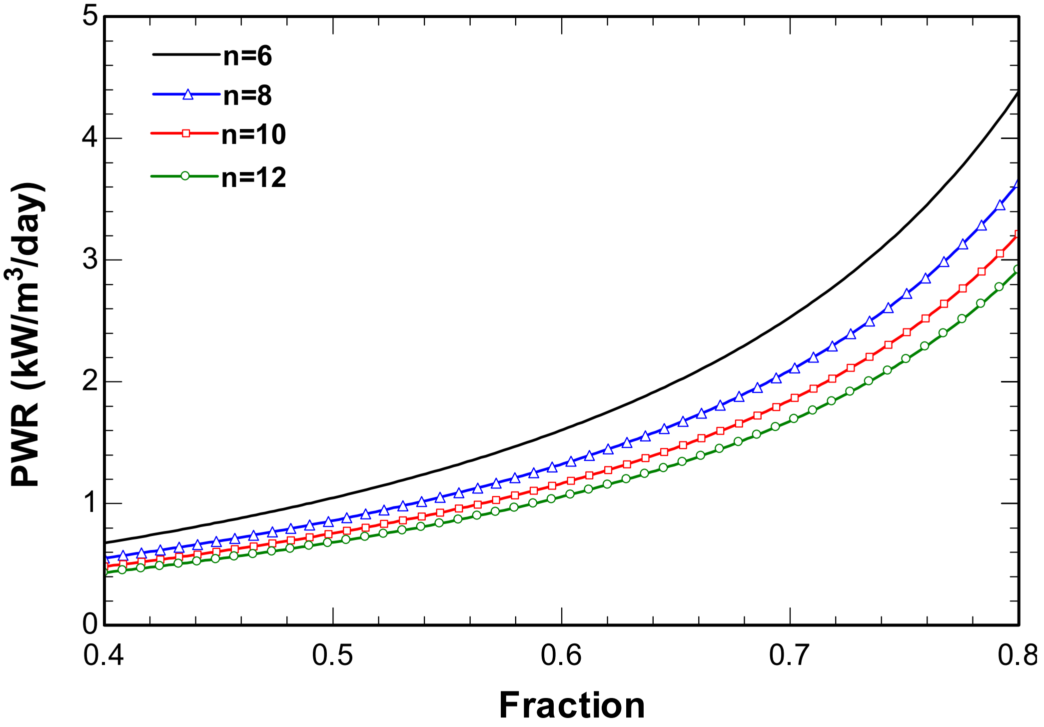

Figure 4.54 Power to water ratio versus fraction, recompressive

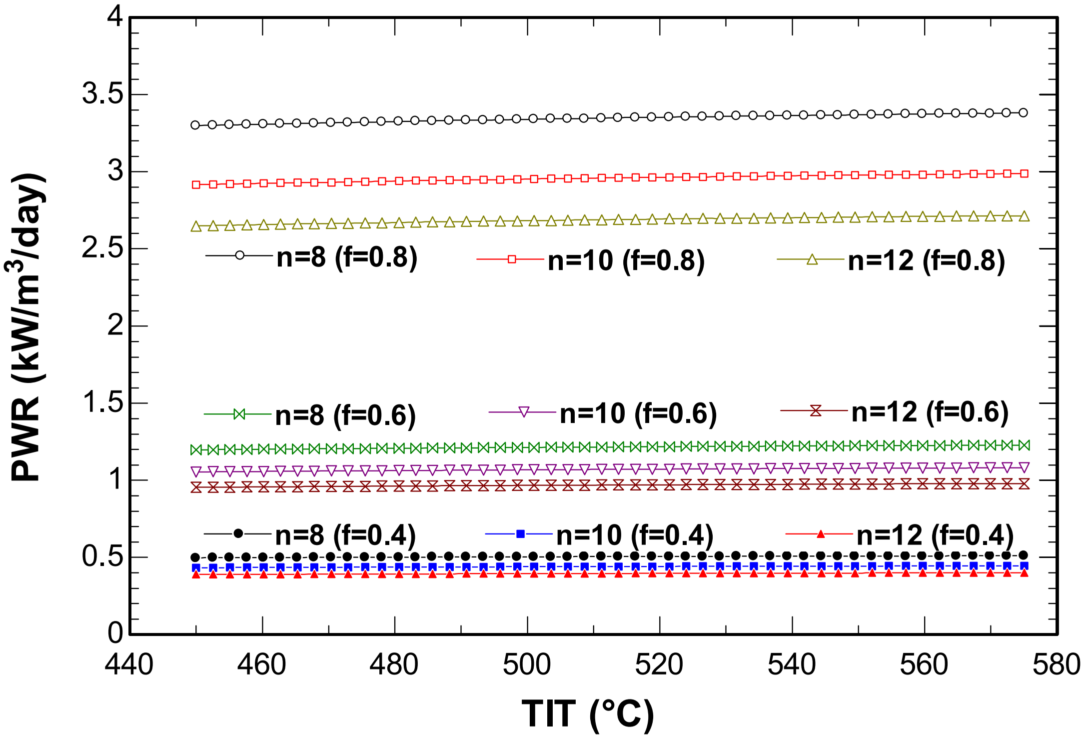

Figure 4.55 Power to water ratio versus turbine inlet temperature for different fractions, regenerative

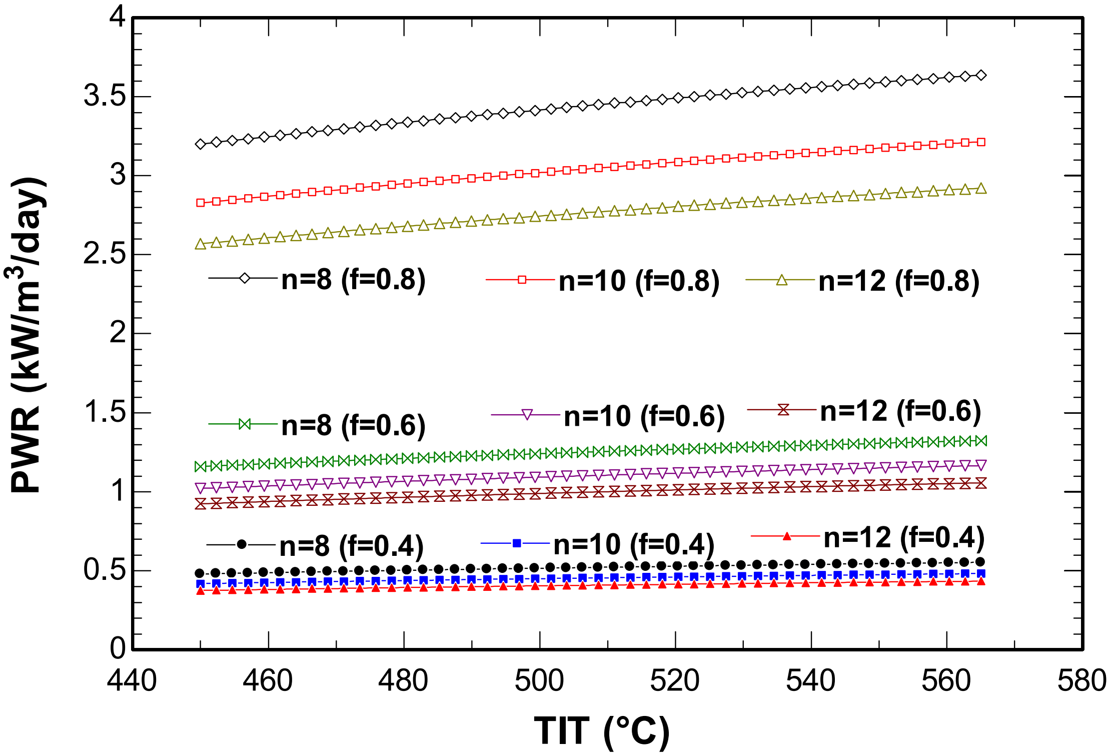

Figure 4.56 Power to water ratio versus turbine inlet temperature for different fractions, recompressive

It can be seen from Figure 4.57 and Figure 4.58 that the regenerative cogeneration cycle is more sensitive to the turbine inlet pressure than the turbine inlet temperature. The increase in the turbine inlet pressure results in an increase in the power to water ratio since the increase in pressure increases the power output of the power cycle. The increase in the number of effects of the MEE-TVC desalination system, however, decreases the power to water ratio due to the increase in the distillate mass flow rate. In both cases, regenerative and recompressive cogeneration cycles, the increase in the fraction increases the power to water ratio as can be seen from the figures.

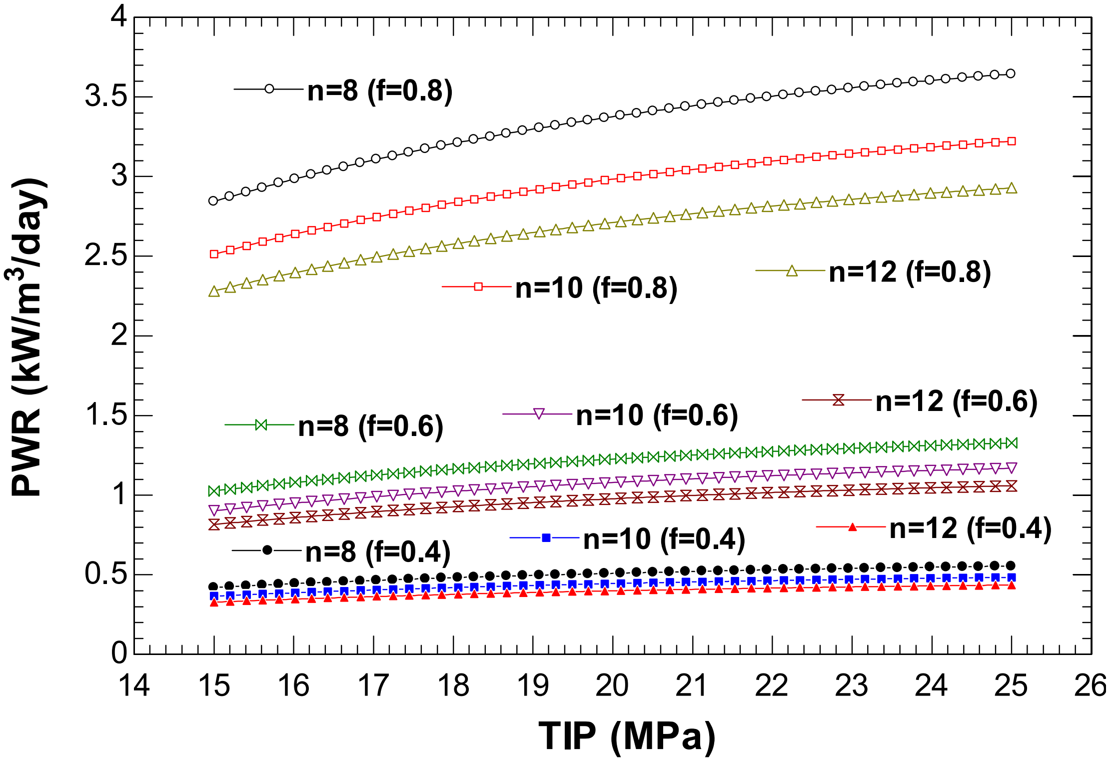

Figure 4.57 Power to water ratio versus turbine inlet pressure for different fractions, regenerative

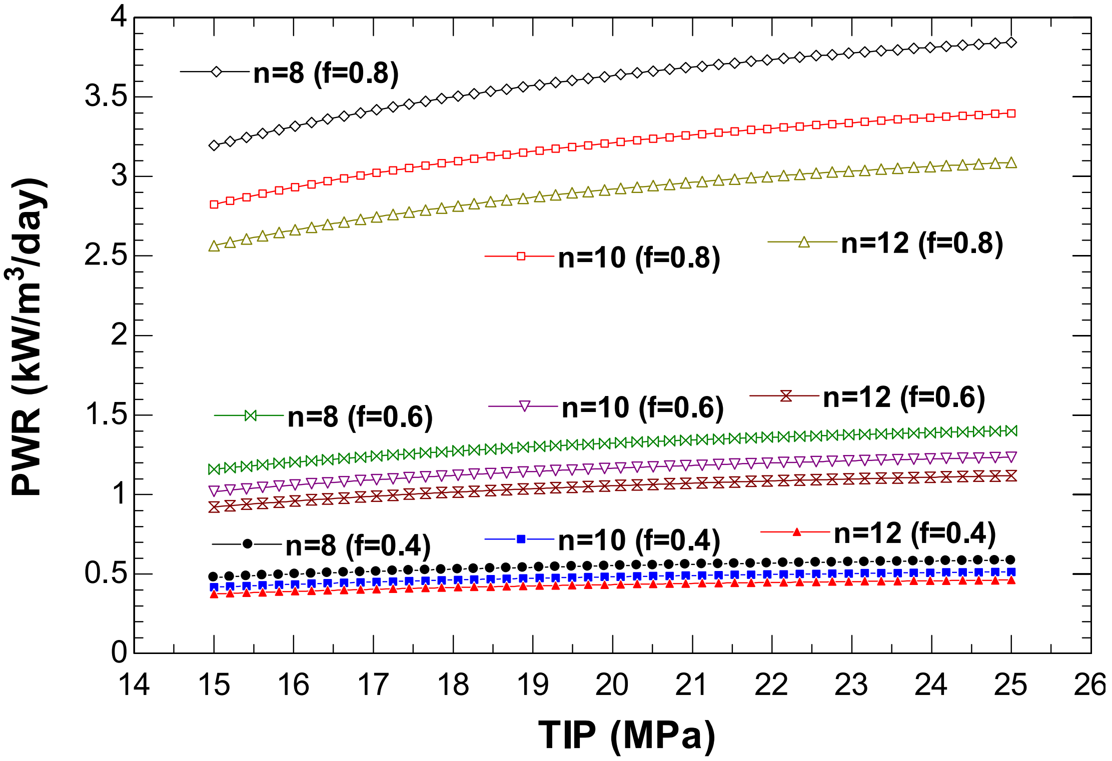

Figure 4.58 Power to water ratio versus turbine inlet pressure for different fractions, recompressive

The effect of the turbine inlet temperature on the cogeneration efficiency for the regenerative and recompressive cycles is shown in Figure 4.59 through Figure 4.62 respectively. The recompressive cycle efficiency is more sensitive to changes in the turbine inlet temperature than the regenerative cycle. However, the regenerative cycle efficiency is more sensitive to changes in the turbine inlet pressure than it is to the temperature as can be shown in Figure 4.59 and Figure 4.61 representing the effect of the turbine inlet temperature and turbine inlet pressure respectively on the efficiency of the regenerative cogeneration cycle for different fractions. In general, the increase in the pressure and temperature entering the turbine results in increasing the efficiency. Decreasing the fraction of heat entering the power cycle results in increasing the efficiency since the fraction removed from the power cycle will be used for the desalination cycle, and increasing the number of effects of the MEE-TVC system increases the overall efficiency.

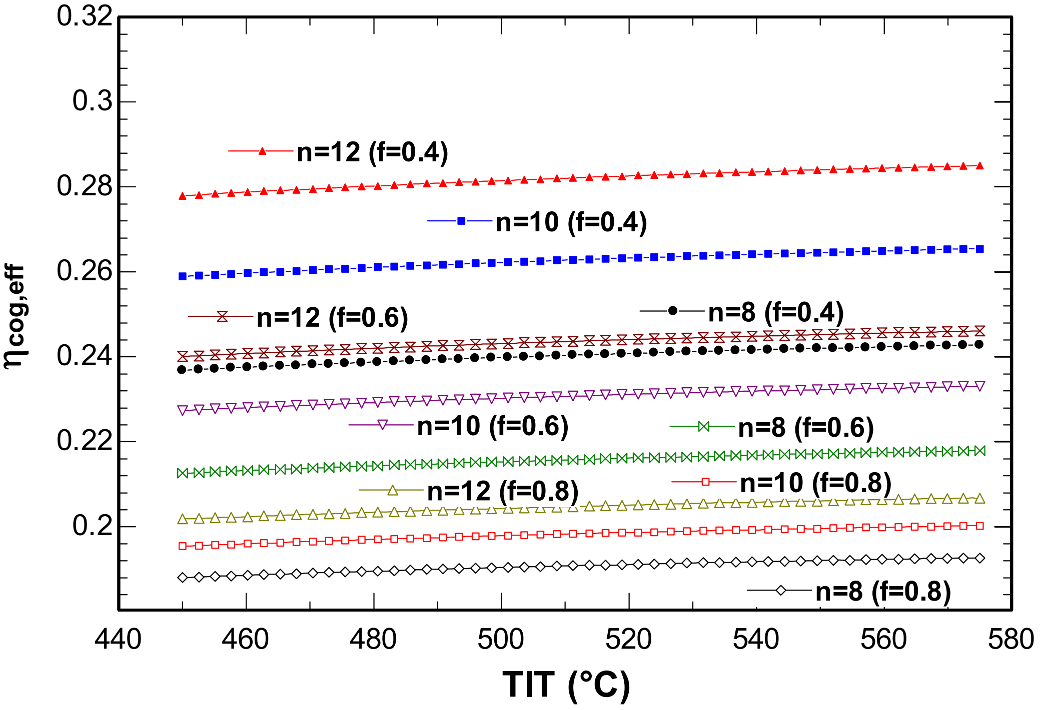

Figure 4.59 Effective cogeneration efficiency versus turbine inlet temperature, regenerative

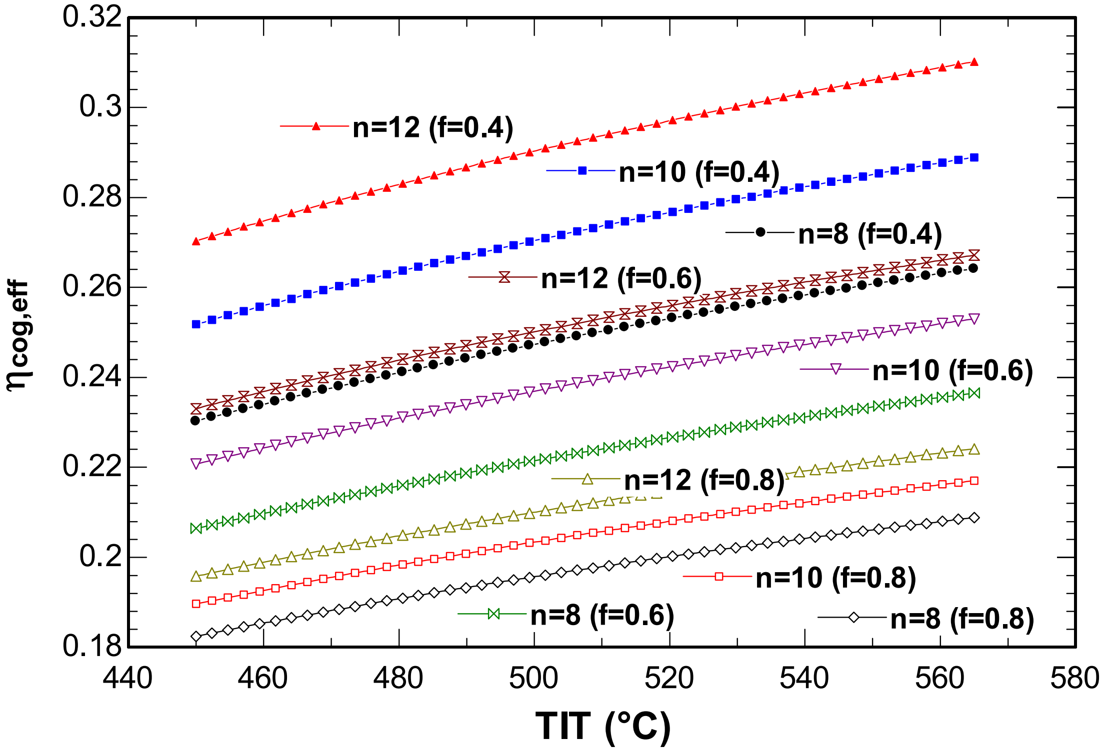

Figure 4.60 Effective cogeneration efficiency versus turbine inlet temperature, recompressive

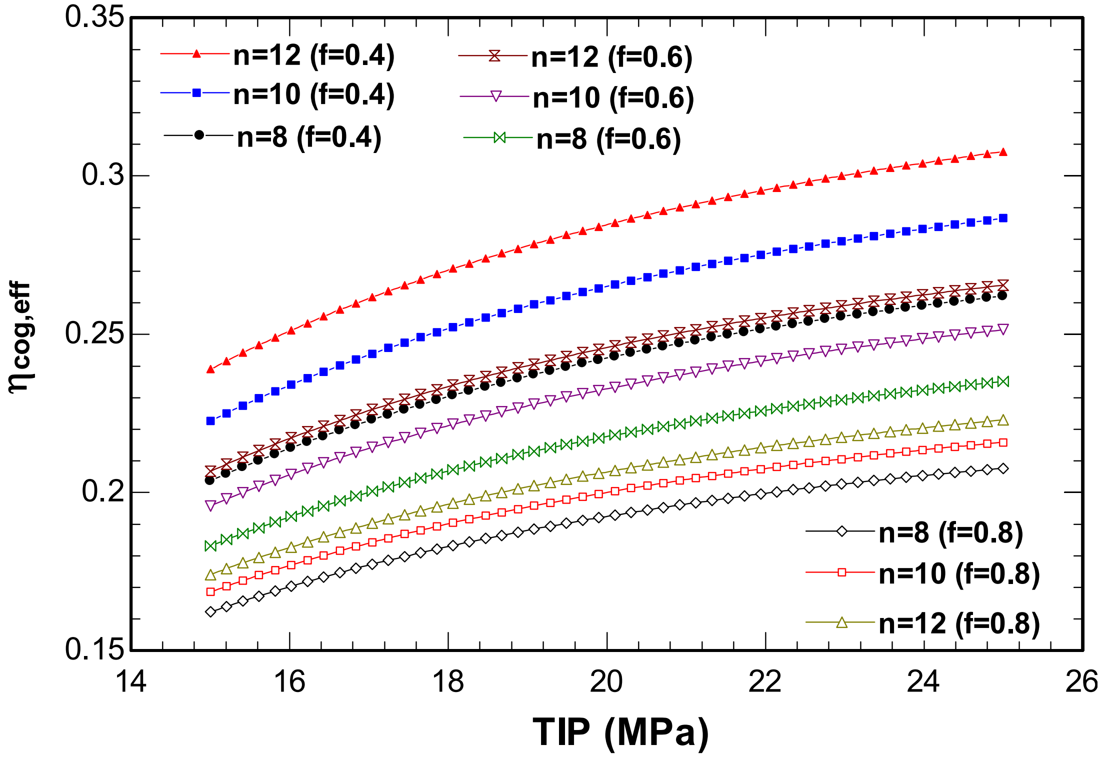

Figure 4.61 Effective cogeneration efficiency versus turbine inlet pressure, regenerative

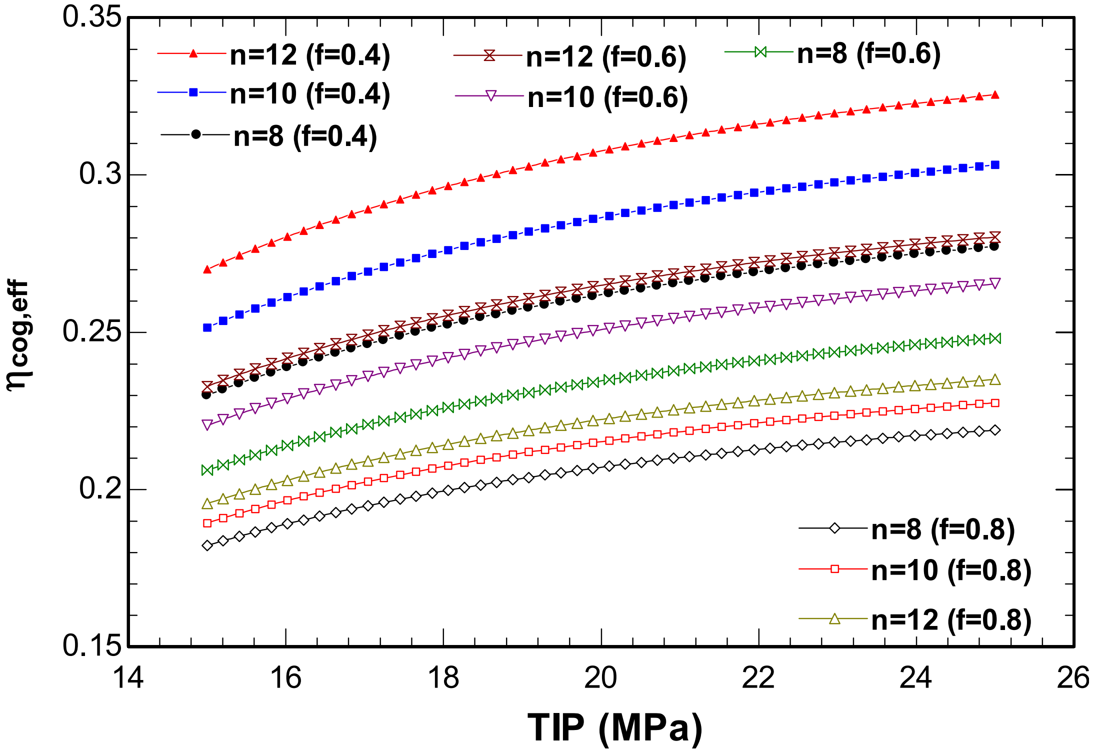

Figure 4.62 Effective cogeneration efficiency versus turbine inlet pressure, recompressive

Figure 4.63 and Figure 4.64 represent the effect of the top brine salinity over the cogeneration efficiency for regenerative and recompressive cogeneration cycles and for fractions of 0.5 and 0.8. The increase in the top brine salinity from 50000 ppm to 70000 ppm results in a slight increase in the overall efficiency of the cogeneration systems. Moreover, it is observed that the cogeneration systems with higher number of effects are slightly more sensitive to the variation in the top brine salinity as can be seen from the figures.

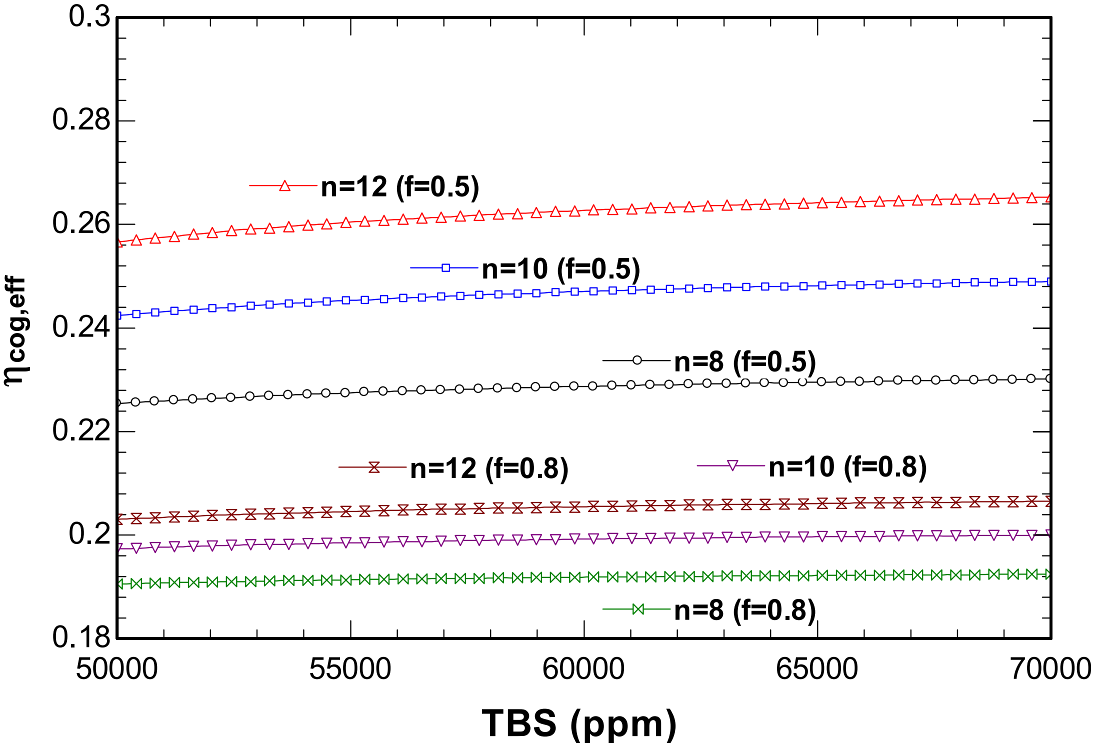

Figure 4.63 Effective cogeneration efficiency versus top brine salinity, regenerative

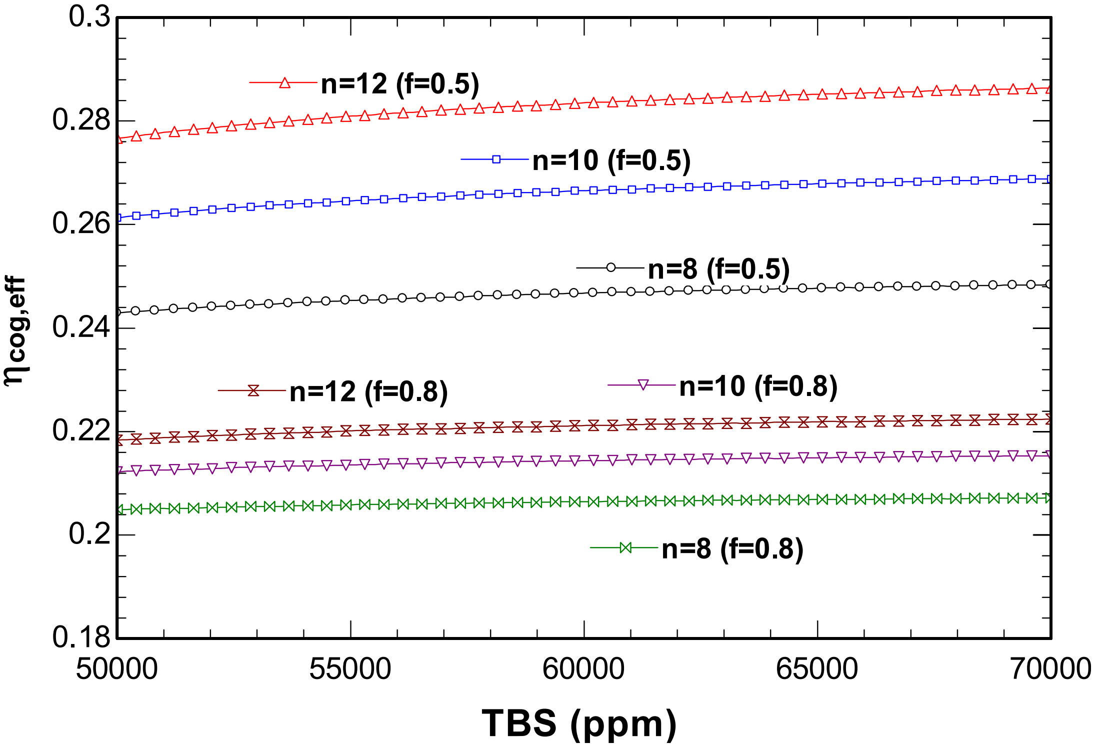

Figure 4.64 Effective cogeneration efficiency versus top brine salinity, recompressive

4.6 Entropy Generation

Table 4.10 Entropy generation (%) contribution of each component of MEE-TVC

		Number of Effects						
		6	7	8	9	10	11	12
Components	Effects	13.40	14.05	15.00	15.54	16.24	16.69	17.22
	Preheaters	2.26	2.64	3.36	4.08	4.88	5.67	6.55
	Flashboxes	0.34	0.43	0.55	0.67	0.80	0.92	1.06
	SJE (steam jet ejector)	60.06	59.55	57.85	56.53	55.02	53.75	52.35
	Down Condenser	10.50	10.16	9.97	9.80	9.63	9.46	9.30
	Distillate	3.16	3.04	3.25	3.47	3.64	3.81	3.95
	Thermal	3.54	3.36	3.65	3.94	4.19	4.44	4.66
	Chemical	1.34	1.51	1.61	1.70	1.76	1.83	1.88
	Rej SW	5.41	5.25	4.76	4.27	3.85	3.42	3.04

Table 4.10 represents the entropy production contribution for each of the components of the MEE-TVC system from the total entropy generation of the MEE-TVC. It can be obviously seen that the highest contributing component in the whole system is the steam jet ejector, reaching 60 % for the system with 6 effects. This fraction will decrease to 52 % for the system with 12 effects. The second largest contribution is from the effects, generating 13 to 14 percent from total entropy generation for 6 and 12 effects respectively. The down condenser is the third contributor; the percentage varies around 10 % for the systems with different number of effects. The distillate, rejected seawater, and brine also contribute in varying percentages to the entropy production. It can be seen, however, that the percentage of contribution from bringing brine to chemical equilibrium with the environment is less than that for bringing it to thermal equilibrium with the environment. The entropy generation resulting from bringing the distillate product to thermal equilibrium with the environment constitutes about three percent from the total. The preheaters contribute in small portions as well. The flash boxes occupy the least contribution to the total entropy generation of the system.

It can be seen from Figure 4.65 that the entropy generation decreases with increasing top brine salinity. Figure 4.66 and Figure 4.67 represent the specific entropy generation of the MEE-TVC system and sCO_2 power cycle versus fraction for different number of effects. It can be seen that the specific entropy generation of the MEE-TVC system increases when the fraction of heat accounted for the power cycle increases. That is, because the lost heat from the power cycle is used to heat the seawater entering the MEE-TVC system. Increasing the fraction, increases the amount of rejected seawater which generates entropy through chemical and thermal equilibrium with the environment. Moreover, it is seen that for systems with larger number of effects, the specific entropy generation is less. Therefore, to minimize the specific entropy generation in the MEE-TVC system, larger effects must be used and lower fractions of heat entering to the sCO_2 power cycle. However, the lowest fraction of heat possible entering the power cycle is limited by the minimum amount of seawater that should be heated to the desired feed temperature. If the fraction of heat accounted for the power cycle is too low, larger fraction of heat is used for the desalination system. In the latter case, more feed seawater will be required, and thus more seawater will be required. If the fraction of heat accounted for the power cycle is too low, the heat exchanger between the sCO_2 power cycle and the desalination system will not be able to provide enough energy to heat the desired amount of seawater into the desalination system. Thus, the conclusion is that the lowest fraction possible is that which renders the seawater flow rate equal to the feed flow rate with no rejected seawater back to the sea. In addition to the specific entropy of the MEE-TVC desalination system, the specific entropy of the sCO_2 cycle remains unchanged, for both cycles, regenerative and recompressive, and for the whole range of fraction. That is, because the increase in the total entropy generation of sCO_2 increases the mass flow rate of CO_2 proportionally.

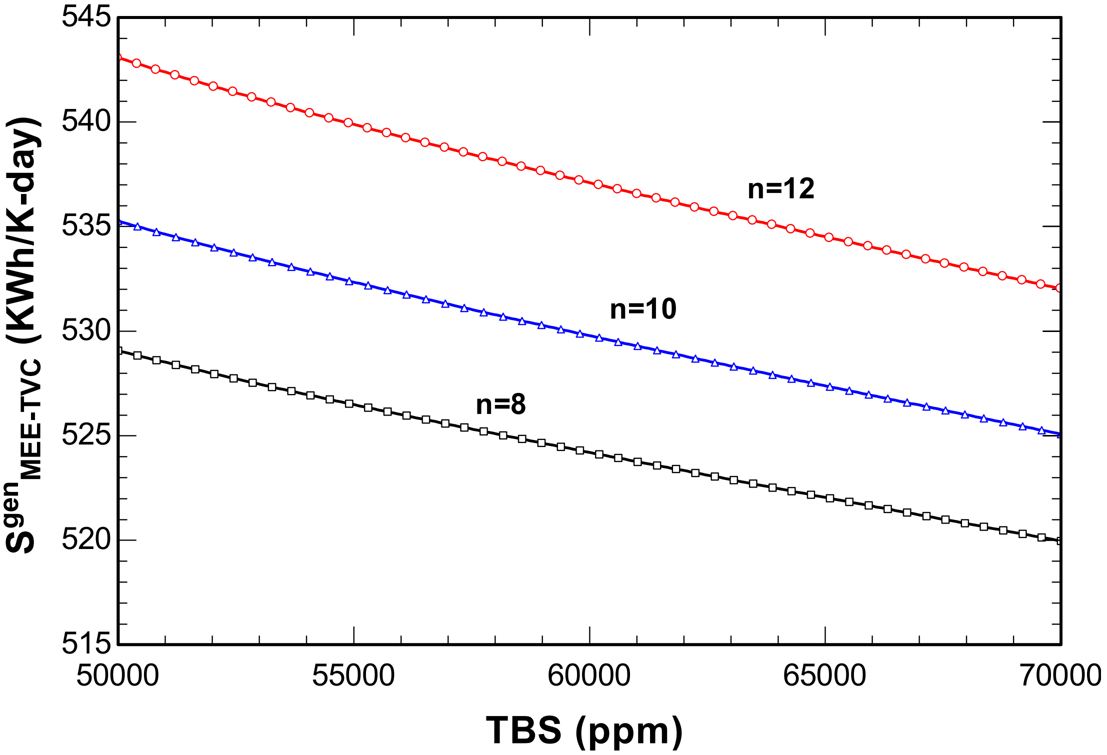

Figure 4.65 Entropy Generation in MEE-TVC system versus top brine salinity, n=12, f=0.5

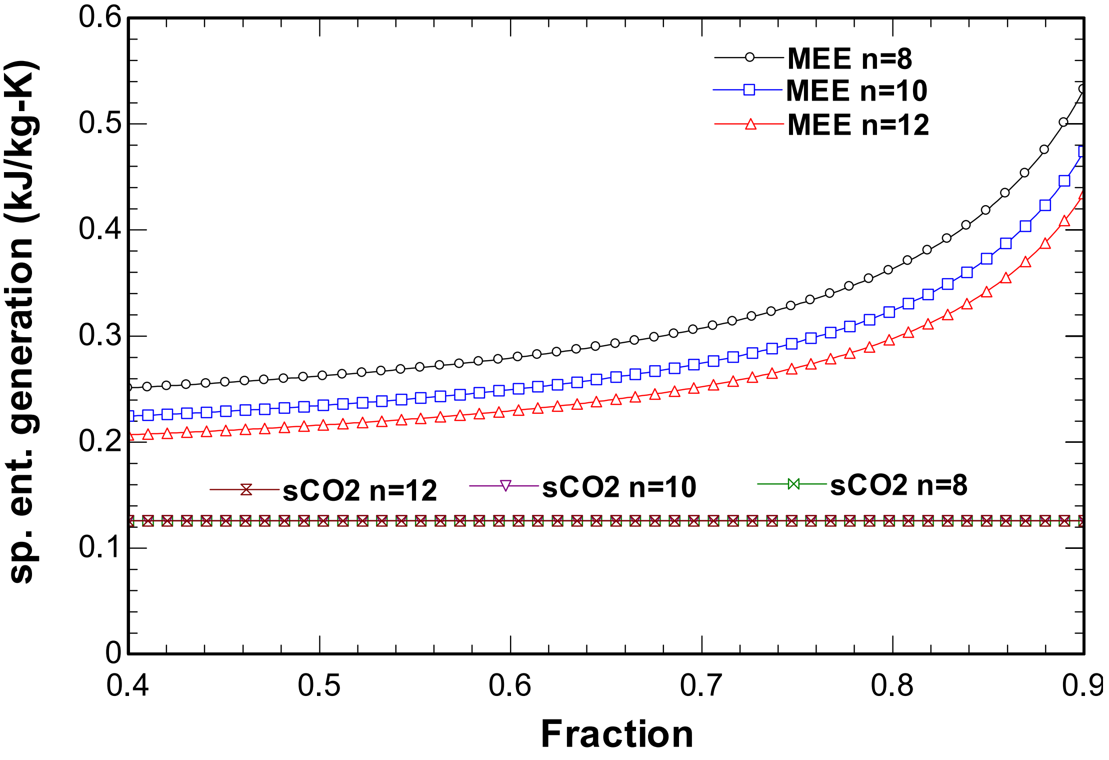

Figure 4.66 Specific entropy generation in MEE-TVC system and sCO_2 cycle versus fraction, regenerative

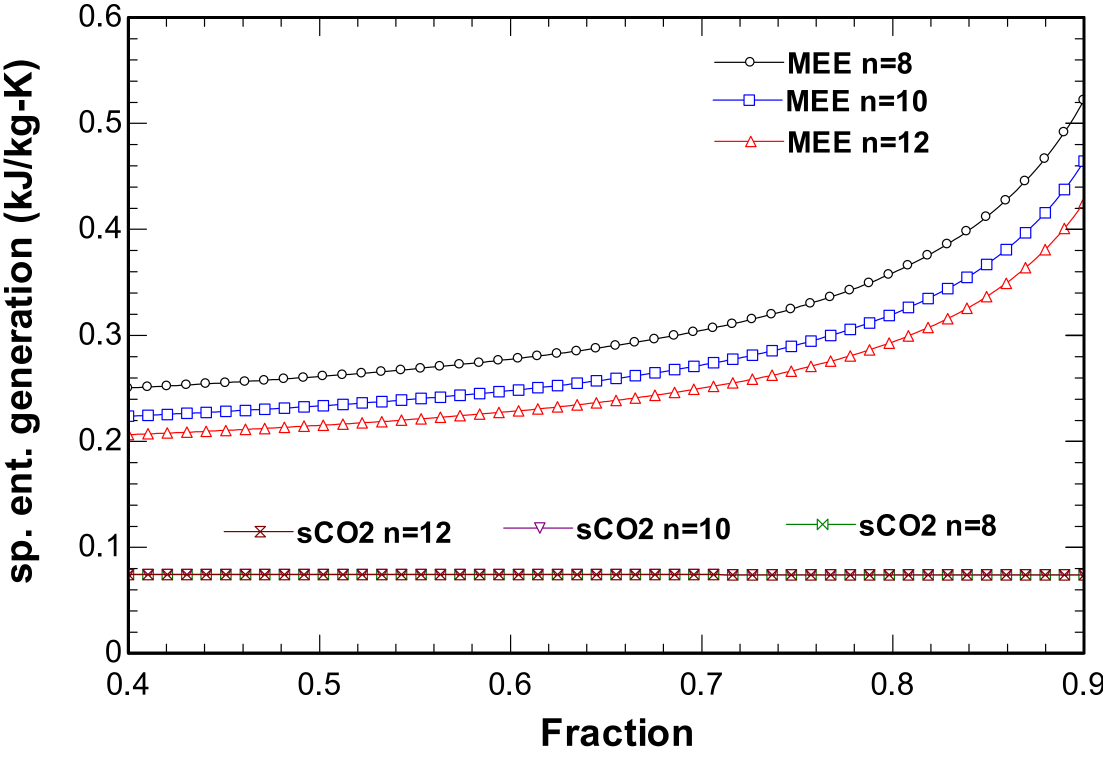

Figure 4.67 Specific entropy generation in MEE-TVC system and sCO_2 cycle versus fraction, recompressive

Figure 4.68 and Figure 4.69 represent the entropy generation percentage from total entropy generated in the sCO_2 power cycle for both, regeneration and recompression sCO_2 cycles. It can be seen from the bar plot of the regeneration cycle that the highest component contributing to the entropy generation is the regenerator with about 45 % entropy generation from the total. The compressor and turbine contribute in comparable values of 11 and 13 % respectively. The heat exchanger with the salt storage generates about 29.82 % from total. For the recompression cycle, the turbine of generates about 27.8 % from the total generated in the power cycle. However, the first and second compressors have comparable values of around 16 % each with a slightly higher contribution from the first compressor. Moreover, the high temperature recuperator has a significantly higher entropy generation rate than the low temperature recuperator reaching 26 % for the HTR and about 6 % for the LTR from total.

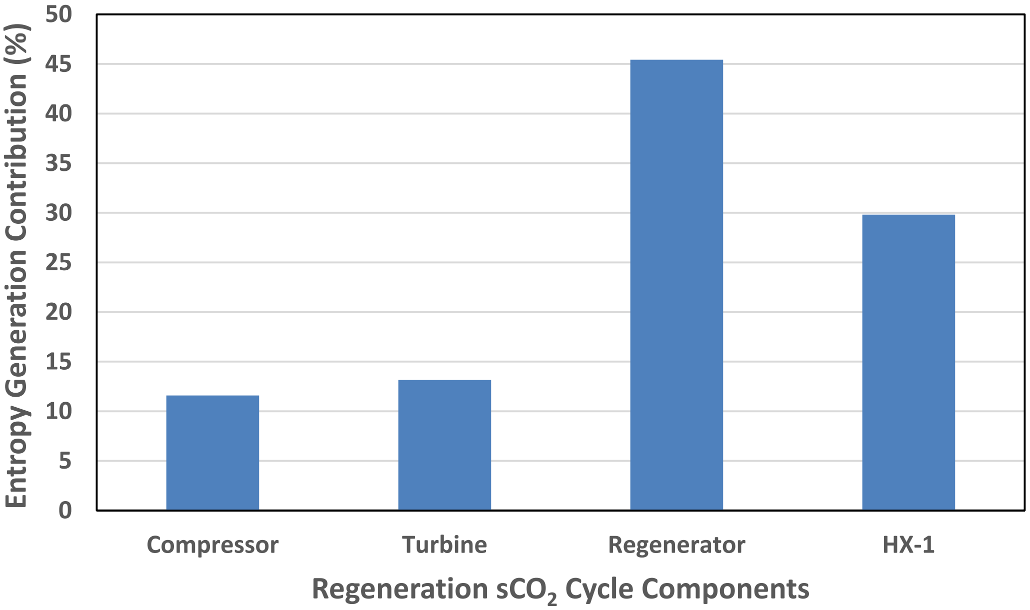

Figure 4.68 Percentage of entropy generation in components of regenerative sCO_2 cycle

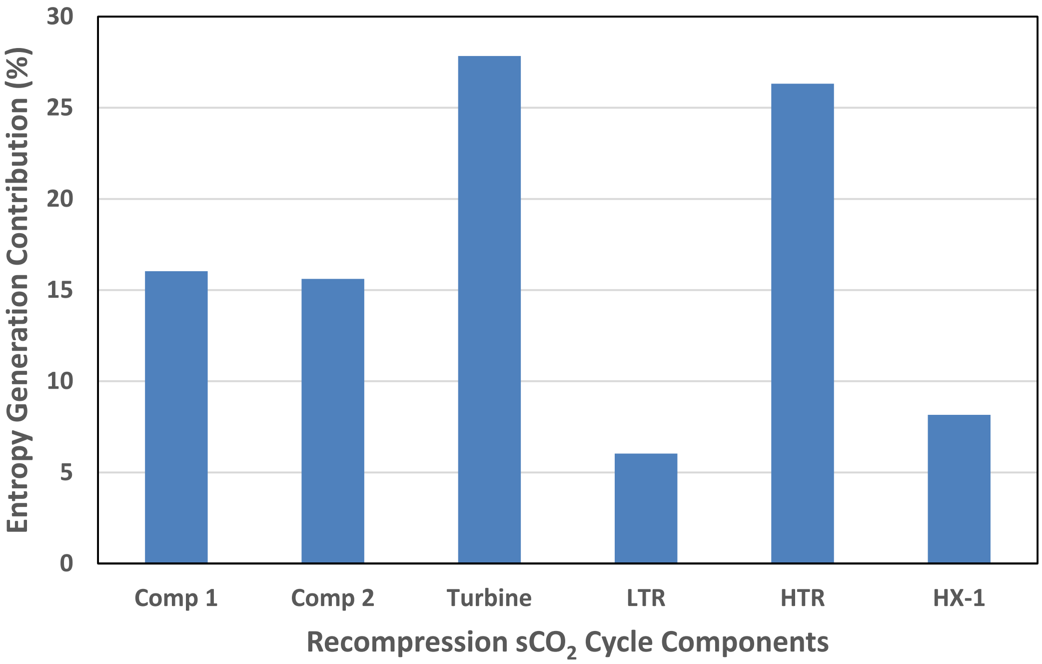

Figure 4.69 Percentage of entropy generation in components of recompressive sCO_2 cycle

Figure 4.70 and Figure 4.71 represent the entropy generation percentage of each component of the solar cogeneration system as a whole with respect to the whole system for the regeneration and recompression cogeneration cycles respectively. It is obviously deducted that the solar tower is the largest contributor to entropy generation in both configurations reaching almost 80 % from total entropy generation. The second contributor to the entropy production is the MEE-TVC desalination system although the entropy generation decreases for the desalination system with the increase in fraction on the expense of the increase in the fraction of entropy production of the sCO_2, whether regenerative or recompressive. It can be seen that the lowest contributor to entropy generation, almost relatively negligible, is the thermal storage contributing almost 0.3 % from total.

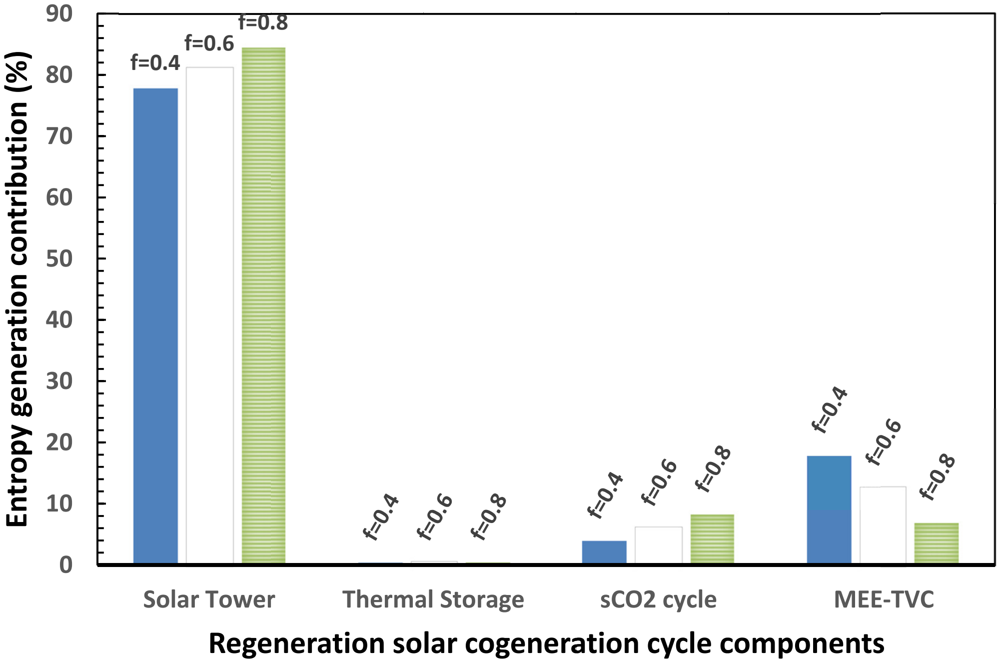

Figure 4.70 Percentage of entropy generation in components of the cogeneration system, regenerative

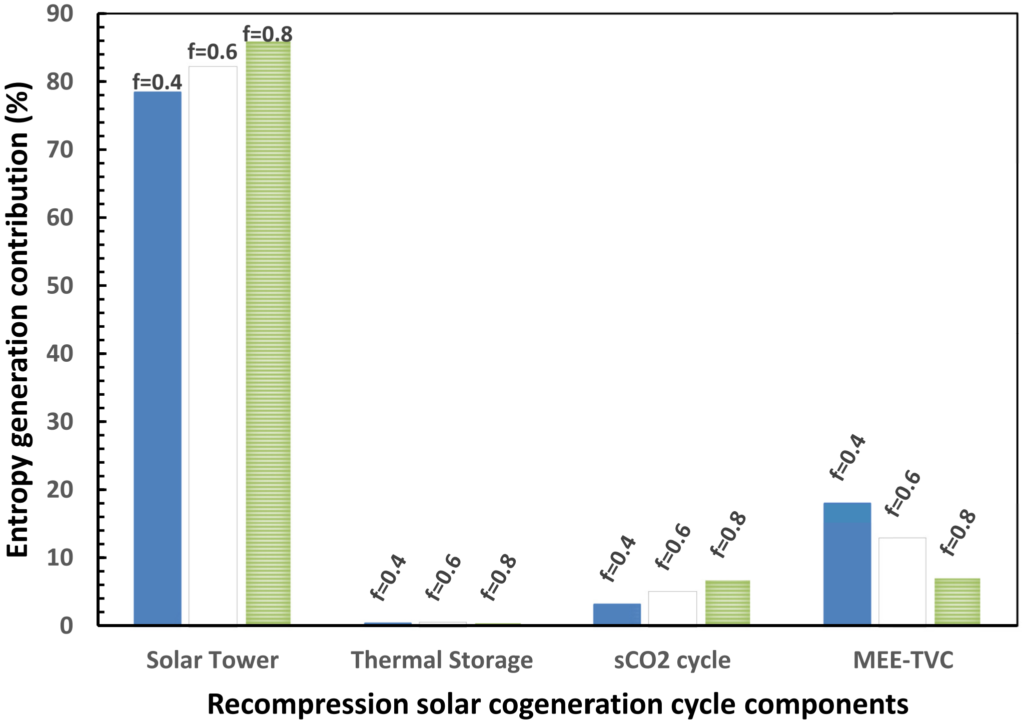

Figure 4.71 Percentage of entropy generation in components of the cogeneration system, recompressive

4.7 Components Exergy Analysis

In the following section, the results for exergy destruction, exergetic fuel depletion ratio, irreversibility ratio, and the improvement potential for each of the components of the regeneration cogeneration cycle and recompression cogeneration cycle is found in Table 4.11 and Table 4.12 respectively.

Table 4.11 Exergy Analysis for the components of the regeneration cogeneration cycle, f=0.5

	$Ex_{comp,j}$(kWh/d)	$IP_{comp,j}$(kWh/d)	$Y_{comp,j}$	$Y_{comp,j}^{*}$	$Z_{comp,j}$
Heliostat Field	890549	819633	0.4797	0.525000	0.4797
Central Reciever	454896	418672	0.2451	0.268200	0.1843
HST	4349	4002	0.0023	0.002564	0.0022
CST	2038	1875	0.0011	0.001201	0.0014
HX-1	8763	8065	0.0047	0.005166	0.0052
Turbine	10548	9708	0.0057	0.006218	0.0114
Compressor	9290	8550	0.0050	0.005477	0.0218
Regenerator	36429	33528	0.0196	0.021480	0.0330
HX-3	19623	18060	0.0106	0.011570	0.0509
HX-2	97878	90084	0.0527	0.057700	0.0967
OFWH	3371	3103	0.0018	0.001987	0.2901
Pump	39.92	36.74	0.0000	0.000024	0.0159
SJE	82968	76362	0.0447	0.048910	0.5063
DC	14735	13561	0.0079	0.008687	0.7158
Effects	27290	25114	0.0147	0.016087	0.0343
Preheaters	10380.9	9554.9	0.0056	0.006121	0.0686
Flashboxes	1675.063	1541.727	0.0009	0.000988	0.0214
Distillate	6255	5757	0.0034	0.003688	1.0000
Brine	10359	9534	0.0056	0.006107	1.0000
Rejected SW	4812	4429	0.0026	0.002837	1.0000
Total	**1696248.883**	**1561170.367**	**0.9138**	**1.0000**	

Table 4.12 Exergy Analysis for the components of the recompression cogeneration cycle, f=0.5

	$Ex_{comp,j}$ (kWh/d)	$IP_{comp,j}$ (kWh/d)	$Y_{comp,j}$	$Y_{comp,j}^{*}$	$Z_{comp,j}$
Heliostat Field	890549	814107	0.4797	0.530500	0.4797
Central Reciever	454896	415849	0.2451	0.271000	0.1843
HST	4349	3975	0.0023	0.002591	0.0022
CST	2038	1863	0.0011	0.001214	0.0014
HX-1	3925	3588	0.0021	0.002338	0.0020
Turbine	13390	12241	0.0072	0.007977	0.0114
HTR	12657	11571	0.0068	0.007540	0.0085
LTR	2909	2659	0.0016	0.001733	0.0033
Comp1	7714	7052	0.0042	0.004595	0.0218
Comp2	7512	6868	0.0040	0.004475	0.0329
HX-3	19343	17683	0.0104	0.011520	0.0599
HX-2	97833	89536	0.0527	0.058280	0.0966
OFWH	3416	3123	0.0018	0.002035	0.2898
Pump	39.92	36.49	0.0000	0.000024	0.0159
SJE	82968	75847	0.0447	0.049430	0.5063
DC	14943	13660	0.0080	0.008902	0.7404
Effects	27290	24945	0.0147	0.016258	0.0343
Preheaters	10380.9	9489.5	0.0056	0.006184	0.0686
Flashboxes	1675.063	1531.287	0.0009	0.000998	0.0214
Distillate	6255	5718	0.0034	0.003726	1.0000
Brine	10359	9470	0.0056	0.006171	1.0000
Rejected SW	4168	3811	0.0022	0.002483	1.0000
Total	**1678609.883**	**1534623.277**	**0.9043**	**1.0000**	

4.8 Cost Analysis

Table 4.13 and Table 4.14 represent the capital and operation & maintenance cost for the components of the cogeneration systems respectively. Figure 4.72 and Figure 4.73 represent the levelized cost of energy and levelized cost of water for the regeneration cogeneration cycle for fractions of 0.5 and 0.7. Figure 4.74 and Figure 4.75 represent the same results for the recompression cogeneration cycle. It can be seen, in general, that the regions with higher solar irradiation has the lowest levelized cost of energy and water. The levelized cost of energy increases with the increase in fraction, and the levelized cost of water increases with the increase in fraction. Moreover, the recompression cogeneration cycle results in lower levelized cost of energy compared to the regeneration cogeneration cycle.

Table 4.13 Capital cost for different components of the cogeneration cycle

	Cost	Unit
Recompressive Cycle[110]	30	$/kW
Regeneration Cycle[25]	16	$/kW
MEE-TVC Desalination[111]	1700	$/(m3/d)
Storage Cost[112]	0.49	$/kg
Capacity Factor[93]	70	%
Solar Field[113]	330	$/m2

Table 4.14 Operation & maintanace cost for different components of the cogeneration cycle

	O&M	Unit
Recompressive Cycle[114]	0.0022	$/kWh
Regeneration Cycle[25]	0.004324315	$/kWh
MEE-TVC Desalination[115]	51	$/(m3/d)
Storage Cost[112]	0.0098	$/kg

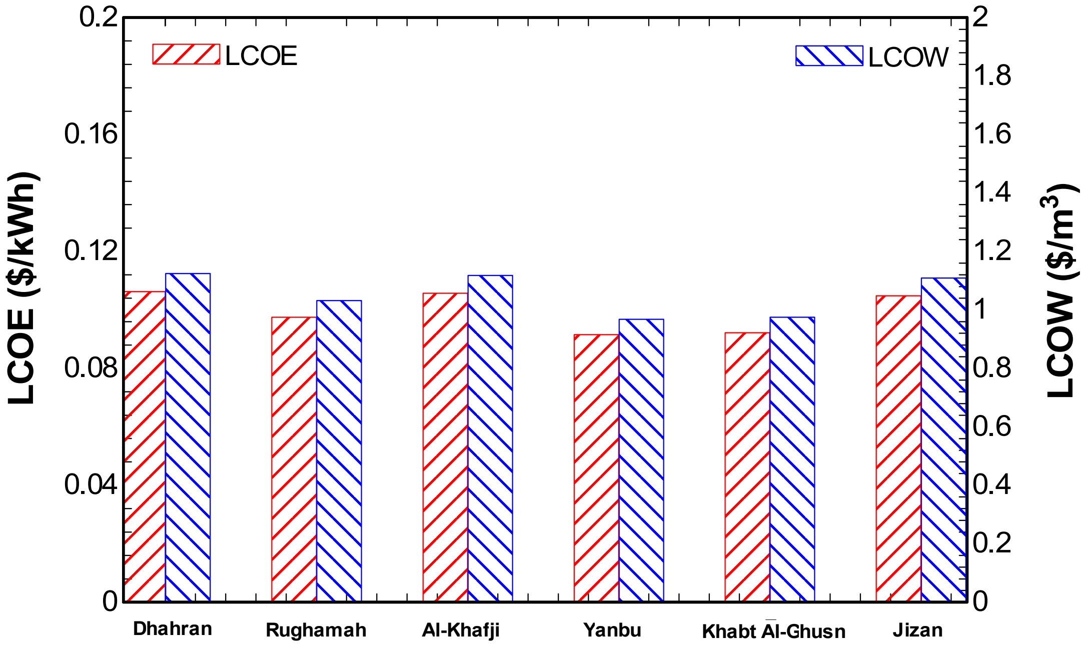

Figure 4.72 Levelized cost of energy and water for different regions, regenerative, f=0.5

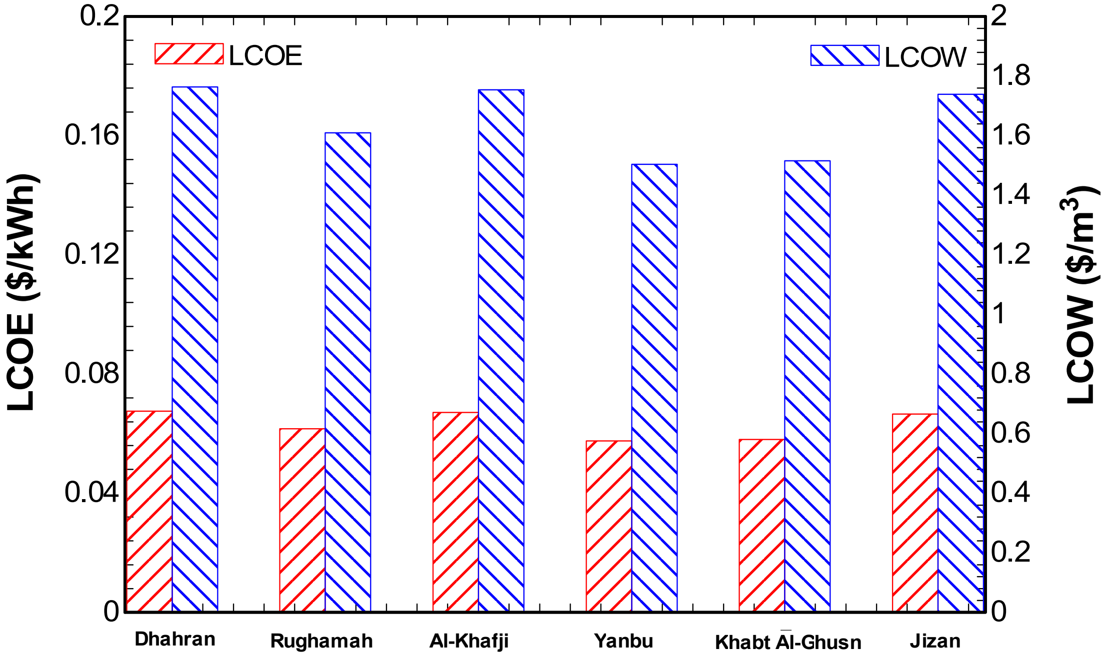

Figure 4.73 Levelized cost of energy and water for different regions, regenerative, f=0.7

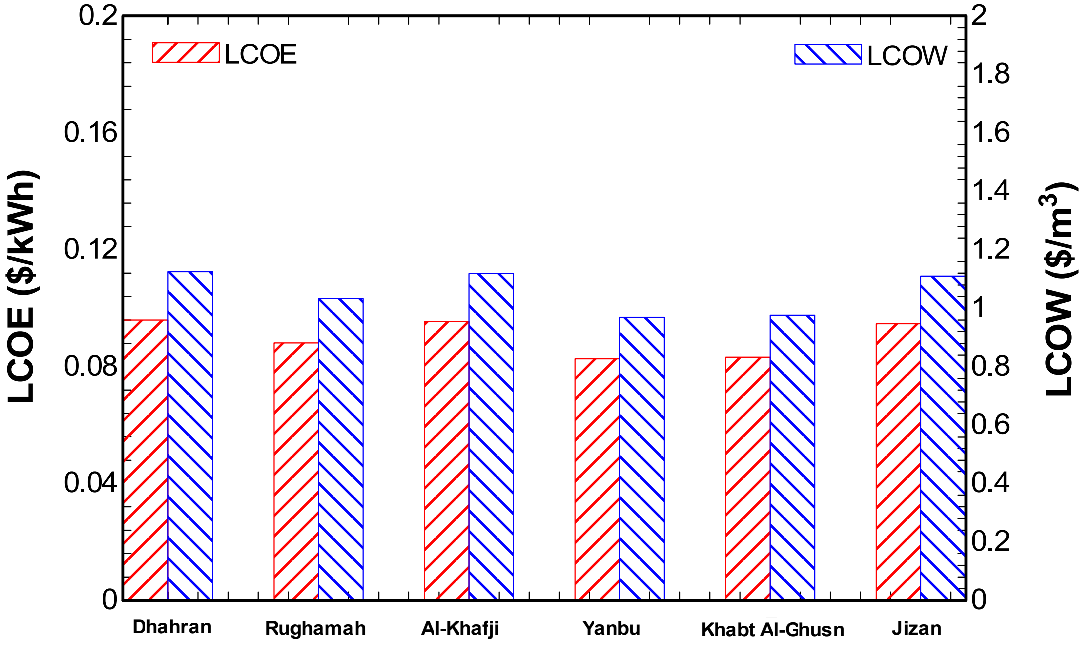

Figure 4.74 Levelized cost of energy and water for different regions, recompressive, f=0.5

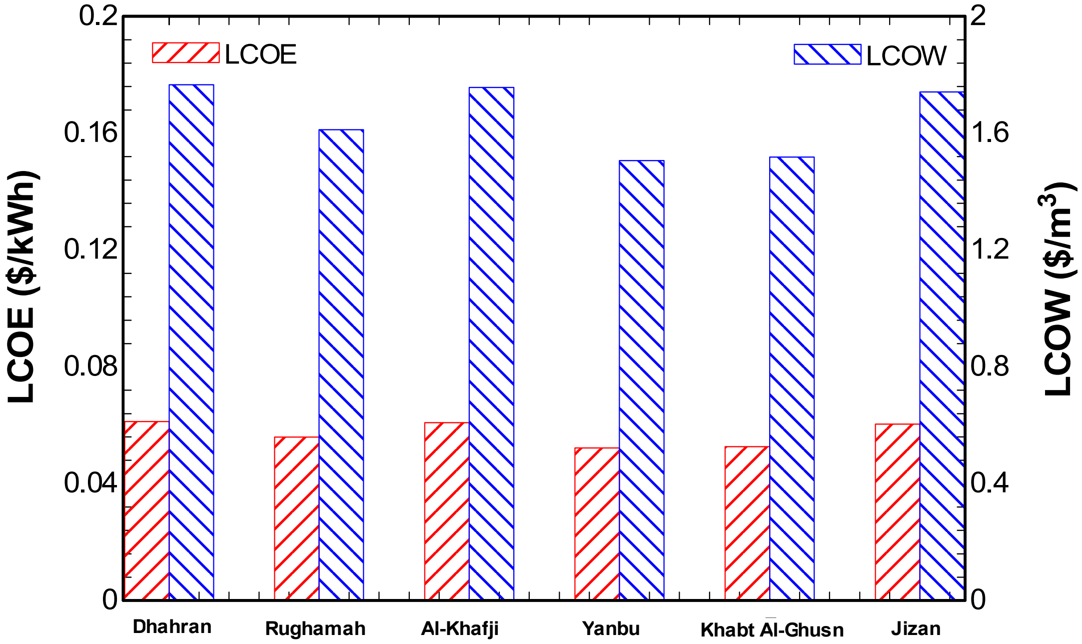

Figure 4.75 Levelized cost of energy and water for different regions, recompressive, f=0.7

After plotting the levelized cost of both energy and water, versus the fraction of heat accounted for the power cycle, it becomes clear to conclude that the cost per total lifetime generated energy is decreasing as the fraction is increasing. Also, it is clear to see the exponential increase in the cost per lifetime production of water. It is obvious to realize the following outcome since the heat added to the power cycle increases the power production and thus driving the levelized cost of energy to descend while in the same time the levelized cost of water is increasing. The increase in the levelized cost of water due to the increase in fraction can be interpreted by the decrease in water production on the expense of the increase of power output.

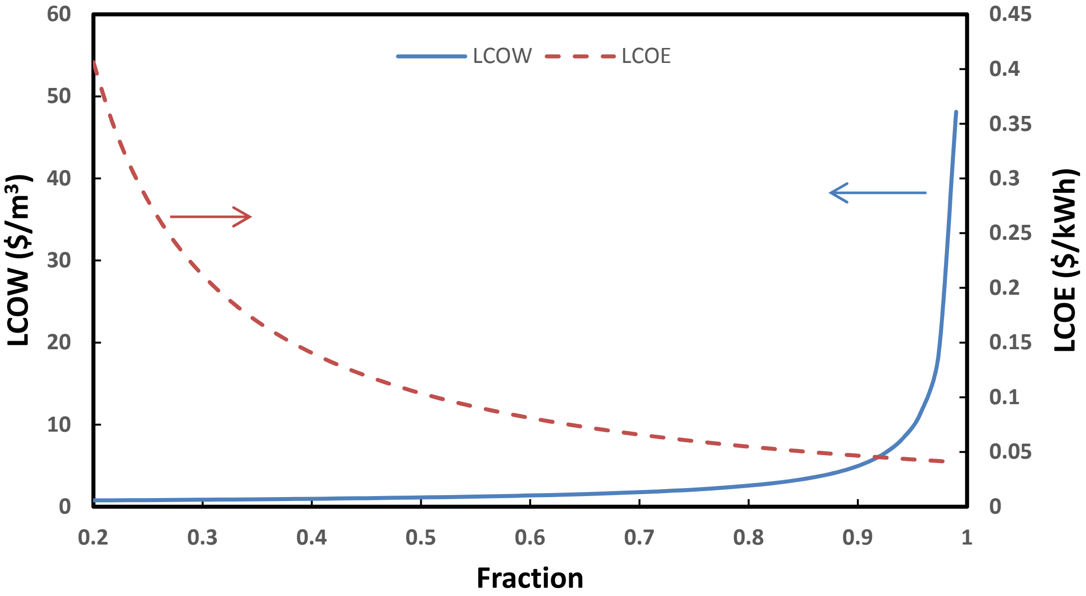

Figure 4.76 Levelized cost of energy and water as a function of fraction, regenerative

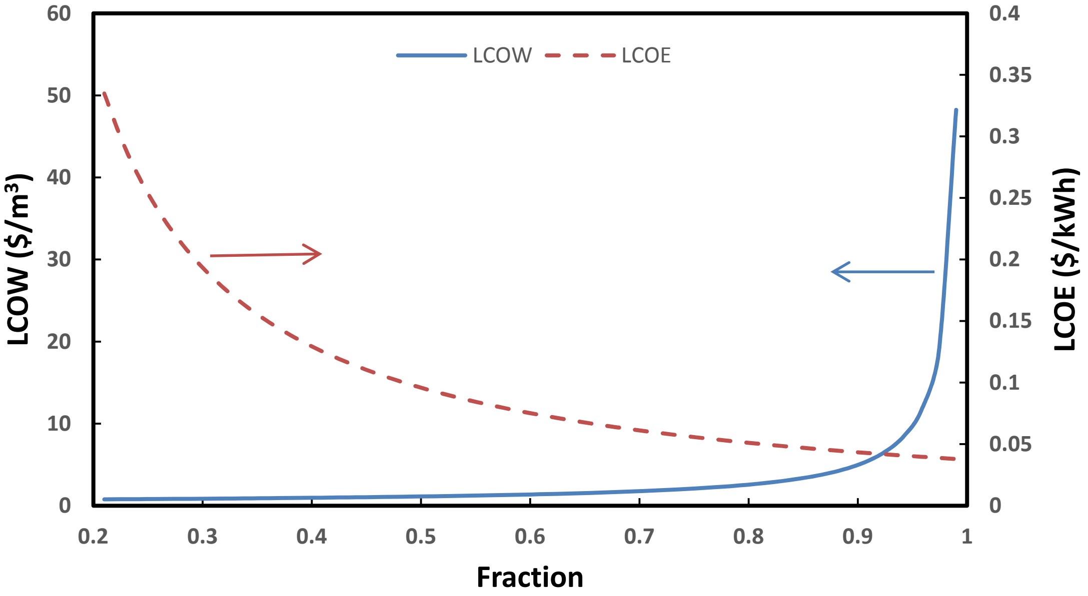

Figure 4.77 Levelized cost of energy and water as a function of fraction, recompressive

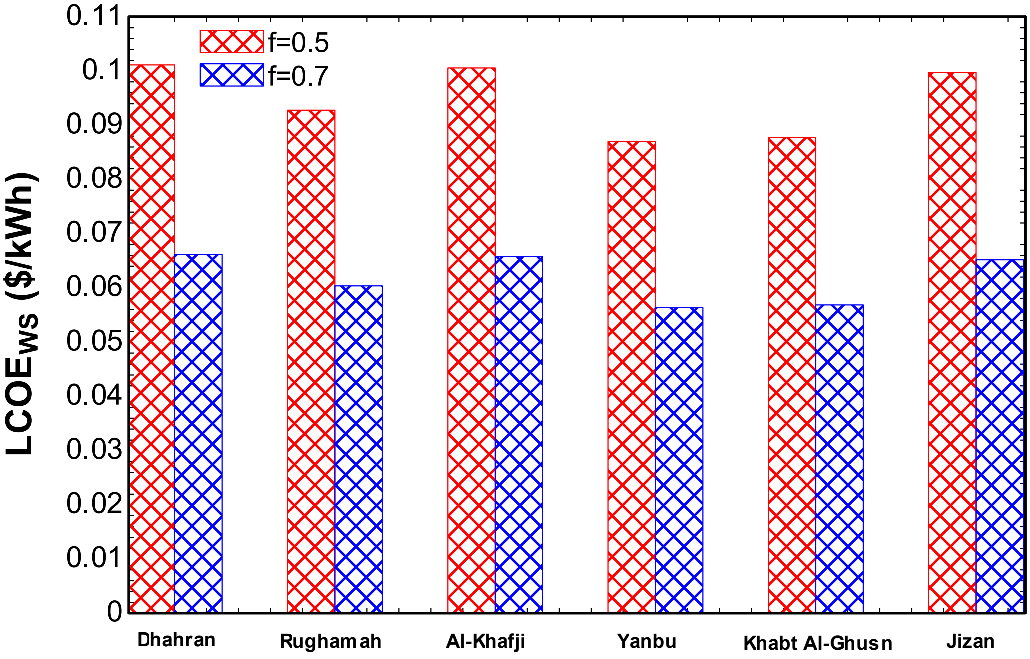

Figure 4.78 Net levelized cost of energy for different regions, regenerative

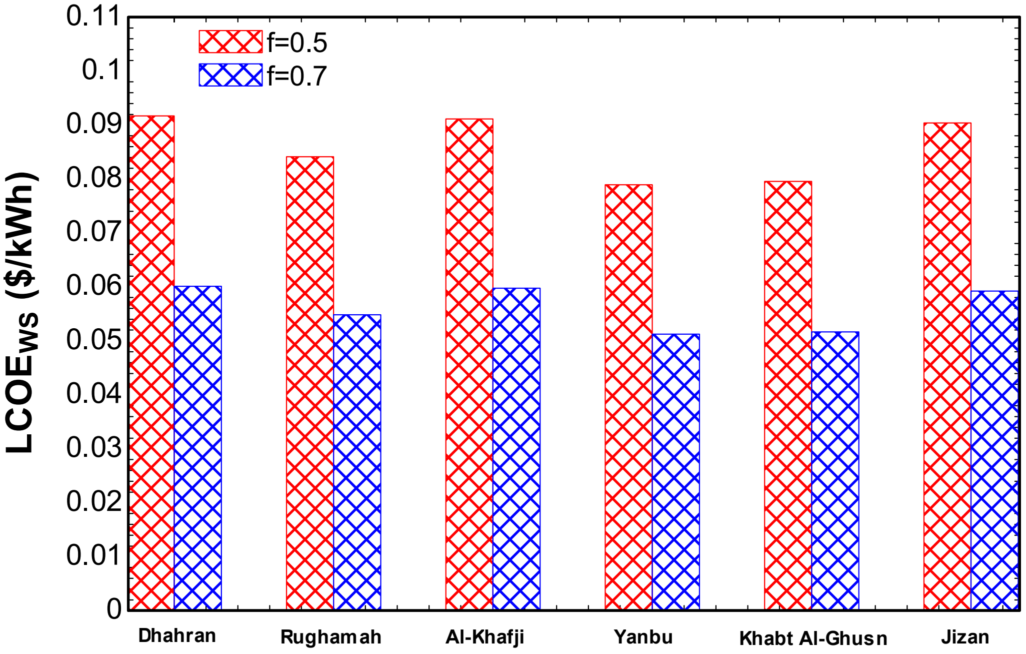

Figure 4.79 Net levelized cost of energy for different regions, recompressive

CHAPTER 5

Conclusion and Recommendations

In this chapter, a comprehensive review of the main findings in the previous chapters is introduced. Moreover, the future work and recommendations are also discussed.

5.1 Conclusions

The performance of two solar cogeneration configurations has been studied, both utilizing solar tower integrated with MEE-TVC desalination and sCO_2 Brayton cycle, first, regeneration, and the second, recompression. A two tank molten salt thermal storage is utilized to ensure a stable operation of the system throughout the day. The study is performed for six different regions of Saudi Arabia, namely, Dhahran, Yanbu-Al-Nakhil, Jizan, Khabt Al-Ghusn, Al-Khafji, and Jabal Al-Rughamah. The two tank molten salt storage utilizes a storage medium which is a mixture of 60%$NaNO_3$ and 40%KNO_3. The variation of the HST and CST molten salt mass within with respect to the time of the day for the average days of the months of June, March, and December is studied. Moreover, for the same days, the charging mass flow rate is studied with respect to the time of the day. However, for the solar cogeneration system as a whole, the average monthly power and water production for the different regions mentioned throughout the year is studied, and the average yearly production comparison for the regions under study is shown as well. For the energy analysis results, the main conclusions drawn are the following,

- The highest productivity is that of the region of Yanbu, followed by Khabt Al-Ghusn in the second place, and the rest are as follows, Jabal Al-Rughamah, Jizan, Al-Khafji, and Dhahran in descending order.
- The recompression solar cogeneration configuration generates more power than the regeneration solar cogeneration cycle due to the higher efficiency of the recompression sCO_2 cycle (6.25% increase in efficiency for the recompression cycle).
- The power to water ratio increases with respect to the increase in fraction, for both configurations.
- The increase in the turbine inlet temperature slightly increases the PWR and effective efficiency of the regeneration solar cogeneration configuration, whereas, a higher increase in PWR and effective efficiency is seen for the recompression cycle configuration.
- The PWR and effective efficiency increase with increase in the turbine inlet pressure for both configurations.
- The increase in the top brine salinity in MEE-TVC slightly increases the effective efficiency in both configurations.
- The effective efficiency is the highest at the minimum fraction of heat entering the sCO_2 cycle.

The entropy generation analysis for the two configurations is carried out as well. Among the results is the fraction of entropy generation from total of the components of MEE-TVC system for different number of effects, the total entropy generation in the MEE-TVC desalination system versus top brine salinity. The fraction of entropy generated in the components of the regeneration and recompression cycles from total is also studied. The specific entropy generation versus fraction for the MEE-TVC and the sCO_2 power cycle, regeneration and recompression, is also studied. The percentage of entropy generated in each of the components of the solar cogeneration system from total entropy generation in the whole system is presented as well. The main conclusions drawn from the entropy analysis are as follows,

- The highest contributing component in the whole system of the MEE-TVC is the steam jet ejector reaching 60 % for 6 effects and decreasing for larger number of effects, followed by the total generation in the effects, and the down condenser.
- The total entropy generation decreases slightly with the increase in the top brine salinity.
- The specific entropy generation in the MEE-TVC decreases with decreasing fraction, and the specific entropy generation of the sCO_2 cycle maintains a constant entropy generation. This result in confirming the energy results previously derived, that is, highest effective efficiency at the minimum specific entropy generation for the MEE-TVC and sCO_2 cycle.
- The solar tower is the largest contributor to entropy generation in both configurations reaching almost 80 % from total entropy generation, followed by the MEE-TVC desalination system, and the sCO_2 power cycle. The entropy generation in the two tank thermal storage is almost negligible.

The cost analysis of both configurations for different regions is carried out and the levelized cost of energy and levelized cost of water are obtained. Moreover, the change in the levelized cost of energy and water with respect to fraction is also calculated. The results drawn are summarized by,

- The regions characterized by the highest average solar irradiation throughout the year have the lowest LCOE and LCOW values. The region achieving the lowest cost is Yanbu, followed by Khabt Al-Ghusn in the second place, and the rest are as follows, Jabal Al-Rughamah, Jizan, Al-Khafji, and Dhahran.
- The recompression cogeneration cycle achieves lower LCOE compared to the regeneration cogeneration cycle.

5.2 Recommendations

The recommendations for future work are the following,

- Exergoeconomic analysis of the configurations under study.
- Energetic study of the hybrid operation of the solar cogeneration system with a fossil fuel energy source to ensure the compensation in the solar irradiation lack in the winter time so as to obtain a uniform production of power and water throughout the year.
- Study of the integration of the system with other CSP technologies (etc. Parabolic trough solar collector).
- Comparison between utilizing sCO_2 power cycle and steam cycle within.

References

[1] *International Energy Outlook*, 2013th ed. U.S. Energy Information Administration, 2014.

[2] S. a. Al-Ajlan, a. M. Al-Ibrahim, M. Abdulkhaleq, and F. Alghamdi, “Developing sustainable energy policies for electrical energy conservation in Saudi Arabia,” *Energy Policy*, vol. 34, no. 13, pp. 1556–1565, Sep. 2006.

[3] LENNTECH Water Treatment Solution, “Carbon dioxide.” [Online]. Available: http://www.lenntech.com/carbon-dioxide.htm. [Accessed: 01-Jan-2014].

[4] M. Kulhanek and V. Dostal, “Supercritical carbon dioxide cycles thermodynamic analysis and comparison,” *Supercrit. CO2 Power Cycle Symp. …*, 2011.

[5] “U.S. Environmental Protection Agency.” [Online]. Available: http://www.epa.gov/chp/basic/. [Accessed: 20-Sep-2014].

[6] H. El-Dessouky and H. Ettouney, *Fundamentals of Salt Water Desalination*. Elsevier Science: Elsevier Science & Technology Books, 2002.

[7] O. A. Hamed, “Evolutionary Developments Of Thermal Desalination Plants In The Arab Region,” 2004.

[8] A. Bejan, *Entropy generation minimization : the method of thermodynamic optimization of finite-size systems and finite-time processes*. 1996.

[9] O. Behar, A. Khellaf, and K. Mohammedi, “A review of studies on central receiver solar thermal power plants,” *Renew. Sustain. Energy Rev.*, vol. 23, pp. 12–39, Jul. 2013.

[10] M. a. Darwish and A. Alsairafi, “Technical comparison between TVC/MEB and MSF,” *Desalination*, vol. 170, no. 3, pp. 223–239, Nov. 2004.

[11] M. Atif and F. a. Al-Sulaiman, “Performance analysis of supercritical CO2 Brayton cycles integrated with solar central receiver system,” *2014 5th Int. Renew. Energy Congr.*, pp. 1–6, Mar. 2014.

[12] F. J. Collado, A. Gomez, and J. A. Turegano, “AN ANALYTIC FUNCTION FOR THE FLUX DENSITY,” *Sol. Energy*, vol. 37, no. 3, pp. 215–234, 1986.

[13] F. J. Collado and J. A. Turegano, “CALCULATION OF THE ANNUAL THERMAL ENERGY SUPPLIED BY A DEFINED HELIOSTAT FIELD,” *Sol. Energy*, vol. 42, no. 2, pp. 149–165, 1989.

[14] F. J. Collado, “Quick evaluation of the annual heliostat field efficiency,” *Sol. Energy*, vol. 82, no. 4, pp. 379–384, Apr. 2008.

[15] F. J. Collado, “Preliminary design of surrounding heliostat fields,” *Renew. Energy*, vol. 34, no. 5, pp. 1359–1363, May 2009.

[16] F. J. Collado and J. Guallar, “A review of optimized design layouts for solar power tower plants with campo code,” *Renew. Sustain. Energy Rev.*, vol. 20, pp. 142–154, Apr. 2013.

[17] F. J. Collado and J. Guallar, “Campo: Generation of regular heliostat fields,” *Renew. Energy*, vol. 46, pp. 49–59, Oct. 2012.

[18] S. Benammar, a. Khellaf, and K. Mohammedi, “Contribution to the modeling and simulation of solar power tower plants using energy analysis,” *Energy Convers. Manag.*, vol. 78, pp. 923–930, Feb. 2014.

[19] C. Xu, Z. Wang, X. Li, and F. Sun, “Energy and exergy analysis of solar power tower plants,” *Appl. Therm. Eng.*, vol. 31, no. 17–18, pp. 3904–3913, Dec. 2011.

[20] V. S. Reddy, S. C. Kaushik, and S. K. Tyagi, “Exergetic analysis and economic evaluation of central tower receiver solar thermal power plant,” *Int. J. Energy Res.*, no. November 2013, pp. 1288–1303, 2014.

[21] G. Franchini, a. Perdichizzi, S. Ravelli, and G. Barigozzi, “A comparative study between parabolic trough and solar tower technologies in Solar Rankine Cycle and Integrated Solar Combined Cycle plants,” *Sol. Energy*, vol. 98, pp. 302–314, Dec. 2013.

[22] M. T. Dunham and B. D. Iverson, “High-efficiency thermodynamic power cycles for concentrated solar power systems,” *Renew. Sustain. Energy Rev.*, vol. 30, pp. 758–770, Feb. 2014.

[23] J. Liu, H. Chen, Y. Xu, L. Wang, and C. Tan, “A solar energy storage and power generation system based on supercritical carbon dioxide,” *Renew. Energy*, vol. 64, pp. 43–51, Apr. 2014.

[24] T. Neises and C. Turchi, “A Comparison of Supercritical Carbon Dioxide Power Cycle Configurations with an Emphasis on CSP Applications,” *Energy Procedia*, vol. 49, pp. 1187–1196, 2014.

[25] R. Chacartegui, J. M. Muñoz de Escalona, D. Sánchez, B. Monje, and T. Sánchez, "Alternative cycles based on carbon dioxide for central receiver solar power plants," *Appl. Therm. Eng.*, vol. 31, no. 5, pp. 872–879, Apr. 2011.

[26] M. Trela, R. Kwidziński, and D. Butrymowicz, "A study of transcritical carbon dioxide cycles with heat regeneration," *Arch. Thermodyn.*, vol. 34, no. 3, pp. 197–217, Jan. 2013.

[27] V. Dostal, "A supercritical carbon dioxide cycle for next generation nuclear reactors - ProQuest," 2004.

[28] X. R. Zhang, H. Yamaguchi, K. Fujima, M. Enomoto, and N. Sawada, "Theoretical analysis of a thermodynamic cycle for power and heat production using supercritical carbon dioxide," *Energy*, vol. 32, no. 4, pp. 591–599, Apr. 2007.

[29] G. Fosselgard and K. Wangnick, "Comprehensive Study on Capital and Operational Expenditures for Different Types of Seawater Desalting Plants (RO, MVC, ME, ME-TVC, MSF) Rated between 200 m3/d and 3,000 m3/d.," *Desalination*, vol. 76, pp. 215–240, 1989.

[30] I. S. Al-Mutaz and I. Wazeer, "Development of a steady-state mathematical model for MEE-TVC desalination plants," *Desalination*, vol. 351, pp. 9–18, Oct. 2014.

[31] A. O. Bin Amer, "Development and optimization of ME-TVC desalination system," *Desalination*, vol. 249, no. 3, pp. 1315–1331, Dec. 2009.

[32] I. Janghorban Esfahani, A. Ataei, V. Shetty K, T. Oh, J. H. Park, and C. Yoo, "Modeling and genetic algorithm-based multi-objective optimization of the MED-TVC desalination system," *Desalination*, vol. 292, pp. 87–104, Apr. 2012.

[33] R. K. Kamali, a. Abbassi, S. a. Sadough Vanini, and M. Saffar Avval, "Thermodynamic design and parametric study of MED-TVC," *Desalination*, vol. 222, no. 1–3, pp. 596–604, Mar. 2008.

[34] O. Samaké, N. Galanis, and M. Sorin, "Thermodynamic study of multi-effect thermal vapour-compression desalination systems," *Energy*, vol. 72, pp. 69–79, Aug. 2014.

[35] M. Shakouri, H. Ghadamian, and R. Sheikholeslami, "Optimal model for multi effect desalination system integrated with gas turbine," *Desalination*, vol. 260, no. 1–3, pp. 254–263, Sep. 2010.

[36] F. N. Alasfour, M. a. Darwish, and a. O. Bin Amer, "Thermal analysis of ME-TVC+MEE desalination systems," *Desalination*, vol. 174, no. 1, pp. 39–61, Apr. 2005.

[37] H. T. E. L. Dessouky, H. M. Ettouney, and F. A. Juwayhel, “Multiple effect evaporation-vapour compression desalination processes,” *Chem. Eng. Res. Des.*, vol. 78, no. May, 2000.

[38] R. Kouhikamali and M. S. M. Mehdizadeh, “Process investigation of different locations of thermo-compressor suction in MED–TVC plants,” *Desalination*, vol. 280, no. 1–3, pp. 134–138, Oct. 2011.

[39] H.-S. Choi, T.-J. Lee, Y.-G. Kim, and S.-L. Song, “Performance improvement of multiple-effect distiller with thermal vapor compression system by exergy analysis,” *Desalination*, vol. 182, no. 1–3, pp. 239–249, Nov. 2005.

[40] A. A. Mabrouk, A. S. Nafey, and H. E. S. Fath, “Thermoeconomic analysis of some existing desalination processes,” vol. 205, no. May 2006, pp. 354–373, 2007.

[41] F. N. Alasfour and H. F. Alajmi, “INTEGRATION OF TVC DESALINATION SYSTEM WITH COGENERATION PLANT : PARAMETRIC STUDY,” in *Fourteenth International Water Technology Conference*, 2010, pp. 117–132.

[42] C. K. Ho, S. S. Khalsa, and G. J. Kolb, “Methods for probabilistic modeling of concentrating solar power plants,” *Sol. Energy*, vol. 85, no. 4, pp. 669–675, Apr. 2011.

[43] J. Rheinlander and F. Lippke, “Electricity and Potable Water from a Solar Tower Power Plant,” *Renew. Energy*, vol. 14, pp. 23–28, 1998.

[44] H. W. Prengle, J. C. Hunt, C. E. Mauk, and E. C. Sun, “SOLAR ENERGY WITH CHEMICAL STORAGE FOR COGENERATION OF ELECTRIC POWER AND HEAT,” *Sol. Energy*, vol. 24, pp. 373–384, 2000.

[45] W. Hoefler, A. Kamal, D. Jarrar, S. Solar, C. Program, H. Hoppman, H. Zewen, S. Division, M. B. Gmbh, and W. Germany, “Design Specifications and Application of a 100 kWe(700 kWth) Cogeneration Solar Power Plant,” *Sol. Energy*, vol. 32, no. 2, pp. 263–269, 1984.

[46] F. McDonald, “A hybrid solar closed-cycle gas turbine combined heat and power plant concept to meet the continuous total energy needs of a small community,” *Heat Recover. Syst.*, vol. 6, no. 5, pp. 399–419, 1986.

[47] H. Alrobaei, “Novel integrated gas turbine solar cogeneration power plant,” *Desalination*, vol. 220, no. 1–3, pp. 574–587, Mar. 2008.

[48] R. Soltani, P. Mohammadzadeh Keleshtery, M. Vahdati, M. H. KhoshgoftarManesh, M. a. Rosen, and M. Amidpour, “Multi-objective optimization of a solar-hybrid cogeneration cycle: Application to CGAM problem,” *Energy Convers. Manag.*, vol. 81, pp. 60–71, May 2014.

[49] S. Giuliano, R. Buck, and S. Eguiguren, “ANALYSIS OF SOLAR THERMAL POWER PLANTS WITH THERMAL ENERGY STORAGE AND SOLAR-HYBRID OPERATION STRATEGY,” *Sol. Energy Eng.*, vol. 133, 2011.

[50] K. M. Hardiman, B. Seyedan, R. Hynes, and G. Delfs, “Solar / Combined Cycle Gas Turbine (CCGT) Hybrid Power Generation,” in *Proceedings of Renewable Energy World Asia*, 2009.

[51] L. García-Rodríguez and J. Blanco-Gálvez, “Solar-heated Rankine cycles for water and electricity production: POWERSOL project,” *Desalination*, vol. 212, no. 1–3, pp. 311–318, Jun. 2007.

[52] J. Blanco Gálvez, L. García-Rodríguez, and I. Martín-Mateos, “Seawater desalination by an innovative solar-powered membrane distillation system: the MEDESOL project,” *Desalination*, vol. 246, no. 1–3, pp. 567–576, Sep. 2009.

[53] A. Ghobeity, C. J. Noone, C. N. Papanicolas, and A. Mitsos, “Optimal time-invariant operation of a power and water cogeneration solar-thermal plant,” *Sol. Energy*, vol. 85, no. 9, pp. 2295–2320, Sep. 2011.

[54] J. I. Ortega, J. I. Burgaleta, and F. M. Téllez, “Central Receiver System Solar Power Plant Using Molten Salt as Heat Transfer Fluid,” *J. Sol. Energy Eng.*, vol. 130, no. 2, p. 024501, 2008.

[55] M. Romero, R. Buck, and J. E. Pacheco, “An Update on Solar Central Receiver Systems, Projects, and Technologies,” *J. Sol. Energy Eng.*, vol. 124, no. 2, p. 98, 2002.

[56] G. J. K. Daniel J. Alpert, “Performance of the Solar One power plant as simulated by the SOLERGY computer code,” 1988.

[57] A. Yogev, A. Kribus, and M. Epstein, “SOLAR ‘ TOWER REFLECTOR ’ SYSTEMS : A NEW APPROACH SOLAR PLANTS,” *Int. J. Hydrogen Energy*, vol. 23, no. 4, pp. 239–245, 1998.

[58] J. Blackmon, N. Jones, and R. Drubka, “Thermally Controlled Solar Reflector Facet with Heat Recovery,” 2004.

[59] A. Segal and M. Epstein, “Practical Considerations in Designing Large Scale ‘Beam Down’ Optical Systems,” *J. Sol. Energy Eng.*, vol. 130, no. 1, p. 011009, 2008.

[60] A. H. Slocum, D. S. Codd, J. Buongiorno, C. Forsberg, T. McKrell, J.-C. Nave, C. N. Papanicolas, A. Ghobeity, C. J. Noone, S. Passerini, F. Rojas, and A. Mitsos, “Concentrated solar power on demand,” *Sol. Energy*, vol. 85, no. 7, pp. 1519–1529, Jul. 2011.

[61] R. K. Akikur, R. Saidur, H. W. Ping, and K. R. Ullah, “Performance analysis of a co-generation system using solar energy and SOFC technology,” *Energy Convers. Manag.*, vol. 79, pp. 415–430, Mar. 2014.

[62] R. K. Akikur, K. R. Ullah, H. W. Ping, and R. Saidur, “Application of Solar Energy and Reversible Solid Oxide Fuel Cell in a Co-Generation System,” *Int. J. Innov. Manag. Technol.*, vol. 5, 2014.

[63] C. Li, G. Kosmadakis, D. Manolakos, E. Stefanakos, G. Papadakis, and D. Y. Goswami, “Performance investigation of concentrating solar collectors coupled with a transcritical organic Rankine cycle for power and seawater desalination co-generation,” *Desalination*, vol. 318, pp. 107–117, Jun. 2013.

[64] A. M. El-Nashar, “Cogeneration for power and desalination - State of the art review,” *Desalination*, vol. 134, no. 1–3, pp. 7–28, 2001.

[65] A. M. El-Nashar, “Optimal design of a cogeneration plant for power and desalination taking equipment reliability into consideration,” *Desalination*, vol. 229, no. 1–3, pp. 21–32, 2008.

[66] M. Hajeeh, O. Mohammad, W. Behbahani, and B. Dashti, “A mathematical model for a dual-purpose power and desalination plant,” *Desalination*, vol. 159, no. 1, pp. 61–68, 2003.

[67] E. W. Perz and S. Bergmann, “A simulation environment for the techno-economic performance prediction of water and power cogeneration systems using renewable and fossil energy sources,” *Desalination*, vol. 203, no. 1–3, pp. 337–345, 2007.

[68] L. Wu, Y. Hu, and C. Gao, “Optimum design of cogeneration for power and desalination to satisfy the demand of water and power,” *Desalination*, vol. 324, pp. 111–117, Sep. 2013.

[69] G. Iaquaniello, a. Salladini, a. Mari, a. a. Mabrouk, and H. E. S. Fath, “Concentrating solar power (CSP) system integrated with MED-RO hybrid desalination,” *Desalination*, vol. 336, no. 1, pp. 121–128, 2014.

[70] T. Altmann, “A new power and water cogeneration concept with the application of reverse osmosis desalination,” *Desalination*, vol. 114, no. 2, pp. 139–144, 1997.

[71] A. M. El-Nashar, “Cost allocation in a cogeneration plant for the production of power and desalted water - comparison of the exergy cost accounting method with the WEA method,” *Desalination*, vol. 122, no. 1, pp. 15–34, 1999.

[72] M. J. Safi and a. Korchani, “Cogeneration applied to water desalination: Simulation of different technologies,” *Desalination*, vol. 125, no. 1–3, pp. 223–229, 1999.

[73] S. E. Shakib, S. R. Hosseini, M. Amidpour, and C. Aghanajafi, “Multi-objective optimization of a cogeneration plant for supplying given amount of power and fresh water,” *Desalination*, vol. 286, pp. 225–234, 2012.

[74] J. A. Duffie and W. A. Beckman, *Solar Engineering of Thermal Processes*. John Wiley & Sons Inc, 2013.

[75] M. Schmitz, P. Schwarzbözl, R. Buck, and R. Pitz-Paal, “Assessment of the potential improvement due to multiple apertures in central receiver systems with secondary concentrators,” *Sol. Energy*, vol. 80, no. 1, pp. 111–120, Jan. 2006.

[76] G. Sassi, “Some notes on shadow and blockage effects,” *Sol. Energy*, vol. 31, no. 3, pp. 331–333, Jan. 1983.

[77] R. P.-P. Peter Schwarzbözl, “Visual HFLCAL - A Software Tool for Layout and Optimisation of Heliostat Fields,” in *SolarPACES*, 2009, no. 2009–09–16.

[78] F. J. Collado, “One-point fitting of the flux density produced by a heliostat,” *Sol. Energy*, vol. 84, no. 4, pp. 673–684, Apr. 2010.

[79] M. A. Abido and N. A. Al-Ali, “Multi-objective differential evolution for optimal power flow,” in *2009 International Conference on Power Engineering, Energy and Electrical Drives*, 2009, pp. 101–106.

[80] C. J. Noone, M. Torrilhon, and A. Mitsos, “Heliostat field optimization: A new computationally efficient model and biomimetic layout,” *Sol. Energy*, vol. 86, no. 2, pp. 792–803, Feb. 2012.

[81] E. J. Sheu and A. Mitsos, “Optimization of a hybrid solar-fossil fuel plant: Solar steam reforming of methane in a combined cycle,” *Energy*, vol. 51, pp. 193–202, Mar. 2013.

[82] S. Klein and F. Alvarado, “Engineering equation solver,” *F-Chart Software, Box*, 2002.

[83] A. Moisseytsev and J. Sienicki, “Performance Improvement Options for the Supercritical Carbon Dioxide Brayton Cycle,” 2008.

[84] N. M. Al-Najem, M. A. Darwish, and F. A. Youssef, “Thermovapor compression desalters: energy and availability — Analysis of single- and multi-effect systems,” *Desalination*, vol. 110, no. 3, pp. 223–238, Sep. 1997.

[85] F. Al-Juwayhel, H. El-Dessouky, and H. Ettouney, “Analysis of single-effect evaporator desalination systems combined with vapor compression heat pumps,” *Desalination*, vol. 114, no. 3, pp. 253–275, Dec. 1997.

[86] R. B. Power, *Steam Jet Ejectors for the Process Industries*. McGraw-Hill, 1994.

[87] M. A. Darwish, “Cogeneration Power—Desalination Plants,” *Desalination*, vol. 69, no. 1, pp. 27–46, Jan. 1988.

[88] M. Kanoglu and I. Dincer, “Performance assessment of cogeneration plants,” *Energy Convers. Manag.*, vol. 50, no. 1, pp. 76–81, Jan. 2009.

[89] K. H. Mistry, R. K. McGovern, G. P. Thiel, E. K. Summers, S. M. Zubair, and J. H. Lienhard V, “Entropy Generation Analysis of Desalination Technologies,” *Entropy*, vol. 13, no. 12, pp. 1829–1864, Sep. 2011.

[90] K. Mistry and J. Lienhard, “Generalized Least Energy of Separation for Desalination and Other Chemical Separation Processes,” *Entropy*, vol. 15, no. 6, pp. 2046–2080, May 2013.

[91] K. H. Mistry, “Irreversibilities and Nonidealities in Desalination Systems by,” Massachusetts Institute of Technology, 2013.

[92] U.S. Energy Information Administration, “Levelized Cost and Levelized Avoided Cost of New Generation Resources in the Annual Energy Outlook 2014,” no. April, pp. 1–12, 2014.

[93] U.S. Department of Energy, “5 . Concentrating Solar Power : Technologies , Cost , and Performance,” 2012.

[94] K. Bognar, P. Blechinger, and F. Behrendt, “Seawater desalination in micro grids: an integrated planning approach,” *Energy. Sustain. Soc.*, vol. 2, no. 1, p. 14, 2012.

[95] C. K. Ho and B. D. Iverson, “Review of high-temperature central receiver designs for concentrating solar power,” *Renew. Sustain. Energy Rev.*, vol. 29, pp. 835–846, Jan. 2014.

[96] “NASA Surface meteorology and Solar Energy.” [Online]. Available: https://eosweb.larc.nasa.gov/cgi-bin/sse/grid.cgi?&email=skip@larc.nasa.gov&step=1&p=&lat=16.90&submit=Reset&lon=42.58. [Accessed: 26-Jan-2015].

[97] M. Liu, M. Belusko, N. H. Steven Tay, and F. Bruno, “Impact of the heat transfer fluid in a flat plate phase change thermal storage unit for concentrated solar tower plants,” *Sol. Energy*, vol. 101, pp. 220–231, 2014.

[98] F. Zaversky, J. García-Barberena, M. Sánchez, and D. Astrain, “Transient molten salt two-tank thermal storage modeling for CSP performance simulations,” *Sol. Energy*, vol. 93, pp. 294–311, 2013.

[99] M. Al-sahali and H. Ettouney, “Developments in thermal desalination processes : Design , energy , and costing aspects,” vol. 214, pp. 227–240, 2007.

[100] F. Al Asfour, “Energy consumption in equivalent work by different desalting methods : case study for Kuwait,” vol. 152, pp. 83–92, 2002.

[101] A. Almulla, A. Hamad, and M. Gadalla, “Integrating hybrid systems with existing thermal desalination plants,” vol. 174, pp. 171–192, 2005.

[102] R. Deng, L. Xie, H. Lin, J. Liu, and W. Han, “Integration of thermal energy and seawater desalination,” *Energy*, vol. 35, no. 11, pp. 4368–4374, 2010.

[103] M. A. Darwish, F. Al-juwayhel, and H. K. Abdulraheim, “Multi-effect boiling systems from an energy viewpoint,” vol. 194, pp. 22–39, 2006.

[104] E. Cardona, A. Piacentino, and F. Marchese, “Performance evaluation of CHP hybrid seawater desalination plants,” vol. 205, no. May 2006, pp. 1–14, 2007.

[105] A. Messineo and F. Marchese, “Performance evaluation of hybrid RO / MEE systems powered by a WTE plant,” vol. 229, no. 22, pp. 82–93, 2008.

[106] T. Rensonnet, J. Uche, and L. S. Ã, “Simulation and thermoeconomic analysis of different configurations of gas turbine (GT) -based dual-purpose power and desalination plants (DPPDP) and hybrid plants (HP),” vol. 32, pp. 1012–1023, 2007.

[107] J. Andrianne and F. Alardin, “Thermal and membrane processe economics : optimized selection for seawater desalination,” vol. 153, 2002.

[108] K. Ansari, H. Sayyaadi, and M. Amidpour, “Thermoeconomic optimization of a hybrid pressurized water reactor (PWR) power plant coupled to a multi effect distillation desalination system with thermo-vapor compressor (MED-TVC) Reheat cooler Steam generator,” *Energy*, vol. 35, no. 5, pp. 1981–1996, 2010.

[109] G. M. Zak, “Thermal Desalination : Structural Optimization and Integration in Clean Power and Water,” Massachusetts Institute of Technology, 2012.

[110] A. Moisseytsev and J. Sienicki, “Performance improvement options for the supercritical carbon dioxide brayton cycle,” *Argonne Natl. Lab. ANL-GenIV-103*, 2008.

[111] M. Moser, F. Trieb, and T. Fichter, “Potential of Concentrating Solar Power Plants for the Combined Production of Water and Electricity in MENA Countries,” *J. Sustain. Dev. Energy, WAter Environ. Syst.*, vol. 1, no. 2, pp. 122–141, 2013.

[112] D. Kearney and B. Kelly, "Assessment of a Molten Salt Heat Transfer Fluid in a Parabolic Trough Solar Field," *Jsee*, no. April, pp. 1–20, 2002.

[113] M. P. Petrov, M. S. Popa, and T. H. Franson, "SOLAR AUGMENTATION OF CONVENTIONAL STEAM PLANTS : FROM SYSTEM STUDIES TO REALITY," 2012, no. May, pp. 1–8.

[114] U.S. Department of Energy, "Review of Combined Heat and Technologies Power Technologies," 1999.

[115] J. Ghelichzadeh, R. Derakhshan, and A. Asadi, "Application of Alternative Configuration of Cogeneration Plant in order to Meet Power and Water Demand," *Chem. Eng. Trans.*, vol. 29, no. 2006, pp. 775–780, 2012.

Vitae

Name : Amine Abdullah Kouta

Nationality : Lebanese

Date of Birth : 4/22/1990

Email : amin.kouta@hotmail.com

Address : Al-Falak Compound/Al-Andalus Street/Al-Khobar-KSA

Academic Background

M.Sc. Mechanical Engineering

May, 2015

King Fahd University of Petroleum and Minerals,

Dhahran, Saudi Arabia

B.Sc. Mechanical Engineering

June, 2011

University of Balamand,

Koura, Lebanon

Publications

"Performance Assessment of Solar Tower Integrated with Regenerative Supercritical CO_2 Brayton Cycle and MEE-TVC Desalination System", SolarPACES 2015 Conference Paper. Accepted.